Reconstruction of deglaciation history since the Last Glacial Maximum along the southern Soya Coast, Lützow-Holm Bay, East Antarctica

川又　基人

博士（理学）

総合研究大学院大学
複合科学研究科
極域科学専攻

令和２（2020）年度

Reconstruction of deglaciation history since the Last Glacial Maximum along the southern Soya Coast, Lützow-Holm Bay, East Antarctica

Moto Kawamata

Department of Polar Science

School of Multidisciplinary Sciences

The Graduate University for Advanced Studies, SOKENDAI

March 2021

Abstract

Geological reconstruction of the retreat history of the East Antarctic Ice Sheet (EAIS) since the Last Glacial Maximum (LGM) is essential for understanding the response of the ice sheet to global climatic change and the mechanisms of retreat, including a possible abrupt melting event. Such information is key for constraining climatic and ice-sheet models that are used to predict future EAIS melting. However, data required to make a detailed reconstruction of the history of the EAIS involving changes in its thickness and lateral extent since the LGM remain sparse. The lack of geological constrain makes it difficult to estimate the mechanism of EAIS fluctuation and leads to uncertainty in predicting future EAIS melting.

The Soya Coast is located on the eastern side of Dronning Maud Land, East Antarctica, and faces the Cosmonauts Sea, including Lützow-Holm Bay. This geographic configuration is considered suitable for investigating the potential impact of ocean–ice interactions on the deglaciation of the EAIS. In addition, numerous numbers of glacial lakes in ice-free oases along the Soya Coast are suitable for reconstructing regional environmental changes and retreat history of the EAIS. The author conducted field-based geomorphological surveys on the southern Soya Coast during 2015–2016, 2017–2018 as

a part of the 57 and 59th Japanese Antarctic Research Expedition (JARE). This thesis presents a detailed ice-sheet history for the southern Soya Coast (Skarvsnes, Skallen, and Telen), Lützow-Holm Bay, East Antarctica, based on geomorphological observations, surface exposure ages, and lake sediments characteristics. This combined approach yields not only a timing of retreat, but also the more detailed reconstruction of the spatial variation of ice-sheet history and mechanism of the thinning and retreat of the EAIS.

Field-based geomorphological observations, surface exposure dating of erratic rocks, and lake sediment analysis, including high precision ^{14}C dating provide clear evidence for an abrupt thinning and retreat of the EAIS along the southern Soya Coast during the Early to Mid-Holocene (between 10 and 9 ka to 5.4 ka). These results also indicate that the ice-free areas (Skarvsnes, Skallen, and Telen) along the Soya Coast were all covered by the EAIS before deglaciation, most likely during the LGM. However, the exposure ages of bedrock from Skarvsnes (18010905 at 21.2 ka and 16012401 at 14.4 ka) show ages that are older than those of the erratic rocks. These differences in the exposure ages of the bedrock-erratic pairs from the same location suggest inheritance in the exposure ages of the bedrock acquired during ice-free periods prior to the last deglaciation. This interpretation is consistent with the difference in weathering features between

bedrock and erratic rocks. This indicates that the subglacial condition of the ice sheet that overlaid this area was nonerosive cold-based ice and/or warm-based ice, which not sufficiently to erode the bedrock to completely reset the inherited component of exposure ages. Although the author cannot directly constrain ice thickness during the last glacial period (certainly LGM), evidence from weathering features and inherited exposure ages of bedrock at Skjegget (400 m a.s.l.), Skarvsnes, provides the first-order estimation for the upper limit on the former ice sheet thickness that overlaid the summit of Skjegget less than ~300 m.

The timing of the abrupt ice-sheet thinning and retreat is probably consistent with the intrusion of modified Circumpolar Deep Water (mCDW) into deep submarine valleys in Lützow-Holm Bay, as inferred from a published record of fossil foraminifera data of marine sediment cores. Thus, the author proposes that the mechanism of the abrupt thinning and retreat of the EAIS along the southern Soya Coast was marine ice-sheet instability caused by the mCDW intrusion into the deep submarine valleys. Based on this hypothesis, the slight differences in the timing of the initiation of the ice-sheet retreat between the northern and southern sides of Skarvsnes can also be explained by the geographical configuration of this area. The Telen submarine valley, southern side of

Skarvsnes, is a large submarine valley with more than 1000 m deep, while the Honnör submarine valley is slightly shallower and smaller. This suggests that the Telen submarine valley is potentially more susceptible to the mCDW intrusion, which may cause earlier deglaciation in the southern side of Skarvsnes. On the other hand, the Skjegget, northern part of Skarvsnes, is directly facing to the Honnör submarine valley, which may have been more sensitive to the mCDW intrusion and to the ocean–ice-sheet interactions than the southern part of Skarvsnes. Therefore, the initiation of the ice sheet thinning of the northern part of Skarvsnes was slightly later, but the more abrupt thinning was thought to have occurred. The present study suggests that understanding of ocean–ice-sheet interactions to explain ice sheet behavior is important not only for West Antarctica but also for the Indian Ocean sector of East Antarctica.

Acknowledgment

First of all, the author appreciates Yusuke Suganuma (chief supervisor), Koichiro Doi (co-supervisor). Their insightful and inspiring instruction for the progress of the author's Antarctic field survey, research discussions, and this Ph.D. thesis was invaluable. Hideki Miura and Takanobu Sawagaki provided me helpful and constructive comments about Antarctic geomorphological research. Kota Katuki and Yuki Matsushi provide insightful and constructive comments about this Ph.D. thesis. The author thanks Kunihiko Nishizumi, Keiji Misawa, and Motohiro Hirabayashi for technical support during sample processing for surface exposure dating, and Yukino Ishii, Eriko Ota, Maki Kubo, Nobuyo Isemura, Mami Takehara, and Kenji Horie for assistance with sample preparation. The author also thanks Jun'ichi Okuno for constructive comments about the Glacial Isostatic Adjustment, and Ikumi Oyabu provided me with the Dome Fuji ice core data. Takamoto Nakano gave me various advices about Structure-from-Motion with Multi-View Stereo Photogrammetry processing of aerial photographs through the Geospatial Information Authority of Japan internship program. Takaharu Sato, Koji Seto, and Morimaru Kida gave me advice and comments about limnological study on Antarctica. Geoscience group members at the National Institute of Polar Research sometimes give me generously and

encourage comments about my study, especially Masakazu Fujii, Takeshige Ishiwa, Rei Kanemaru, and Akihisa Hattori.

The Antarctic field survey was conducted through support by the Japanese Antarctic Research Expedition (JARE). The author many thanks to the JARE members especially Akira Kadokura, Kazuo Higuchi, Nobuhiko Kizu, Matt Mutumi Sato, Takeo Mizutani, Kazuhiro Shibata, Hiroshi Watanabe, Makoto Shiobara, Kaoru Shiramizu, Takahiro Shimono, Masanao Sumiyoshi, Ryo Ohyama, Yukari Takeuchi, Eri Sasamori, Kody Patterson, Nozomu Matushima, Koji Mihara, Nobuaki Uchiyama, Jun Ikehara, Syo Shimamura, Daisuke Shibata, Yukiko Tanabe, Rachel Rudd, Shinpei Gotoh and Dale Anderson for support of my field observation and/or collecting samples. The author conducted a part of this study about lake sediments through a joint-use system at the Center for Advanced Marine Core Research, Kochi University (18B062) especially supported by Minoru Ikehara, Takuya Matsuzaki, and Nan Xiao. The author also thanks Takayuki Omori and Hiromasa Ozaki for ^{14}C dating sample processing and measured at the Laboratory of Radiocarbon Dating, The University Museum, The University of Tokyo. I acknowledge the PRIME Lab at Purdue University (USA) for conducting the ^{10}Be and ^{26}Al measurements.

This study was supported by partially funded by JSPS Kakenhi (19H00728, 16H05739, 17H06321, and 22500991), the TOREY Science Foundation, a Sasakawa Scientific Research Grant from The Japan Science Society (2019-6047), and NIPR through Advanced Project (KP-7 and KP306). ALOS/PRISM data were provided within the framework of JAXA ALOS-2 RA-6 (PI No. 3298).

Finally, I would like to thank my family for fully supporting my life. In addition, I appreciate Syuichiro Fujihira who is a high school teacher. He taught me the first basic instruction of earth science when I was a high school student. Without him, I would be nowhere. I dedicated this thesis to both of Takao Yamano and Minoru Hashimoto, my life mentors.

Contents

1. General introduction

1.1 Importance of geological constrain on the Antarctic Ice Sheet change

The Antarctic Ice Sheet (AIS) is a large freshwater reservoir which comprises an ice mass equivalent to 58 m of global sea-level rise (Fretwell et al., 2013) (Fig. 1-1). Its future evolution and the associated sea-level change are therefore of remarkably importance to global climate change, thorough the affect the coastal populations, ecosystems, and economies. In addition, the variability of the AIS due to ocean–ice-sheet interaction at the coastal area controls Southern Ocean sea-ice production and Antarctic Bottom Water production (e.g. Ohshima et al., 2013), and has a significant impact on the global climate system through the global heat distribution by the oceanic circulation (thermohaline circulation) (e.g. Johnson, 2008; Broecker, 2010). In the past five million years, global climate change in response to atmospheric CO_2 concentrations has been considered to have caused significant changes in the Antarctic ice sheet (e.g. Dutton et al., 2015), resulting in significant global sea-level changes such as the Pliocene Warmer period (e.g. Miller et al., 2020).

Over the past decades, accelerated ice-mass loss of the AIS has been reported through satellite measurements and oceanographic observations (e.g. Jacobs et al., 2011;

Rignot et al., 2011; Pritchard et al., 2012; Shepherd et al., 2012; Paolo et al., 2015; Rignot et al., 2019). The processes of the mass loss of the AIS are considered to be calving and basal melting of ice shelves (e.g. Depoorter et al., 2013; Dinniman et al., 2016). Particularly, the basal melting has been identified as a major contributor to the present ice-mass loss in West Antarctica, especially in the Amundsen and Bellingshausen seas (e.g. Pritchard et al., 2012; Joughin et al., 2014; Paolo et al., 2015; Jenkins et al., 2018). A key process of the enhanced basal melting is thought to be inflow of modified Circumpolar Deep Water (mCDW) to the continental shelf (e.g. Thoma et al., 2008; Jacob et al., 2011; Dinniman et al., 2012; Rignot et al., 2013; Liu et al., 2015; Nakayama et al., 2018). Thinning of ice shelves owing to basal melting is expected to have propagated into the continental ice sheet (Schoof, 2007; Golledge et al., 2012; Whitehouse et al., 2017) and to have accelerated the outflow of the ice sheet, thereby contributing to sea-level rise (Golledge et al., 2015, 2019; DeConto and Pollad, 2016). These phenomena suggest that understanding ocean–ice-sheet interactions in coastal areas of the AIS is important for interpreting contemporary ice-mass loss and for predicting future ice-sheet behavior. However, the length of several decades of the satellite and oceanographic observational records is too short to assess and capture the large-scale and potentially non-linear

(abrupt) response of the AIS to global climatic change, meaning that understanding of the mechanisms and drivers about the process enacting of abrupt deglaciation over this century and beyond is limited (Bentley, 2010).

An effective approach to understanding the mechanisms and drivers of large-scale and abrupt deglaciation is reconstruction of ice-sheet history based on investigation of glacial landforms and determination of the timing of the retreat using surface exposure dating (SED) along transects (both vertical and horizontal) in ice-free areas, especially for the period since the Last Glacial Maximum (LGM) (e.g. Stone et al., 2003; Bentley et al., 2017). Although several reconstructions of ice-sheet history have been made for the western Indian Ocean sector (Dronning Maud Land and Enderby Land), East Antarctica (e.g. Nishiizumi et al., 1991; Moriwaki et al., 1992; Altmaier et al., 2010; Yamane et al., 2011; Suganuma et al., 2014; White and Fink, 2014), the timing and magnitude of ice-sheet change there since the LGM remain unclear. As deglaciation of the AIS since the LGM is thought to have been spatially and temporally variable (Mackintosh et al., 2014; Small et al., 2019), regional geological constraints (e.g. vertical and/or horizontal transect chronology) on change in the AIS in various parts of Antarctica are needed, especially in coastal areas, to understand ocean–ice-sheet interactions and their impact on ice-sheet

dynamics.

Knowledge of the long-term history of the AIS is also required to estimate the current ice-mass balance based on satellite gravity measurements, as long-term glacial isostatic adjustment (GIA) has a significant effect on geodetic signals (e.g. Whitehouse et al., 2019). Owing to the lack of sufficient geological constraints on vertical and/or horizontal transect chronology in East Antarctica, current GIA model predictions in the Indian Ocean sector of the Antarctic continent show marked variation in the amplitude of isostatic uplift rates and their spatial distribution, ranging from 1 to 5 mm yr^{-1} (Ivins and James, 2005; Whitehouse et al., 2012; Briggs et al., 2014; Peltier et al., 2016). Moreover, the current crustal deformation rates in the Weddell Sea region observed by the Global Navigation Satellite System (GNSS) shows clear discrepancies from the GIA models, which is thought to due to assumption of the monotonic melting of the AIS during the mid-to-late Holocene used in these models (Bradley et al., 2015). As a result of the variation in the GIA models and their uncertainty, the modeled ice-sheet retreat history also contains significant uncertainty, which is directly linked to uncertainties in current estimates of the mass balance of the AIS and its contribution to contemporary sea-level rise. Therefore, detailed reconstructions of the history of the AIS since the LGM,

especially in Dronning Maud Land in the western Indian Ocean sector, are urgently needed.

1.2 Importance of understanding the ocean-ice sheet interactions since the Last Glacial Maximum for modern and future ice-sheet behavior

The Antarctic coastal region, especially in the Amundsen and Bellingshausen seas is currently experiencing ice mass loss due to the ocean–ice-sheet interactions (Shepherd et al., 2018; Rignot et al., 2019). Small et al. (2019) compiled the paleo-thinning rates of AIS since the LGM based on published SED data set from the Antarctic coastal region. Although the thinning rates are spatially variable, the fastest thinning occurred in regions that are characterized by currently experiencing significant ice mass loss, namely the Amundsen Sea and Antarctic Peninsula regions (Small et al., 2019). This suggests that similar mechanism(s) is thought to have operated to drive the currently ice mass loss in the past. Contemporary ice mass loss areas (the Amundsen Sea, the Bellingshausen Sea, and the Antarctic Peninsula) face the southernmost branch of the Antarctic Circumpolar Current (ACC) and thus associated CDW carried into continental shelves via submarine valley (Nakayama et al., 2018) (Fig. 1-1). These areas such as

Palmer Deep (Leventer et al., 2002), Pine Island Bay (Hillenbrand et al., 2017), and eastern Antarctic Peninsula (Etourneau et al., 2019) have been reported evidence of southward penetration of warm CDW during the early-mid Holocene based on the analysis of marine sediment cores.

On the other hand, the Soya Coast is located on the eastern side of Dronning Maud Land and faces the Cosmonauts Sea including Lützow-Holm Bay (Fig. 1-2a). The Lützow-Holm Bay sector (37˚–40˚E) is located near the eastern limb of the Weddell Gyre where the ACC begins to deflect southward (Vernet et al., 2019) (Fig.1-3). The continuous deep submarine valley in the Lützow-Holm Bay from the continental slope connects to the Soya Coast is the key local topographical feature for efficiently guiding offshore warm mCDW. Recent oceanographic observation indicates a high basal melt rate below the Shirase Glacier driven by the mCDW guided along the deep submarine valley (Hirano et al., 2020). The basal melting process associated with the mCDW advects onto the continental shelf and into the ice shelf cavities in Shirase Glacier, Lützow-Holm Bay is a similar mechanism to that of the contemporary ice mass loss in the West Antarctic region. Therefore, the Lützow-Holm Bay has a potential risk of rapid mass loss of the ice-sheet due to the intensified inflow of mCDW, similar to the modern trend of ice mass loss region

in West Antarctica.

The geographic configuration of Soya Coast is considered a suitable region for investigating the potential impact of the assess and capture the potentially non-linear (abrupt) response of the AIS caused by the ocean–ice-sheet interactions over the centennial-scale ice sheet behavior. In addition, numerous numbers of glacial lakes and marine fossils in raised beach distributed ice-free oases along the Soya Coast is a valuable area not only for reconstructing the ice-sheet retreat history but also available for reconstructing the regional environment and relative sea-level (RSL) change. On the basis of the faunal analysis of fossil foraminifera of marine sedimentary records, Igarashi et al. (2001) reported that mCDW intrusion into Lützow-Holm Bay during the Holocene might have contributed to ice-sheet retreat along the Soya Coast. However, the relationship between mCDW and ice-sheet retreat remains unclear because neither the timing nor magnitude of the retreat has been well constrained. Although four surface exposure ages have been obtained from one of the ice-free areas (Skarvsnes) of the Soya Coast (Yamane et al., 2011), the detailed ice-sheet history has not yet been reconstructed, which limits evaluation of the potential impact of ocean–ice-sheet interactions on the deglaciation of the AIS.

1.3 The aims and structure of the thesis

This thesis aimed to ascertain changes in the altitude and spatial extent of the AIS since the LGM on the southern Soya Coast (Skarvsnes, Skallen, and Telen), Lützow-Holm Bay, East Antarctica. Based on the reconstructed detailed ice-sheet history, the author examines the mechanism and driver that caused the thinning and retreat of the ice sheet in this region. To achieve these aims, the author carried out detailed field-based geomorphological observations in two austral summer seasons in Antarctica, from December 2015 to February 2016 and from November 2017 to February 2018, through the support of the Japanese Antarctic Research Expedition (JARE), and constrain the timing of ice-sheet thinning and retreat by newly determined surface exposure ages, and ^{14}C ages from lake sediments. Using these data, the author provides evidence for an episode of abrupt thinning and retreat of the AIS in this region over a short time interval between the Early (11.2–8.2 ka) and Mid (8.2–4.2 ka) Holocene. In addition, based on the bedrock weathering feature and inherited exposure age of bedrock, estimating the basal conditions and the first-order limit on the former ice sheet thickness (certainly LGM) that overlaid the summit of ice-free areas. The author also discusses the validity of

previously reported RSL fall associated with re-activation of a local fault, and discusses the history of lake systems associated with RSL changes after the ice sheet retreat. Finally, the author discusses the possible mechanisms and drivers of the abrupt ice sheet thinning and retreat along the southern Soya Coast, including the locations of currently ice-free areas (Skarvsnes, Skallen, and Telen) and the bathymetry of the adjacent areas.

2. Geomorphological setting and previous research at study area

2.1 Ice sheet configuration and geomorphological setting along the Soya Coast

The Soya Coast is a north–south-oriented ice-free coastal area extending for ~120 km along the eastern shore of Lützow-Holm Bay, Dronning Maud Land, East Antarctica (Fig. 1-2a). The ice-free areas are composed mostly of crystalline bedrock of gneiss (e.g. Ishikawa et al., 1977; Nakai et al., 1979; Osanai et al., 2004) and are separated by outlet glaciers, including Langhovde, Honnör, Telen, Skallen, and Vågs glaciers (Fig. 1-2b).

Raised beach sediments are widely distributed at ~20 m above sea level along the Soya Coast, and ^{14}C ages of marine fossils (shells, polychaete tubes, and foraminifera) in these sediments have been reported (Yoshida, 1983; Hayashi and Yoshida, 1994; Maemoku et al., 1997; Miura et al., 1998a, b, and c). Miura et al. (1998a) presented detailed descriptions of sedimentary structures and ^{14}C dates of in situ fossil shells of the fragile bivalve *Laternula elliptica* found in the sediments. ^{14}C ages obtained from the northern Soya Coast can be clearly divided into two age groups: Holocene (ca. 5–4 ka) and pre-35 ka. In contrast, ^{14}C ages from the southern Soya Coast show only Holocene ages (7–3 ka) (Miura et al., 1998a, c; Takada et al., 2003). Miura et al. (1998a) thus

concluded that the northern Soya Coast had not been covered by the East Antarctic Ice Sheet (EAIS) during the LGM, as the existence of pre-35 ka in situ fossil shells suggests that the ice sheet did not overlie the area after their burial. The limited extent of the EAIS during the LGM is considered to be consistent with the geomorphological features between the northern and southern Soya Coast. Bedrock is deeply weathered along the northern Soya Coast, whereas in the southern part, bedrock is unweathered, and ice erosion micro-topographic features, such as glacial striations, are clearly observed (Miura et al., 1998b). An alternative interpretation of these various characteristics, as proposed by Verleyen et al. (2017), is that the LGM ice sheet was nonerosive or cold based and was slow-moving over the Soya Coast area, which also accounts for the in situ fossil shells preserved in the raised beach sediments. In either case, the EAIS is thought to have overlain the southern Soya Coast during the LGM and then to have retreated during the Holocene (Miura et al., 1998a). This is consistent with the results of SED (10–6 ka) from the southern Soya Coast (Yamane et al., 2011).

In Lützow-Holm Bay, several conspicuous and deep submarine valleys exist immediately off the present ice streams along the Soya Coast (Moriwaki and Yoshida. 1983) (Fig. 1-2a). Igarashi et al. (2001) reported continuous recovery of calcareous

foraminifera, including *Bulimina aculeata*, from two sediment cores (81-110402 at water depth of 778 m and 81-110901 at water depth of 683 m) from the submarine valleys (Fig. 1-2b), indicating intrusion of mCDW into the valleys. Although the chronology of the cores was poorly constrained owing to the limited number of ^{14}C ages and anomalies may be caused by remobilization of the organic matter fraction caused by significant reworking and/or greater reservoir effect on phytoplankton material for bulk organic carbon (Domack and McClennen, 1996), calcareous foraminifera were observed to have a continuous distribution throughout the cores, indicating intrusion of warm, nutrient-rich, $CaCO_3$-saturated water; i.e., intrusion of mCDW from the offshore area via submarine valleys into the southeastern coast of Lützow-Holm Bay during the Holocene (Igarashi et al., 2001). In contrast, a large number of calcareous specimens, including *Bulimina aculeata*, were sporadically recovered from the core of SL-1 at a water depth of 393 m. The sporadic recovery of the calcareous foraminifera from SL-1 indicates an intermittent intensification of the mCDW intrusion, at least during the early Holocene. Hence, at least during the Holocene, the mCDW intruded towards the southeastern coast of Lützow-Holm Bay, and its intrusion sometimes intensified, thereby impacting coastal environments, especially the southern Soya Coast.

2.2 Previous research of the study area

Field-based geomorphological observations, rock sampling for SED, and coring the lake sediments, were carried out at three localities along the southern Soya Coast: Skarvsnes, Skallen, and Telen (Fig. 1-2b). The fieldwork focused on establishing transects and the features of distances from the current ice-sheet margin to reconstruct temporal variations in the altitude and spatial extent of the EAIS along the Soya Coast.

2.2.1. Skarvsnes

Skarvsnes is the largest ice-free area (63 km^2) along the Soya Coast (Yoshida, 1983), protruding from the ice sheet by ~12 km, and the maximum elevation in this area is 400 m a.s.l. (Skjegget) (Fig. 2-1). The submarine valleys of Honnör and Telen flank Skarvsnes (Fig. 1-2b). The geomorphology of this area is characterized by low hills, shallow linear depressions controlled by geological structure, and numerous lakes (Yoshida, 1983). Raised beaches containing marine fossils (shells, polychaete tubes, and foraminifera) are well developed in many places along the present shoreline and can be found up to 23 m above sea level (Hayashi and Yoshida, 1994).

Marine fossil ^{14}C dates obtained using accelerator mass spectrometry (AMS) range from 8860 to 2000 yr BP (Miura et al., 1998c and reference therein). On the basis of the oldest ^{14}C date (7170 yr BP) of in situ *Laternula elliptica*, Skarvsnes is estimated to have become ice free by at least ca. 7 ka (Miura et al., 1998a). Similarly, ^{14}C dates of lake sediment core bottoms obtained from Skarvsnes range from 7650 to 3050 yr BP (Takano et al., 2012; Verleyen et al., 2017). Assuming that ages of lake sediment core bottoms record the timing of ice-sheet retreat (e.g. Hodgson et al., 2001; Verleyen et al., 2004), Verleyen et al. (2017) estimated that Skarvsnes has been ice free from at least the beginning of the Mid-Holocene (around 7650 yr BP), consistent with the oldest ^{14}C dates of in situ *Laternula elliptica* (Miura et al., 1998a).

Yamane et al. (2011) determined the timing of ice-sheet retreat based on SED of four erratic rocks located close to the present ice-sheet margin at Skarvsnes (within ~5 km) (Fig. 2-1). Although temporal variations in the thickness and extent of the ice sheet were not well constrained by that study, Skarvsnes is thought to have been covered by a >360-m-thick ice sheet during the LGM and became ice-free between ca. 10 and 6 ka (Yamane et al., 2011).

Verleyen et al. (2017) reported a minimum marine limit of 32.7 m a.s.l. based on

a lake sediment core from Lake Kobachi-Ike and marine fossil, which is ca.10 m higher than previously published evidence in Skarvsnes, and at least 15 m higher than that reported in the other ice-free areas on Soya Coast. Because the GIA model predictions are unable to provide an explanation for the shape of the reconstructed RSL curve at Skarvsnes, Verleyen et al. (2017) favors an interpretation where the anomalously high marine limit and rate of RSL fall is due to reactivation of a local fault.

2.2.2. Skallen

Skallen is the third-largest ice-free area (14.4 km^2) along the Soya Coast (Miura et al., 1998c), protruding northwestward from the ice sheet and attaining a maximum height of 186 m a.s.l. (Fig. 2-1). This ice-free area is close to Skallen Glacier and the Telen submarine valley (Fig.1-2b). Skallen has a gently undulating surface with two main geomorphological elements that are separated by a wide east–west-trending valley and Lake Skallen Ô-Ike: a northern part with a maximum elevation of 186 m a.s.l. and a southern part with a maximum elevation of 142 m a.s.l.. Glacially eroded surfaces are better preserved than those of Skarvsnes and include striations, grooves, and small erosional marks (Sawagaki and Hirakawa, 1997). Raised beaches are found along the

eastern coast and around Lake Skallen Ô-Ike below ~15 m a.s.l. (Yoshida, 1983). Along the strandline of northeastern Skallen, unconsolidated sediments are distributed as several ridges that attain heights of up to 20–40 m (Hayashi and Yoshida, 1994). Hayashi and Yoshida (1994) concluded that these ridges are lateral moraines formed by Skallen Glacier, given their composition of mainly gravel and boulders and the lack of marine sedimentological features.

Lake Magoke-Ike is a glacier lake located on the southeastern side of Skallen (Fig. 2-2). Around Lake Magoke-Ike, gray silty-clay and sand sediments with abundant shell fragments are found (Igarashi et al., 1995; Maemoku et al., 2008). Two ^{14}C ages (3180 yr BP and 3790 yr BP) have been reported from fossil shell fragments (*Latanulla elliptica*) in the sediments (Igarashi et al., 1995). This sedimentary setting and the ^{14}C ages of the fossil shells can be explained by a re-advance of the EAIS during the Late Holocene (Maemoku et al., 2008).

^{14}C ages from fragmented marine fossils obtained from Skallen range from 7810 to 3180 yr BP (Igarashi et al., 1995). In addition, bottom sediment of Lake Skallen Ô-Ike has yielded a ^{14}C age of 7219 ± 41 yr BP (Takano et al., 2012). The ages suggest that the initiation of retreat of the EAIS occurred at least from the beginning of the Mid-Holocene

(ca. 7 ka) at Skallen.

2.2.3. Telen

Telen is a small ice-free area located to the east of Skallen and has a maximum elevation of 106 m a.s.l. (Fig. 2-3). Unlike Skarvsnes and Skallen, which protrude from the ice sheet as peninsulas, Telen is surrounded by Skallen and Telen glaciers and is located in the upper (terrestrial) part of the Telen submarine valley. Skallen Glacier flows to the NNW on the southern side of Telen, and Telen Glacier flows to the NW on the northern side. Several ridges of unconsolidated sediments are clearly developed, relating to the flanking glaciers. No geochronological constraints on ice retreat have been reported from Telen.

3. Methods

3.1 Geomorphological study

Geomorphological observations were carried out in two austral summer seasons in Antarctica, from December 2015 to February 2016 and from November 2017 to February 2018, through the support of the JARE. These observations focused mainly on the degree of weathering of bedrock and on the occurrence and orientations of glacial striations to obtain the basic information for discussing ice history. In addition, to improve knowledge of RSL change and lake history, a trench excavation survey of unconsolidated sediments near the Lake Oyako-Ike was conducted. The degree of rock weathering has been used in various studies as a proxy for the relative age of ice-sheet retreat (i.e., the length of time that the rock has been exposed) (e.g. Moriwaki et al., 1991, 1994; White et al., 2011; Suganuma et al., 2014; Kanamaru et al., 2018). Glacial striation orientations were measured by magnetic compass and assumed to indicate the direction of paleo ice-flow. Magnetic north in the study area was corrected to true north using the 50° west declination of the IGRF model (Thébault et al., 2015). The trench survey was excavated by manual shoveling on the utilize of gully perpendicularly to the step-like topographies named the Oyako-trench (Fig. 3-1). Altitude was measured by GRS-1 (TOPCON) and

handy leveling equipment, referring 21.274 m to ellipsoidal height of Skarvsnes (S69˚28', E39˚40') (Pavlis et al. 2012).

3.2 Surface exposure dating

3.2.1 Sampling for surface exposure dating

A total of 32 samples (29 from glacial erratic rocks and 3 from bedrock surfaces) were obtained for SED from Skarvsnes, Skallen, and Telen (Table 1). Altitudes and locations of the samples were measured using a handheld Global Positioning System device (GPSMAP 62s, GARMIN). Isolated boulders and mostly cobble-sized erratic rocks that appeared to be resting stably on bedrock or moraine were sampled to minimize the possibility of post-depositional movement and self-shielding. Most of the erratic rock samples were taken whole from the sampling sites. In contrast, the samples from the bedrock surfaces and some larger erratic rocks were collected by using a handheld electric cutter fitted with a diamond-tipped blade (Suganuma et al., 2012). The advantage of this method is that the sample can be obtained from a constant depth from the rock surface, thereby minimizing the component of age uncertainty attributable to sample shape heterogeneity. Samples were chosen while avoiding physical weathering, such as sheeting

and honeycomb weathering. The topographic shielding effect was measured using a handheld level at the sampling sites and calculated using the CRONUS-Earth online calculators (https://hess.ess.washington.edu/).

3.2.2 Laboratory analytical techniques

Rock samples were crushed and sieved to 250–500 μm size (with the 250–1000 μm size fraction being used for samples 15123102 and 17122702) to obtain 40–60 g of clean quartz grains for SED analysis. Elements Be and Al were selectively extracted from the clean quartz grains at the National Institute of Polar Research, Tokyo, Japan, following established methods (Kohl and Nishiizumi, 1992; Bierman et al., 2002). In order to accurate determination of the ^{27}Al concentration in quartz, a part of the sample solution had separated during the experimental processing and used for ^{27}Al measurement by inductively coupled plasma–mass spectrometry (ICP-MS). The weights of the samples and carriers listed in Table 2 show residual weights for AMS measurement after aliquoting for ^{27}Al measurement. ^{10}Be/^{9}Be and ^{26}Al/^{27}Al ratios were measured using clean quartz grains of 40–60 g at the Purdue Rare Isotope Measurement (PRIME) Laboratory, Purdue University, US (Table 2). Measurements were normalized to the 07KNSTD Be

standard material with nominal $^{10}Be/^{9}Be = 2.851 \times 10^{-12}$ (Nishiizumi et al., 2007) and to the KNSTD Al standard material with nominal $^{26}Al/^{27}Al = 1.818 \times 10^{-12}$ (Nishiizumi, 2004). Procedural blanks (n = 5) and samples were both spiked with ~0.5 mg ^{9}Be carrier (Be carrier, 347.5 μg Be/g). Blanks were spiked with ~1.5 mg ^{27}Al carrier (Al carrier, 728 ppm), and samples were spiked with ca. 1.0 mg ^{27}Al carrier with the value depending on the native Al content of the sample. Blanks ranged from 3×10^{-15} to 30×10^{-15} [$^{10}Be/^{9}Be$] and 1×10^{-15} to 12×10^{-15} [$^{26}Al/^{27}Al$]. Concentrations reported in Table 2 involved subtraction of background ^{10}Be and ^{26}Al atoms measured in one procedural blank (Table 2 and 3). Uncertainties include a propagated AMS sample/lab-blank uncertainty, and a 3% uncertainty reflecting stable ^{27}Al measurement by ICP–MS. Unfortunately, ^{26}Al determinations for some samples were unable to be properly measured by AMS owing to interference by high concentrations of ^{26}Mg.

3.2.3 Exposure age calculations

Surface exposure ages were calculated using the CRONUS-Earth V3 (http://hess.ess.washington.edu/math/v3/v3_age_in.html) online calculators (Balco et al., 2008). Exposure ages were calculated using a ^{10}Be half-life of 1.387 Ma (Chmeleff et al.,

2010; Korschinek et al., 2010) and an ^{26}Al half-life of 0.705 Ma (Nishiizumi., 2004) with the CRONUS-Earth production rates (Borchers et al., 2016) and employing the Lal–Sato–Dunai nuclide-specific (LSDn) scaling scheme (Lifton et al., 2014). Rock density was assumed to be 2.7 g cm^{-3} for quartz-bearing erratic rock and bedrock samples. Multiple-isotope (^{10}Be and ^{26}Al) cosmogenic nuclide data are useful for understanding either single-exposure (simple-exposure) or complex-exposure and burial ice-sheet histories (Jones et al., 2017). In this study, ^{10}Be-based exposure ages were used as the main basis for interpretation and discussion because the production rate of ^{10}Be is better constrained than that of ^{26}Al (Gosse and Phillips, 2001). ^{26}Al-based exposure ages were used to check their correspondence to ^{10}Be-based exposure ages (within error ranges), considering the possible problems relating to sample selection and collection, and to validate the experimental accuracy of quantification of nuclides. All ages are apparent exposure ages, which means that an inherited component might be included. In addition, the age determinations assume that the samples did not undergo self-shielding by rolling and were unweathered, which was handled by collecting erratic rocks resting stably on bedrock or moraine with little surface weathering. The author made no attempt to account for the minor variation in production rate caused by GIA, as any influence on age by elevation

changes associated with GIA of the Soya Coast is very limited (up to 1%–2%) (Jones et al., 2019). The SED results published for Skarvsnes (Yamane et al., 2011) were recalculated using the same procedure as described above. Uncertainties in SED in this study derive from external errors, including scaling and production-rate uncertainties, as well as internal uncertainties (concentration uncertainties based on laboratory/AMS measurements).

3.3 Lake sediment core

3.3.1 Collecting for lake sediment cores

Lake sediments were collected from ice-covered lakes using a new portable engine-driven percussion piston corer during the 59th Japanese Antarctic Research Expedition (November 2017–December 2017). The engine-driven percussion coring equipped with a core-catcher is believed to have penetrated to the bed-rock of lakes, and available to obtain relatively coarse and hard sediments (Fig. 3-2). The main body of the corer is composed of a transparent polycarbonate pipe with an external diameter of 76 mm, which allows us to check length and facies of the sediments immediately after coring (Suganuma et al., 2019).

3.3.2 Description and physical analyses of the Lake sediments

The author descripts the lithological composition, sedimentary structures, and measurement the physical properties for lake sediment cores. The physical properties of core samples measured by the Multi-Sensor Core Logger (MSCL) which commercially available tools for gathering all these data automatically without destruction. By moving a core sample through sensors using a conveyor belt-like mechanism, it is possible to continuously acquire physical property data such as fractional porosity, and magnetic susceptibility. In addition, it three-dimensionally analyzes the sedimentary structure of core samples without destruction by applying medical X-ray computer tomography (CT) scan techniques for core samples. X-ray CT and MSCL measurements were conducted at the Center for Advanced Marine Core Research, Kochi University.

3.3.3 Radiocarbon dating

Bottom age of the lacustrine/marine sediments of isolation basins provide minimum ages of initial ice-sheet retreat. In order to estimate the minimum age for the deglaciation, bulk sediment samples from lake sediment core and marine fossils in raised

beach were dated by using the compact AMS system of the Laboratory of Radiocarbon Dating, The University Museum, The University of Tokyo, Japan. First, bulk sediment from each lake sediments were digested with 1M HCl (80˚C, over 3 days) and changing the solution on each day. After the sediments were digested with 1M HCl, rinsed free of mineral acid with distilled water (Milli-Q water) to a neutral pH and freeze dried. The marine fossils (polychaete tube and fossil shell) were reaching with 0.1M HCl after ultrasonic washing in Milli-Q water. These acid processing conducted at the National Institute of Polar Research, Tokyo, Japan. Then, these samples were weighed in a silver cup and combusted to form CO^2 using a Vario ISOTOPE SELECT elemental analyzer (Omori et al., 2017). The CO^2 was introduced into a vacuum line and sealed in a reaction vessel with sufficient H^2 (2.2 times the amount of CO^2) and 2 mg of iron powder for catalysis. The graphite was reduced on the surface of the catalyst at 650°C for 6 h. Reduced graphite was pressed in an aluminum holder for AMS analysis. These graphitization processing and AMS analysis were performed at Laboratory of Radiocarbon Dating, The University Museum, The University of Tokyo. A series of international standards were simultaneously measured, and $\delta^{13}C$ measured by AMS was applied to correct the isotopic fractionations during preparation and measurement to

calculate the conventional radiocarbon age (Stuiver and Polach, 1977).

The results are reported as conventional radiocarbon years BP with one-sigma (1 σ) standard deviation error (Table 4). The ^{14}C ages of bulk lake sediments and marine fossils from raised beach (polychaete tube and fossil shell) were calibrated using the same way as Verleyen et al. (2017). The ^{14}C ages from the marine sediment unit in the Lake Oyako-Ike and marine fossils were calibrated using the Marine13.^{14}C calibration curve in CALIB 7.1 (Reimer et al., 2013) using a Delta R of 720 years, leading to a total correction of 1120 years as recommended for the region (Yoshida and Moriwaki, 1979). An error of ±100 years for the reservoir effect was calculated based on the Yoshida and Moriwaki (1979) ages. The lacustrine lake sediments which thought to be deposit under the flesh water environment, using the terrestrial SHCal13.^{14}C calibration curve (Hogg et al., 2013). In contrast to the marine sediment and marine fossil samples, no reservoir correction was applied to ages from lacustrine sediments following other previous research of the East Antarctic lake sediments (e.g. Hodgson et al., 2001; Verleyen et al., 2011).

3.4 Generation of a detailed digital surface model

In order to identify the micro-landforms for spatial area, the author newly produce the high-resolution digital surface model (DSM). The Geospatial Information Authority of Japan (GSI) has a record of aerial photographs for Soya Coast taken by the JARE. The author used Structure from Motion with Multi-View Stereo (SfM–MVS) photogrammetry to produce high-resolution DSM based on the archived airborne photographs taken during the 34th JARE in 1993 at Skarvsnes. SfM–MVS is a method for the construction of three-dimensional data of objects from two-dimensional photographs (Szeliski, 2010). This method has recently been used for geomorphological research for acquiring detailed topographical data. For the present research, the author has used the 338 color photographs available free of charge (400 dpi). This set of aerial photographs covers the totality of Skarvsnes providing a pixel resolution of 0.7 m.

Using Agisoft Photoscan Pro, the DSM was produced by the following procedure. (1) 70 tie-points (ground control points: GCP) were added using previously published DSM, which is about 10 m resolution made by GSI (GSI-DSM). GCPs are added in the landscape, such as shoreline and top of the hill uniformly. (2) Then a 3D "pointcloud" was extracted from the photographs, (3) and a dense pointcloud was calculated from the sparse pointcloud, before being turned into (4) a mesh that has been

wrapped with a mosaic of the aerial imagery. Then, this mapped 3D was converted into a DSM and an orthophotograph (Fig. 3-3).

Although a col-shaped distortion was identified in the generated DSM (SfM–DSM), this was reduced by correcting the 3D surface trend estimation of the distortion by using the “grdtrend” component of the Generic Mapping Tools software package (GMT). This program locally fits a polynomial curved surface to the original DSM to identify a trend of distortion and then removes it. Then, the author succeeded in creating a SfM–DSM with 1.4 m resolution, which is sufficient for the identification of micro landforms that ever could not interpretation the former DSM (GSI-DSM) with 10 m resolution (Fig. 3-4).

4. Results

4.1 Geomorphology

4.1.1. Skarvsnes

Skjegget (400 m a.s.l.) is an asymmetrical peak located in the northwestern part of Skarvsnes (Figs. 2-1 and 4-1). This peak is a cliff on its southwest side, but the northeast slope is relatively gentle. Differences in the degree of weathering of bedrock surfaces on Skjegget are clearly observed with elevation change. The bedrock at and near the summit is strongly honeycomb weathered (Fig. 4-2a), similar to that of the northern Soya Coast, where fossil shells older than the LGM (pre-35 ka ages) have been reported (Maemoku et al., 1997; Miura et al., 1998b). In contrast, elevations of 250–300 m a.s.l. are characterized by less intense physical weathering, with honeycomb weathering becoming inconspicuous, and smooth surfaces dominating (Fig. 4-2b).

Mt. Suribachi-Yama (258 m a.s.l.) is a large rocky hill measuring ca. 1500 m long and 300 m height in the central part of Skarvsnes. This hill is interpreted as a particularly large roche moutonnée (Sawagaki and Hirakawa, 1997, 2002b) (Fig. 2-1). In contrast to the highly weathered bedrock surface at the top of Skjegget (400 m a.s.l.), the bedrock surface on Mt. Suribachi-Yama is relatively unweathered and shows striations

(oriented N60°W) (Fig. 4-2c). Cross-cut striations (N100°W overlapping N50°W) are clearly seen at lower altitudes on the southeastern (ice sheet) side of Mt. Suribachi-Yama (Fig. 4-2d). The cross-cut striations suggest that the direction of ice-sheet flow changed from N50°W to N100°W.

Mt. Shirasuso-Yama (362 m) is the second-highest peak, is located in the eastern part of Skarvsnes, and is closer to the present ice-sheet margin than Skjegget and Mt. Suribachi-Yama (Fig. 2-1). Bedrock weathering of Mt. Shirasuso-Yama is characterized by relatively weak physical weathering from the base to near the summit of the mountain and by striations at the peak (Fig. 4-2e). These weathering features differ from those at Skjegget. The orientations of glacial striations change from west (N90°W–100°W) on the southeastern side of Mt. Shirasuso-Yama to northwest at the summit (Fig. 4-2f). The striae directions of Mt. Suribach-Yama and Mt. Shirasuso-Yama, southern side of Skarvsnes, show a change in ice-sheet flow direction from NW–SE to W–E. This is consistent with the shift from the overlaid ice sheet to valley glaciers, as ice thinned toward the modern-day profile.

Lake Oyako-Ike is located on the saddle of a narrow U-shaped valley connecting Torinosu-Cove and Osen (Fig. 4-3a). Lake Oyako-Ike is presently separated from the

open ocean by sills with heights (outflowing points) of 2.37 ± 0.01 m a.s.l. (Takano et al., 2012). The marine sediments of the valley were distributed above the present shoreline up to 15 m a.s.l. (Miura et al., 1998 c), representing that the valley was once a strait connecting Torinosu-Cove and Osen. Glacial striations were observed in the same direction (N 50˚W) at an altitude of about 150 m a.s.l at the western peak and 222 m a.s.l. at the eastern peak of Lake Oyako-Ike. On the other hand, on the flat surface in the middle of the eastern peak of Lake Oyako-Ike, the N110˚W striation overlap that oriented N50˚W (Fig. 4-3b), indicating that the direction of ice-sheet flow changed from N50˚W to N110˚W, consistent with the lowering of the ice-sheet as ice thinned toward the U-shaped valley connecting Torinosu-Cove and Osen (Fig. 4-3c).

In order to consider the initiation of the lake and its history of environmental change, the author conducted an intensive survey at raised beach surround Lake Oyako-Ike (Fig. 3-1). Oyako-trench with 7 m in length and ca. 0.5 m in depth is located at 30 m westward of the Lake Oyako-Ike. The raised beach sediments observed in the trench are composed of well-sorted fine to medium-grained sand, intercalated with pebble-sized gravel layers, and contain abundant marine fossils (a polychaete tube). Based on the sedimentary facies and occurrences of the marine fossils, the beach deposits are thought

to be formed by the shallow-marine environment.

4.1.2. Skallen

Glacial striations and smooth surfaces on bedrock are well preserved at Skallen. These features show no variation with altitude or with distance from the present ice-sheet margin, in contrast to those at Skarvsnes. Orientations of the glacial striations change from SE–NW to SSE–NNW from the western to eastern parts of Skallen (Fig. 2-2). In addition, the SSE–NNW-oriented striations overlap those oriented NW–SE at several sites (Fig. 4-4a), indicating that the direction of ice-sheet flow changed from NW to NNW, consistent with lowering of Skallen Glacier as ice thinned toward the modern-day profile.

4.1.3. Telen

Orientations of glacial striations at Telen are mainly N–S (Fig. 4-4b), consistent with the current flow direction of Skallen Glacier. Striations and small erosional marks (sculpted erosional forms: s-forms) are clearly observed (Fig. 4-4c). The bedrock weathering features and glacial landforms, including s-forms, are similar to those at Skallen. Several ridges along the strandlines of Skallen and Telen Glaciers are composed

of unconsolidated sediments, such as gravel and boulders, mixed with fine materials and are almost certainly lateral moraines formed by each glacier (Fig. 4-4d).

4.2 Surface exposure dating

4.2.1. Skarvsnes

18 erratic rocks and two bedrock surfaces were sampled and analyzed for SED through an elevation range of 47–400 m a.s.l. at Skarvsnes (Figs. 2-1, 4-5a, and b). The surface exposure ages from the erratic rocks lie predominantly in the range 9.7–6.5 ka and show a getting young with decreasing elevation (Figs. 4-1, 4-5a, and b). Bedrock surfaces yielded older ages, namely, 21.2 ka and 14.4 ka (Fig. 2-1). The bedrock samples were collected from relatively unweathered surfaces at the summit of Skjegget and near the summit of Mt. Suribachi-Yama, with the latter sample being collected from where striations were observed (Fig. 4-2c).

4.2.2. Skallen

Six erratic rock samples were collected from 7–140 m a.s.l. along two transects on the northeastern and southeastern sides of Skallen, facing Skallen Glacier (Figs. 2-2

and 4-5c). Rock sample 18012812 was taken from the eastern edge of moraine ridges in northeastern Skallen (Fig. 4-4e), with the other five samples being taken from on top of bedrock. In addition, erratic rock sample 15123101 and bedrock sample 15123102 were collected from the same location on the western flank of Mt. Himi-Yama to ascertain subglacial conditions, with the bedrock sample being collected from a flat surface with striations (Fig. 4-4f). Surface exposure ages of the samples from Skallen range from ca. 8 to ca. 5 ka, except for one young sample (18012709: 1.5 ka). This young rock sample 18012709 is collected from 7 m a.s.l which is lower than the maximum sea-level height inferred by the raised beach sediments (Yoshida, 1983). However, the relative sea-level at 1.5 ka in Skallen is estimated to be up to ca. 4 m a.s.l. (Verleyen et al., 2017). Thus, the rock sample 18012709 is most likely glacial in origin. The ages of the erratic rock and bedrock samples from western flank of Mt. Himi-Yama are consistent within error (Fig. 2-2).

4.2.3. Telen

Four erratic rocks (two samples situated on bedrock and others situated on moraine) were sampled from Telen. The sampling elevations cover 4 to 91 m a.s.l., and

exposure ages range from ca. 6.6 to 0.2 ka (Fig. 2-3). Although the height (4 m a.s.l.) of two samples with young ages (16011201 at 0.6 ka and 16011202 at 0.2 ka) is certainly lower than the maximum sea-level in the area (Yoshida, 1983), they are thought to be glacial in origin. This is because they are from large boulders on the moraine ridge, which are not considered to be ice rafted debris. In addition, the sea-level in this area is thought to become lower than 4 m a.s.l. after 0.6 ka (Verleyen et al., 2017). The ages show a getting young with decreasing elevation (Fig. 4-5d). The two exposure ages (16011201 at 0.6 ka and 16011202 at 0.2 ka) from the erratic rocks of moraine along Skallen Glacier are younger than those of Skarvsnes and Skallen.

4.4 Lake sedimentary lithostratigraphy and ^{14}C age

4.4.1 Lake Naga-Ike

Lake Naga-Ike (S69°29.24' E39°35.84') is a small lake on Skarvsnes (Fig. 2-1). A 130 cm sediment core was collected from water depth of 10.3 m at the center of this lake. The core was thought to reach to the bedrock, or very rigid, consolidated sediment underneath of the soft lake sediment. The core mainly contains two lithostratigraphic units: a minerogenic sandy clay (NG1) and an overlying highly organic laminated

microbial mat (NG2) (Fig. 4-6a). The NG1 is a 12 cm (118–130 cm) thick olive-black fine and medium sand with occasional granules (NG1). The NG1 is conformably overlayed by a 118 cm (0–118 cm) of the organic laminated microbial mat, varying between olive-black, gray, and light-yellow (NG2). In addition to the lithostratigraphic change, the transition between NG1 and NG2 is marked by a very rapid decrease in magnetic susceptibility and relatively low porosity. Bulk sediment samples were taken from four horizons of the core for ^{14}C dating. A ^{14}C age of the bottom of the core yields an age of 7641 cal. yr BP and the age got younger with the upper part. The depth of 60 cm age in the lake yielded an age of 6446 years. If this age is adopted, the sedimentation rate changes significantly after 60 cm depth in unit NG2 (about 0.1 mm/yr above 60 cm depth and 0.6 mm/yr below), but the lithostratigraphy and magnetic susceptibility of NG2 do not indicate a significant change in the depositional environment.

4.4.2 Lake Hyoutan-Ike

Lake Hyoutan-Ike (S69°29.15' E39°36.75') is located near the Lake Naga-Ike on Skarvsnes (Fig. 2-1). A 134 cm sediment core was collected from water depth of 9.7 m at the center of this lake. The core was thought to reach to the bedrock, or very rigid,

consolidated sediment underneath of the soft sediment. The core contains two sediment lithostratigraphic units: a minerogenic sandy clay (HY1) and overlying highly organic laminated microbial mat (HY2) (Fig. 4-6b). The HY1 are made of two sub-units: lower sub-unit is a 4 cm (130–134 cm) thick grey to medium sand, with occasional granules (HY1i). This sub-unit is conformably overlain by 12 cm (118–130 cm) of olive-grey massive fine sand (HY1ii). The HY2 is also made of two sub-units: the lower sub-unit is a 15 cm (103–118 cm) unit of weak laminated, silty sand varying between olive-grey, olive-black, and dark-olive (HY2i). This sub-unit is conformably overlayed by a 103 cm thick-laminated microbial mat, varying between olive-black, dark-olive, and olive-yellow (HY2ii). In addition to the lithostratigraphic change, the transition between HY1 and HY2 is marked by a very rapid decrease in magnetic susceptibility and relatively low porosity. Bulk sediment sample was taken from the top and the bottom of HY2 for ^{14}C dating. The bottom of the HY2 sample yielded an age of 8071 cal. yr BP. Although dating was also performed from the HY1 horizon, the carbon content was too low to be dated.

4.4.3 Lake Namazu-Ike

Lake Namazu-Ike (S69°29.93' E39°41.79') is located in southeastern Skarvsnes (Fig. 2-1). A 135 cm sediment core was collected from water depth of 11.1 m at the center of this lake. The core mainly contained two sediment lithostratigraphic units: a minerogenic sand with gravel (NZ1) and a highly organic laminated microbial mat (NZ2) (Fig. 4-6c). NZ1 made of two sub-unit units: the lower sub-unit is a more than 9 cm (110–125 cm; under the 125cm collapsed) thick sub-unit of unconsolidated, mainly subangular gravel about 2mm to 10mm in diameter with less matrix (NZ1i). Also, the depth of 116 cm contains the biological mat. NZ1i was sharply but conformably overlayed a by 6 cm (104-110 cm) of fine sand (NZ1ii). NZ1ii was conformably overlayed by a 104 cm (0–104 cm) of the laminated microbial mat, varying between olive-gray and purplish-black (NZ2). In addition to the visual stratigraphy, the transition between NZ1 and NZ2 is marked by a very rapid decrease in magnetic susceptibility and relatively low porosity. Bulk sediment samples were taken from four horizons of the core for ^{14}C dating. The uppermost and lowermost parts of this lake were dated from both bulk sediments and biological mat. The bottom of the NZ2 was 6201 cal. yr BP, but the lower part of the NZ1 showed a younger age of around 1 to 2 ka as almost the same as the top of the core.

4.4.4 Lake Oku-Ike

Lake Oku-Ike (S69°29.88’ E39°37.57’) is a small lake on Skarvsnes (Fig. 2-1). A 137 cm sediment core was collected from water depth of 6.0 m the center of this lake. The core was thought to reach to the bedrock, or very rigid, consolidated sediment underneath the soft lake sediment. The core mainly contains two lithostratigraphy units; a minerogenic sand (OK1), and an overlying highly organic laminated microbial mat (OK2) (Fig. 4-6d). The OK1 is a 28 cm (109–137 cm) thick of olive-grey and olive-black, mainly coarse sand containing medium sand unit. The OK1 is conformably overlain by 109 cm (0–109 cm) of the organic laminated microbial mat, varying between olive-black, dark-olive, and olive-yellow (OK2). In addition to the visual lithostratigraphy, the transition between OK1 and OK2 is marked by a very rapid decrease in magnetic susceptibility and relatively low porosity. Bulk sediment sample was taken from four horizons of the core for ^{14}C dating. The bottom of the OK2 sample yielded an age of 7176 cal. yr BP. The bottom age of the OK1 that composed of organic laminated microbial mat unit is 5523 cal. yr BP. This age relatively close to that of the bottom of the NZ2 (6201 cal. yr BP) composed of almost same lithofacies of laminated microbial mat unit.

4.4.5 Lake Oyako-Ike

Lake Oyako-Ike (S69°28.53' E39°36.10') is presently separated from the open ocean by sills with heights (outflowing point) of 2.37 ± 0.01 m a.s.l. (Takano et al., 2012) on Skarvsnes (Fig. 2-1, 3-1). A 487 cm sediment core was collected from water depth of 8.6 m at the center of this lake. Five distinct lithostratigraphy units were identified in the Lake Oyako-Ike sediment core (Fig. 4-7). The lowermost of these (OY1) were made of two sub-units: the first is a 13 cm (474–487 cm) thick unit of unconsolidated, silty sand with granite (OY1i). The OY1i was conformably overlain by 37 cm (437–474 cm) of dark greenish-grey laminated silty sand (OY1ii), and there are no marine fossils observed within OY1. The OY2 is a 142 cm (295–437 cm) thick lithostratigraphy unit of once again dark layer of dominated sandy silt including marine fossils (sea urchin spine and polychaete tubes) and alternate the silty sand with granule, and terminates with a shift to weak laminated silty sand and sandy silt. Above the OY2, the OY3 is overlain with a 117 cm (178–295 cm) thick unit dominated by silty sand and sandy silt with the rarely including granite. The OY3 abundances the sea urchin and fossil shells than other parts of this core. The OY4 is a 168 cm (10–178 cm) thick unit mainly composed of silt including marine fossils (fragmented fossil shells). The upper part of this unit is composed

of relatively high organic sandy silt. The upper most lithostratigraphy unit of this core (OY5) is the organic laminated microbial mat. In addition to the visual stratigraphy, the magnetic susceptibility is also useful proxy to capture the transition of each unit. A bulk sediment sample was taken from five horizons of the core for ^{14}C dating. The lower of the OY2 sample yielded an age of 8542 cal. yr BP. Judging from the ^{14}C ages from five horizons the core, the sedimentation rate during the OY2 was faster than in the other units, and the rate decreased toward OY3. Because marine fossils are produced at the unit of OY4, the age of four samples correct at depths below OY4 were calibrated using Marine13 with a local reservoir. On the other hand, the present Lake Oyako-Ike is completely freshwater (Kimura et al., 2010; Kida et al., 2019), the ages collected from the uppermost part of the Lake Oyako-Ike were calculated using SHCal13 same as other lakes. The 14C ages of two polychaete tubes and a fragment of fossil shell in the trench near the Oyako-Ike are 6821 ± 28, 6841 ± 26, and 7445 ± 29 yr BP, respectively (Fig. 3-1).

5. Discussion

5.1 Interpretation of geomorphic features, exposure ages and sedimentary cores

5.1.1 Geomorphic features and exposure ages

In order to interpret the range of ice-sheet thinning and retreat and subglacial conditions along the southern Soya Coast, the author considers the relationship of each sample location, exposure ages, and geomorphological features. The exposure ages of bedrock from Skarvsnes (18010905 at 21.2 ka and 16012401 at 14.4 ka) show ages that are older than those of the erratic rocks. These disparities can be explained by inheritance acquired during ice-free periods prior to the LGM.

The bedrock with the oldest exposure age, from the summit of Skjegget (18010905 at 21.2 ka), is characterized by strong honeycomb weathering (Fig. 4-2a). No striations or glacial polish were observed on the bedrock surface at elevations of >300 m a.s.l. at Skjegget. At this site, the bedrock sample is clearly older than the erratic rock (18010904 at 8.9 ka) in close proximity. Fresh erratic rocks with younger exposure ages on highly weathered bedrock have been explained in terms of being covered by the cold-based AIS (Sugden et al., 2005; Mackintosh et al., 2007; White and Fink, 2014). Because a cold-based ice sheet is less erosive (cf. a warm-based ice sheet) and thus unable to

remove the surface of bedrock, the weathering state of the bedrock before the last ice advance is thought to have been preserved at Skjegget.

In contrast, the bedrock (16012401) of Mt. Suribachi-Yama is relatively unweathered and partially striated and yielded a slightly younger exposure age (14.4 ka) compared with the summit of Skjegget (Fig. 4-2c). Geomorphological evidence suggests that subglacial conditions at Mt. Suribachi-Yama were warm based, which would have eroded the bedrock surface, although not sufficiently to remove bedrock down to the ~2 m that is needed to completely reset the inheritance of cosmogenic nuclides (Gosse and Phillips, 2001). Thus, the difference in exposure ages from the bedrock surfaces between Skjegget and Mt. Suribachi-Yama indicates that Skarvsnes was covered not only by cold-based ice sheets during the LGM. The clear transition from weathered to fresh bedrock observed at Skjegget is considered to represent a transition in subglacial conditions from cold- to warm-based ice during the LGM possibly due to the ice thickness.

Unlike at Skarvsnes, the bedrock (15123102 at 6.6 ka) at Skallen provides an identical exposure age to that of the sampled adjacent erratic rock (15123101 at 7.0 ka). In addition, streamlined bedforms and s-forms are well preserved around these sampling sites and are thought to have been formed by subglacial meltwater (Sawagaki and

Hirakawa, 1997). These features suggest that subglacial erosion at Skallen was more intense than that at Skarvsnes and was significant enough to completely remove any preexisting cosmogenic nuclides in the bedrock. Therefore, subglacial conditions along the southern Soya Coast were not uniform and instead were likely to be highly dependent on ice thickness; i.e., on the relationship between terrain altitude and distance from the ice sheet.

The exposure ages of the sampled erratic rocks allow inferences to be made regarding the timing of thinning and retreat of the EAIS along the Soya Coast. Exposure ages from Skjegget at Skarvsnes show a progressive younging with decreasing elevation, from 8.9 ka at the peak (400 m a.s.l.) to ca. 6.5 ka at ~50–150 m a.s.l. (Fig. 4-1). In addition, the exposure ages of erratic rocks close to the present ice-sheet margin (e.g. 16012201, 16012503, and 16012501) are also ca. 10–7 ka (Fig. 2-1). These results suggest that the ice sheet completely covered Skarvsnes (400 m a.s.l.) prior to ~10 ka and retreated by at least ~10 km over a period of a few thousand years during the Early to Mid-Holocene (between 10 and 9 ka to 6.5 ka). In addition, the ice retreat is thought to be started slightly earlier on the southern side of Skarvsnes, whereas the ice retreat in the northern site might start later, but it was more significant (rapid) than that of the southern

side (Fig. 4-5a and b).

At Skallen, the exposure ages of erratic rocks lie mainly in the range ca. 8–5 ka. The exposure age from the highest site (17122702 at Mt Himi-Yama) is 6.6 ka and is younger than exposure ages (18012805 and 16010601) from the northern part of Skallen, despite lying at lower altitudes than 17122702. As Mt. Himi-Yama is close to the present ice-sheet margin which located ca. 1 km north from the current ice sheet margin (Fig. 2-2), the slightly younger age can be explained in terms of the terrain having been exposed far from the current ice sheet margin. An exposure age obtained erratic rock from just below the summit at Telen (16010902 at 91 m a.s.l.) indicates that Telen had started to become ice free at 6.6 ka. As the older exposure age (4.2 ka) was obtained from a relatively higher site (16010901 at 68 m a.s.l.) (Fig. 4-5d), the ice-sheet lowering rate at Telen is interpreted as having been smaller than that at Skarvsnes and Skallen (Fig. 4-5d). Cross-cutting striations found at Skarvsnes and Skallen (Figs. 4-2d and 4-4a) are inferred to have been produced by a change in the direction of ice flow, controlled by the configuration of bedrock topography, during the ice-sheet thinning, which is consistent with the progressive younging of exposure age with decreasing elevation.

The inferred timings of ice-sheet retreat at Skallen (ca. 8–5 ka) and Telen (< ca.

7 ka) are slightly younger than that at Skarvsnes (ca. 10–6 ka). Altitudes of exposure ages from the highest sites at Skallen (140 m a.s.l.) and Telen (91 m a.s.l.) are much lower than those from Skarvsnes (400 m a.s.l.), suggesting that an initiation of the thinning of ice-sheet at Skallen and Telen can be older than the exposure ages obtained from these localities.

These differences in the timing and magnitude of ice retreat are likely controlled the geographical configuration, especially relationship with the submarine valleys. In order to verify this hypothesis, a Monte Carlo linear regression analysis using the MATLAB® model "iceTEA" (http://ice-tea.org; Jones et al., 2019) is used to estimate a magnitude and rate of ice surface lowering. The rates of ice surface lowering for facing to Honnör submarine valley areas (northern side of Skarvsnes), facing to Telen submarine valley (southern side of Skarvsnes and Skallen) (only southern side of Skarvsnes) are generated from 5000 iterations through randomly-sampled points using 2σ internal uncertainties. The ice surface lowering rates were calculated for each submarine valley facing region of Skarvsnes and Skallen, which protrude from the ice sheet as peninsulas. Because Telen is surrounded by Skallen and Telen glaciers and is located in the upper (terrestrial) part of the Telen submarine valley unlike Skarvsnes and Skallen, the exposure

ages from Telen are excluded from the calculation. In addition, the apparently young exposure age of 18012709 from Skallen is also excluded for the calculation because it is possibility originated to deposition of a re-advance Skallen Glacier.

The ice surface lowering rate for the area along the Honnör submarine valley ranges from 0.16-0.29 m/yr (1σ; 68 %) and 0.13-0.47 m/yr (2σ; 95 %), and the median rate is 0.21 m/yr (Fig. 5-1a). The ice surface lowering rate for along the Telen submarine valley (southern side of Skarvsnes and Skallen) ranges from 0.08-0.19 m/yr (1σ; 68 %) and 0.06-0.45 m/yr (2σ; 95 %), and the median rate is 0.11 m/yr (Fig. 5-1b). The ice surface lowering rate for along the Telen submarine valley (southern side of Skarvsnes) ranges from 0.10-0.38 m/yr (1σ; 68 %) and 0.07-1.83 m/yr (2σ; 95 %), and the median rate is 0.16 m/yr (Fig. 5-1c). The oldest age for the northern part of Skarvsnes is 8.9 ka (400 m a.s.l. at 18010904), while the oldest age for the southern part is 10.4 ka (352 m a.s.l. at SV4-2, Yamane et al., 2011). These slight difference of oldest exposure ages and ice surface lowering rate show the slight difference in the timing and magnitude of the ice retreat on the southern and northern sides of Skarvsnes, the ice retreat in this area is thought to start along the Telen submarine valley, and then propagate to the both sides of the valley (Fig. 5-1a, b, and c). On the other hand, the ice retreat along the Honnör

submarine valley likely starts slightly later, but it was more intensive, probably due to close contact between the mountain flank and the ocean (Figs 1-2b and 2-1). Therefore, the author concludes that the EAIS started to thin and retreat at the almost same time along the southern Soya Coast during the Early Holocene (between 10 and 9 ka), but that propagation was locally variable.

Because the moraine material suggests a change in behavior of glaciers such as re-advance and/or stillstand, surface exposure age of moraine on northern Skallen (18012812) provides evidence for a small re-advance and/or stillstand of the glacier that terminated at ~5.4 ka. Thicker accumulation of glacial debris reaches up to sample 16010901 (~4.2 ka) across the lower flanks of Telen is consistent with this interpretation.

Very young exposure ages obtained at three sites in Skallen and Telen provides new insights on the regional re-advance and after the continuously retreat of Skallen Glacier. The exposure age of 18012709 (ca. 1.5 ka) at Skallen can be explained by a possible re-advance of Skallen Glacier during the Late Holocene. Maemoku et al. (2008) inferred a minor re-advance of the glacier based on geomorphological observations, including shell fragments observed in clayey glacial sediments at Lake Magoke-Ike. On the basis of the ^{14}C age of a shell fragment (ca. 3 ka BP) (Igarashi et al., 1995), the author

considers that the re-advance of Skallen Glacier occurred ca. 3 ka. Thus, the exposure age of 18012709 (ca. 1.5 ka) obtained from a site ~1 km north of Lake Magoike-Ike likely represents the timing of the retreat of Skallen Glacier after the re-advance event (Fig. 2-2). The two young exposure ages of erratic rocks (16011201 at 0.6 ka and 16011202 at 0.2 ka) from lateral moraines along Skallen Glacier at Telen are interpreted the continuously retreat of Skallen Glacier had finished at the 0.6 ka. Thus, a re-advance of Skallen Glacier is thought to have occurred over the present ice-sheet margin during the Late Holocene, probably from ca. 3.0 ka, and after continuously retreated 1.5 ka to 0.6 ka. In addition, judging from the exposure age of the northern moraine (5.4 ka), it is probable that Skallen Glacier would not re-advance to the northern moraine.

Empirical geological evidence of bedrock weathering can also be used to estimate ice-sheet thickness along the Soya Coast prior to retreat and thinning of the EAIS. As mentioned above, the author interprets the transition in bedrock weathering features at Skjegget (Fig. 4-1), indicating a change of the basal ice sheet condition from a warm- to cold-based. It is known that poor preservation of strongly weathered bedrock suggests an ice thickness greater than ~300 m (Bentley et al., 2010; Bromley et al., 2010). Thus, the highly weathered bedrock with older exposure ages in the upper of Skjegget provides

the first-order estimation for the limit on the former ice thickness that overlaid the summit of Skjegget less than ~300 m.

The interpretation of ice thickness during the LGM along the Soya Coast is consistent with results of numerical modeling studies (Sawagaki and Hirakawa, 2002a; Okuno et al., 2013). Sawagaki and Hirakawa (2002a) conducted a hydraulic numerical experiment to estimate the optimum thickness and shape of an ice sheet, which is thought to produce the arrangement of streamlined bedforms by subglacial meltwater. Those authors found that the subglacial meltwater simulated by an ice sheet with a thickness of ~400 m tilted to the west is consistent with the arrangement of streamlined bedforms observed at Skarvsnes. On the other hand, Okuno and Miura (2013) performed relative-sea-level calculations for the Soya Coast and other sites along Antarctic coastal regions by using GIA modeling with different ice thickness, ice distribution and lithospheric thickness parameters. Regardless of lithospheric thickness parameters, those authors found that geological constrain of paleo sea-level (Miura et al., 1998a) could not be explained unless an ice sheet with a few hundred meters thick had melted along the Soya Coast since the LGM. Therefore, the author's estimates of ice thickness during the LGM from geological features from Skjegget (at least 400 m but no more than overlaid ~300

m at Skjegget) is consistent with the results of numerical models.

5.1.2 Interpretation of lake sediments, the history of lake system, and reconsidered of the previous report of RSL

The lithofacies of newly obtained Lake sediment cores show the lowermost unit composed of relatively coarse-grained sediment and overlain of these by the relatively soft, fine-grained freshwater lake/marine sediments. The matrix-supported silt beds with sand fractions and gravel recognized at the lowermost part of the sediment cores are interpreted as glacial sediments. The clear transition from glacial sediments to freshwater lake/marine sediments most likely reflects the process of the lake evolution and history after the retreat of the ice sheet. Unlike the other lake sediments, the sedimentary facies at the bottom of the Lake Namazu-Ike (NZ1i) are composed of less matrix, slightly rounded gravel, and contain microbial mat. In addition, the bottom of Lake Namazu-Ike (NZ1i) shows apparently younger ^{14}C age (2053 and 1154 cal. yr BP), which are not different from the surface and the lowest microbial mat layers. The apparently young ^{14}C age and sedimentary facies of the lowermost part of the core likely suggest that the unconsolidated gravel and microbial mat layer is turbidite origin intruded from the sharp

cliff of the lakeside. Except for Lake Namazu-Ike, the ^{14}C ages of the lower part of lake sediment cores are consistent with the exposure ages from the Skarvsnes, which confirm that the abrupt thinning and retreat of the EAIS occurred Early to Mid-Holocene (between 10 and 9 ka to 5.4 ka) along the southern Soya Coast (Fig. 5-2).

The initiation of retreat of the EAIS along the Soya Coast has previously been investigated on the basis of marine fossils and ^{14}C dating of lake sediments from Skarvsnes and Skallen (Miura et al., 1998a, c; Takano et al., 2012; Verleyen et al., 2017). At Skarvsnes, the oldest ^{14}C age of a marine fossil (a polychaete tube) in a raised beach is 8860 yr BP (Miura et al., 1998c), and the oldest bulk ^{14}C age of lake sediments from Lake Kobachi-Ike is 7650 yr BP (Verleyen et al., 2017) (Fig. 2-1, 5-3). At Skallen, the oldest ^{14}C age of a shell fragment (*Laternula elliptica*) in a raised beach is 7810 yr BP (Miura et al., 1998c) (Fig. 3). These ^{14}C ages suggest that Skarvsnes and Skallen became ice free during the period between 10 and 9 ka to 5.4 ka, which is consistent with the author's geomorphological observations, exposure ages, and ^{14}C ages in this study.

The RSL change along the Soya Coast has previously been investigated on the basis of the ^{14}C ages of fossil shells (*Laternula elliptica*) in raised beach, and lake sediment transition age of flesh to the marine environment with sill height (outflowing

point of the lake) (Miura et al., 1998a, c; Takano et al., 2012; Verleyen et al., 2017) (Fig. 5-3). Verleyen et al. (2017) reported a minimum RSL of 32.7 m a.s.l. which is about 10 m higher than previously published evidence in Skarvsnes (Hayashi and Yoshida. 1994; Miura et al., 1998a) (Fig. 5-3). Because the GIA model predictions have been unable to predict the rapid fall of the RSL (uplift rate of 16.2 mm/yr) at Skarvsnes (Whitehouse et al., 2012; Argus et al., 2014), Verleyen et al. (2017) interpreted that the high RSL is caused by a reactivation of a local fault. However, there are at least three issues uncertain: (i) the marine fossil reported from 32.7 m a.s.l., (ii) the transition of marine to lacustrine of Lake Kobachi-Ike, and (iii) neotectonic processes. The author claim they are needed to be reconsidered regarding the RSL estimations along the Soya Coast.

Firstly, no clear evidence is represented that the fossil shell at 32.7 m a.s.l. is in situ. Verleyen et al. (2017) reported ^{14}C age of a fossil shell preserved in a raised beach in the upper sill of Lake Kobachi-Ike (28 m a.s.l.). However, there is no description of the fossil in growth position in raised beach, suggesting that the fossil could be transported to the lake by a storm or by a bird, such as snow petrels. The distribution of raised beach sediments has been reported up to around 20 m a.s.l. (Hayashi and Yoshida, 1994; Miura et al., 1998a), which about 10 m lower than the fossil shell. Thus, the author

suggests that a careful consideration to constrain the RSL change not only based on the single ^{14}C age.

Secondly, the analysis of sediment core from Lake Kobachi-Ike seems difficult to simply interpret the change in depositional environment from marine to fresh water. Kimura et al. (2010) had reported a modern profile of the salinity of the Lake Kobachi-Ike, showing 0.8% above 2 m depth and 1.6–1.7% below 3 m depth (Fig. 5-4). Considering the salinity of about half of the seawater in the Lake Kobachi-Ike, the input freshwater after the lake isolation was not enough to flush the trapped marine water. This causes marine diatoms to be produced throughout the sediment cores in the Lake Kobachi-Ike, making it difficult to know the change in depositional environment from marine to the freshwater. Verlyen et al. (2017) considered the decrease in magnetic susceptibility and the start of the dominance by brackish diatoms at 93 cm depth of around 2.5 ka as a sign of separation from the ocean at the Lake Kobachi-Ike (Fig. 5-5). This timing is consistent with the timing of coincided with the cyanobacteria indicator of *myxoxanthophyll* (Verlyen et al., 2017). However, taking into account the present geographical setting of the Lake Kobachi-Ike (little freshwater inflow and little replacement of the trapped marine water), parameters of diatom assemblage with fossil

pigments and changes in the magnetic susceptibility not only indicate the timing of isolation from the ocean but also highly dependent on changes in snowfall and inflow of fresh water from the catchment. Therefore, the author argues that accurately estimate the marine to freshwater boundaries (i.e. timing of RSL fall) from the sediment core of Lake Kobachi-Ike is difficult.

Thirdly, the topographic change associated with local fault in Skarvsnes is not confirmed in this study. The fault trace passes through the Kizahashi Beach in Skarvsnes was described by Ishikawa et al. (1977) based on the description of geological structure. This fault is thought to have occurred in relation to deformation during the late Precambrian to Paleozoic of Lützow-Holm complex (Ishikawa et al. 1976). Based on this geological background, Verleyen et al. (2017) concluded the abrupt Holocene RSL change was thought to be caused by the re-activation of this fault (Fig. 5-6a). If the fault was moved after the ice sheet retreat, the fault cliff should appear in the topography as evidence of its activity because more than ca. 10 meters of offset is needed to produce the abrupt Holocene RSL change in Skarvsnes. However, no-fault is identified not only on the Kizahashi Beach but also the other area in Skarvsnes based on newly generated SfM-DSM analysis (Fig. 5-6b, c). Thus, the author concludes that no-fault movement could

have occurred in the Holocene.

In order to obtain new information on the high RSL period, the author investigated the raised beach distributed around Lake Oyako-Ike. The upper limit of height of the raised beach surrounding the Lake Oyako-Ike was ca. 16 m a.s.l. which shows the lower limit of RSL (Fig. 3-1). This height of the upper sea level limit is consistent with that at the Kizahashi Beach (Miura et al., 1998a). These facts indicate the lower limit of maximum RSL after ice-sheet retreat. Although there is no geomorphological evidence that the RSL was higher than ca. 16 m a.s.l., it is possible that the sediments were not preserved, and the upper limit of RSL cannot be specified.

Based on the above geomorphological interpretation and sediment core characteristics corrected from Lake Oyako-Ike, the geomorphic development around Lake Oyako-Ike is discussed. During the LGM, all of Skarvsnes, including those around Lake Oyako-Ike, were covered with thick ice (Fig. 5-7a). Glacial sediment was deposit at the bottom of the U-shaped valley connecting Lake Oyako-Ike and Osen (OY1). From ca. 8.5 to 8.0 ka, the ice sheets around Lake Oyako-Ike had started to melt. However, based on SED, the ice sheet would have melted from the Torinosu-Cove side of southern Skarvsnes and still remained on the Osen side (Fig. 5-7b). OY2 may have formed in a

relatively short period of time (for about 500 years) due to the abundant supply of debris from the nearby ice sheet. During this period, relatively large mass of ice like a valley glacier around the strait of Torinosu Cove and Osen certainly have still exist. The RSL is thought to be a peak at the beginning of the rapid ice sheet melting at Skarvsnes, and the RSL may have reached the sill height of Lake Kobachi-Ike 28 m a.s.l. at this time. The lack of geomorphological evidence showing the RSL of 28 m a.s.l. may have been caused by this glaciomarine environment of OY2. After ca. 8 ka, the ice sheet surrounding the Osen had melted and the environment gradually became open marine like a fjord. Marine organisms were thrived by about 3 ka (OY3) and the raised beach was formed surrounding the Lake Oyako-Ike (Fig. 5-7c). Because the RSL was further decreased, no debris is thought to be supplied from icebergs, and then formed homogeneous silty sediment (OY4) (Fig. 5-7d). Finally, the strait connecting Torinosu-Cove and Osen was cut off as the RSL lowered, and formed a freshwater Lake Oyako-Ike on ca. 1 ka (Takano et al., 2012) on the saddle of a U-shaped valley (OY5) (Fig. 5-7e).

5.2 Timing and magnitude of deglaciation since the LGM in the Indian Ocean sector of the EAIS

The geomorphological observation, including the surface exposure ages, lithology and ^{14}C ages of lake sediment indicate that the ice sheet completely covered the highest peak of Skarvsnes (at least 400 m of ice thickness but no more than overlaid ~300 m at summit of Skjegget) and retreated by at least 10 km during the relatively short interval from the Early to Mid-Holocene (between 10 and 9 ka to 5.4 ka) along the southern Soya Coast. The rate of thinning at Skjegget (Honnör submarine valley) is estimated to be 0.21 m/yr, which is similar to the other "abrupt thinning" reported at other locations across Antarctica, such as Western Weddle Sea (ca. 1.5 kyr to thin 250 m - i.e. <0.2 m/yr) (Johnson et al., 2019), in the heart of the inner Weddell Sea embayment (ca. 1 kyr to thin 200 m - i.e. 0.2 m/yr) (Hein et al., 2016), and western Marie Byrd Land (ca. 0.9 kyr to thin 330 m - i.e. <0.4 m/yr) (Stone et al., 2003). Such abrupt thinning and retreat of the EAIS have been reported from other parts of the Indian Ocean sector of East Antarctica (White and Fink, 2014). White and Fink (2014) reported exposure ages from erratic rock and bedrock samples from Condon Hills, along the lower part of the Rayner Glacier, in the coastal area of Enderby Land (Fig. 1-2a). Those authors determined exposure ages of erratic rocks in the upper (560 m a.s.l.) and lower (240 m a.s.l.) parts of

Condon Hills of ca. 9 ka and ca. 6 ka, respectively, indicating that ice-sheet thinning of >300 m and retreat of >10 km occurred during 9–6 ka at Condon Hills.

The thickness of the EAIS that overlaid Condon Hills can also be estimated using geomorphological features. A clear transition in the weathering state of bedrock has been observed within the elevation range of 300–450 m a.s.l. at Condon Hills (White and Fink, 2014). The bedrock above the transition is deeply weathered, whereas that in the lower part of the terrain is relatively unweathered, showing smooth surfaces and striations. In addition, the exposure ages of bedrock in the upper (560 m a.s.l.) and lower (240 m a.s.l.) parts are ca. 103 ka and ca. 26 ka, respectively, and are older than those of adjacent erratic rocks. These geomorphological features and older exposure ages of the bedrock at Condon Hills are similar to those observed at Skarvsnes, which the author explain in terms of a transition in subglacial conditions from a warm- to cold-based ice sheet. As ice-sheet thickness controls subglacial conditions (Bentley et al., 2010; Bromley et al., 2010), the thickness of the EAIS that overlaid Condon Hills during the LGM is considered not to have exceeded several hundred meters. Zwartz and Stone (1997) interpreted the LGM ice-sheet thickness at Mt. Riiser-Larsen (Fig. 1-2a), near Condon Hills, to have been less than 500 m, as no erratic rocks or striated bedrock are found above 500 m a.s.l.

there. These SED results and geomorphological features of bedrock from Enderby Land are very similar to present study observations for the Soya Coast in Dronning Maud Land (Fig. 1-2a). Combining the previous results with new data, the author infers that abrupt deglaciation after the LGM occurred essentially simultaneously along the entire coastal area of Dronning Maud Land and Enderby Land during the Early to Mid-Holocene.

In contrast to the coastal areas of Dronning Maud Land and Enderby Land, a lower magnitude of ice-sheet thinning in the interior of the EAIS has been inferred from exposure ages and geomorphologic evidence from nunataks in the Sør Rondane Mountains (Moriwaki et al., 1991, 1992; Suganuma et al., 2014) and the Wohlthat Massiv (Altmaier et al., 2010), Dronning Maud Land, East Antarctica. Although the marked ice-sheet thinning since the LGM has been reported in the major ice drainage system such as Lambert Glacier (White et al., 2011) and Rayner Glacier (White and Fink, 2014), the ice-sheet thinning is generally less intensive in the other part of the EAIS interior. Therefore, marked thinning and retreat of the EAIS since the LGM appears to have occurred only in the coastal area and the major ice drainage system in the Indian Ocean sector of East Antarctica.

Detailed reconstructions of the history of the EAIS will contribute to interpret the local crustal deformation observed by the GNSS and calibrate the current GIA models. Ohzono et al. (2006) reported an upward displacement rate of approximately 1 mm/year for 8 years since 1998 at Skarvsnes based on the GNSS observation. Although the effect of the significant snowfall in Dronning Maud Land, observed by the satellite gravity mission in recent years (e.g. Velicogna et al., 2020), is needed to be considered, detailed reconstruction of the retreat history of the relatively thick EAIS that overlaid the southern Soya Coast since the Early to Mid-Holocene, revealed by this study, allows us to compare the GNSS data and GIA models in future studies.

5.3 Possible mechanism and drivers of the abrupt deglaciation of the EAIS since the LGM

In order to identify the mechanisms and drivers of the abrupt thinning and retreat of the EAIS along the southern Soya Coast during Early to Mid-Holocene (between 10 and 9 ka to 5.4 ka), the scale and potentially non-linear (abrupt) nature of the response of the AIS to global climatic change must be considered. On the basis of ice-core $\delta^{18}O$ records (Dome Fuji Ice Core Project Members, 2017), no clear signal of climate change,

such as atmospheric warming, has been identified over this time interval (Fig. 5-8). Therefore, changes in atmospheric temperature and/or related snow accumulation rates are not considered as potential drivers for the abrupt thinning and retreat, meaning that an alternative explanation of the melting event is required.

A key consideration for explaining the abrupt deglaciation along the southern Soya Coast is the geographical setting, including the locations of currently ice-free areas (Skarvsnes, Skallen, and Telen) and the bathymetry of the adjacent areas. Deep submarine valleys incise from the continental shelf to the present ice-sheet margin into Lützow-Holm Bay (Moriwaki and Yoshida, 2002) (Fig. 1-2b). Skarvsnes and Skallen protrude from the continental ice sheet and face a branch (Telen submarine valley and Honnör submarine valley) of the deep submarine valleys (Fig. 1-1a).

On the basis of marine geological records, Igarashi et al. (2001) suggested that mCDW intruded and the intermittently intensified into the bay via submarine valleys during the Holocene. These valleys are thought to have been formed through selective erosion, controlled by geological structure, by past ice streams (Moriwaki and Yoshida, 1983), including a large outlet glacier that flowed NW–SE along the Telen submarine valley. Given this geographical configuration, the author considers that the ice sheet along

these valleys had been affected by basal melting and the rapidly retreat of the grounding-line due to mCDW intrusion into submarine valleys. Thus, the process of marine ice-sheet instability and ocean-driven melting is most likely caused the abrupt thinning and retreat of the EAIS along the southern Soya Coast between 10 and 9 ka to 5.4 ka.

In order to attempt to understand the possible mechanisms of the abrupt thinning and retreat of the EAIS along the southern Soya Coast since the LGM, changes in 2D shapes of the past ice-sheet are estimated based on the modern surface profile of Skallen Glacier (Fig. 5-9). The Skallen Glacier is relatively large among the outlet glaciers along the Soya Coast, flowing to the Telen submarine valley, and its grounding line is thought to be a few hundred meters below sea level. Thus, the modern profile of Skallen Glacier can be roughly used for estimating the 2D shapes of the glacier, which extended to Lützow-Holm Bay during the LGM. Fig. 5-9 shows horizontal cross-sections of the northern and southern sides of Skarvsnes and the modern profile of Skallen Glacier with exposure ages. This figure shows that similar exposure ages are found from the almost same altitude in the northern part of Skarvsnes, regardless of the distance from the current ice sheet margin. On the other hand, several samples with relatively older exposure ages are found near the present-day ice sheet margin in the southern part of Skarvsnes. This

distribution of the exposure ages and its slight discrepancy between the northern and southern side of Skarvsnes cannot be explained by a simple horizontal retreat of the glacier (Fig. 5-9).

The slight discrepancy in the timing of the initiation of the ice-sheet retreat between the northern and southern sides of Skarvsnes can be explained by the geographical configuration of this area. The Telen submarine valley, southern side of Skarvsnes, is a large submarine valley with more than 1000 m deep, while the Honnör submarine valley is slightly shallower and smaller (Fig. 1-1b). This suggests that the Telen submarine valley is potentially more susceptible to mCDW intrusion, which may cause earlier deglaciation in the southern side of Skarvsnes. On the other hand, the Skjegget, northern part of Skarvsnes, is directly facing to the Honnör submarine valley, which may have been more sensitive to the mCDW intrusion and to the ocean–ice-sheet interactions than the southern part of Skarvsnes. Therefore, the initiation of the ice sheet thinning of the northern part of Skarvsnes was slightly later, but the more abrupt thinning was thought to have occurred (Fig. 5-8). In addition, in the southern side of Skarvsnes, there are submarine valleys with down to ca. 200 m deep, which is thought to be covered by a small valley glacier during the LGM (Fig. 5-10). The relatively older exposure ages in the

southern part of Skarvsnes, obtained despite its proximity to the present-day ice sheet margin, may be attributed to this valley topography.

The position of the grounding line during the LGM is also estimated in this study. Based on the estimation of the range of maximum ice-sheet thickness by the bedrock weathering features and inherited exposure age (Fig. 4-1), ridges of submarine valleys exist in the extent of ice sheet expansion considered from the 2D shape of the Skallen Glacier. This suggests the grounding line during the LGM is thought to be located on the ridge of the submarine valley (Figs. 5-11 and 5-12). Because marine ice-sheet instability requires a positive feedback process due to reverse bed slopes (e.g. Schoof et al., 2007), this geographical configuration might be a key for the abrupt thinning and retreat of the EAIS in the southern Soya Coast. Inflowing the mCDW drives enhanced basal melting and perturbation in the vicinity of the grounding line located on a ridge of the submarine valley, resulting in an inland retreat of the grounding line. The grounding line is then migrated on slopes downward inland, i.e. an unstable position, which causes the abrupt thinning and retreat of the Skarvsnes and Skallen. On the other hand, Telen is located upstream of the submarine valley and is flanked by glaciers, unlike the other two ice-free areas of Skarvsnes and Skallen (Fig. 1-1b). The author interprets these differences in

geographical configuration in terms of marine ice-sheet instability effect have been relatively minor at Telen, thus the ice-sheet thinning was relatively slow in this area (Fig. 4-5d). Overall, present study suggests that the thinning and retreat of the EAIS in the southern part of the Soya Coast have been greatly influenced by the marine ice-sheet instability and ocean-driven melting.

Fig 5-13 illustrates a schematic view of the processes of the hundreds of meters of thinning and ca. 30 km of retreat of the EAIS along the Soya Coast (Figs. 5-8 and 5-13). The inferred history of the ice-sheet retreat is as follows. The EAIS covered the entire southern Soya Coast during the LGM. The ice sheet thinning and retreat had started Early-Holocene (around 10 ka), with flow direction changing as a result of bedrock topographic control. The thinning and retreat of the EAIS in this area is considered to have been marine ice-sheet instability caused by the intensified intruding of the mCDW via deep submarine valleys. This suggests that the Telen submarine valley is potentially more susceptible to mCDW intrusion, which may cause earlier deglaciation in the southern side of Skarvsnes. Around 8–7 ka, the lakes located southern side of Skarvsnes were established with the retreat of the ice sheet. The small re-advance and/or stillstand of Skallen Glacier likely suggest ceasing or weakening of the mCDW intrusion by ~5.4 ka.

In other parts of Antarctica, including Condon Hills, hundreds of meters of ice-sheet thinning over a few thousand years in the Holocene have been reported (Johnson et al., 2014, 2019; Jones et al., 2015; Hein et al., 2016; Spector et al., 2017). A common feature in these studies is that areas with such abrupt ice-sheet thinning are face the fast-flowing outlet glaciers. Small et al. (2019) reported high paleo ice-sheet thinning rates are thought to coincide with the modern ice mass loss region in West Antarctica. Etourneau et al. (2019) revealed a sharp increase in ocean temperature from ~8200 to 7000 years BP is accompanied by a continuous and slow ocean warming of +0.3 ˚C throughout the Mid to Late-Holocene in the eastern Antarctic Peninsula. In addition, a rapid deglaciation of the Amundsen sea sector due to the intensified CDW upwelling from at least 10,400 years ago until 7,500 years ago is also suggested by chemical compositions such as the magnesium/calcium (Mg/Ca) ratio and $\delta^{13}C$ ratio of foraminifera shells and benthic foraminifera assemblages of marine sediments (Hillenbrand et al., 2017). These timing of mCDW inflow is almost consistent with the onset of the abrupt retreat of the southern Soya Coast. Since the mCDW upwelling to the continental shelf is considered to be ACC-related, the mCDW intensification observed in West Antarctica may have been synchronized in the western Indian Ocean sector of East Antarctica, including Soya Coast,

during the Early to Mid-Holocene. This emphasizes the importance of reconstructing paleo ice-sheet changes based on geological and geomorphological study not only in West Antarctica but also in East Antarctica to predict potential ice sheet melting areas associated with ocean–ice-sheet interactions in the future.

Conversely, deglaciation since the LGM as inferred from inland nunataks was not significant in Dronning Maud Land (Moriwaki et al., 1991, 1992; Altmaier et al., 2010; Suganuma et al., 2014), suggesting that the ice-sheet thinning in coastal areas did not propagate into the interior of the EAIS. Therefore, the author hypothesizes that the difference in ice-sheet thinning since the LGM between coastal areas and the EAIS interior can be explained by different mechanisms of ice-mass change. The loss of ice mass in coastal areas is considered to have been caused predominantly by ice dynamics (fast response) responding to ocean–ice-sheet interactions. In contrast, the change in ice mass in the EAIS interior was likely to have been controlled by water supply from the Southern Ocean (slow response) (Suganuma et al., 2014; Yamane et al., 2015). This hypothesis emphasizes the promotion of ice-sheet thinning at the regional scale by mCDW, extending along the coastal area of the western Indian Ocean sector, but with propagation of the ice-mass loss being restricted by the geographical setting.

The source of Meltwater Pulse 1A (MWP-1A) has been suspected to have in part originated in East Antarctica (Weber et al., 2014; Small et al., 2019). New exposure ages indicate that the timing of ice-sheet retreat most likely post-dated MWP-1A, implying a minimal contribution by ice-melting along the Soya Coast to MWP-1A (Fig. 5-8d). These results are rather consistent with recent studies that suggest the AIS was destabilized by retreating the grounding line due to sea-level rise induced by melting of the northern hemisphere ice-sheet (Mackintosh et al., 2011; Gomez et al., 2020). However, the extent and thickness of the EAIS in Lützow-Holm Bay during the LGM have not yet been established. Therefore, further studies, especially those based on marine records, are needed to accurately estimate the contribution of ice mass loss around Lützow-Holm Bay to sea-level rise after the LGM.

5.4 Future research priorities

The present study suggests that understanding of ocean–ice-sheet interactions to explain ice sheet behavior is important not only for West Antarctica but also for the Indian Ocean sector of East Antarctica. The geographic configuration of Lützow-Holm Bay is highly suitable for investigating these interactions. Despite elucidating the detailed

deglaciation history along the southern Soya Coast in this study, the LGM grounding zone in Lützow-Holm Bay and the detailed deglaciation history of marine ice-sheet associated with the inflow of mCDW are unclear. For a further understanding of the extent of ice-sheet expansion and the mechanism of the EAIS variability, detailed geomorphological investigations, including surface exposure dating and lake sediment analysis, should be carried out throughout the Soya Coast, especially northern Soya Coast where may have remained ice-free during the LGM. In addition, detailed bathymetry and marine sediment analysis in the Lützow-Holm Bay will contribute to a better understanding of the long-term response to ocean-driven ice-sheet melting. In particular, Be isotope analysis together with microfossil analysis of marine sediments would help us to constrain the progress of marine ice-sheet melting (the process from the subglacial to the ice shelf to the open marine) associated with the mCDW intrusion during the Holocene (e.g. White et al., 2019). Moreover, numerical modeling studies various range and variety of forcings should be applied to test the mechanisms (the forcing of warm water and bathymetry) on the ice-sheet retreat that caused grounding-line migration, together with a comparison of model results with field observations relating to past ice extent (e.g. Mackintosh et al., 2011; Jones et al., 2015; Whitehouse et al., 2017). As described above, the combination

of high-precision spatial deglaciation history in Lützow-Holm Bay and numerical modeling studies will lead to assess the critical for understanding ice sheet mass loss over this century and beyond around the Indian Ocean sector where not much is known.

6. Conclusion

The present study reveals the ice-retreat history of the southern Soya Coast, Lützow-Holm Bay, East Antarctica, based on field-based geomorphological observations, surface exposure ages, and lake sediment analysis, including high precision ^{14}C dating and physical property measurements. The major findings of this study are summarized as follows.

- The East Antarctic Ice Sheet (EAIS) during the Last Glacial Maximum extended at least 10 km farther than the present ice margin and had an ice thickness of at least 400 m at Skarvsnes, southern Soya Coast.
- Surface exposure ages and lower part of ^{14}C ages from lake sediments from the southern Soya Coast indicate that abrupt thinning and retreat of the ice sheet occurred during the Early to Mid-Holocene (between 10 and 9 ka to 5.4 ka).
- The ice sheet that overlaid the southern Soya Coast retreated while changing flow direction as controlled by bedrock topography.
- The abrupt fall in relative sea-level previously reported in Skarvsnes were not associated with the neotectonic processes.

- Differences in exposure ages of bedrock-erratic pairs from the same location suggest inheritance in the ages of the bedrock acquired during ice-free periods prior to the last deglaciation. The inherited ages and geomorphological features indicate that the subglacial condition of the ice sheet that overlaid this area was nonerosive cold-based ice and/or warm-based ice.
- Evidence from weathering features and inherited age of bedrock at Skjegget (400 m a.s.l.) at Skarvsnes provides the first-order estimation for the limit on the former ice sheet thickness that overlaid the summit of Skjegget less than ~300 m.
- The abrupt ice-sheet thinning and retreat identified along the southern Soya Coast is most likely synchronously occurred with a similar magnitude in the other Antarctic ice-free areas characterized by fast-flowing outlet glaciers.
- The mechanism of the abrupt thinning and retreat of the EAIS in this area is considered to have been marine ice-sheet instability caused by the intrusion of modified Circumpolar Deep Water via deep submarine valleys.

References

Altmaier, M., Herpers, U., Delisle, G., Merchel, S., Ott, U., 2010. Glaciation history of Queen Maud Land (Antarctica) reconstructed from in-situ produced cosmo- genic ^{10}Be, ^{26}Al and ^{21}Ne. Polar Sci. 4, 42−61.

Argus, D.F., Peltier, W.R., Drummond, R., Moore, A.W., 2014. The Antarctica component of postglacial rebound model ICE-6G_C (VM5a) based on GPS positioning, exposure age dating of ice thicknesses, and relative sea level histories. Geophys. J. Int. 198, 537−563.

Balco, G., Stone, J.O., Lifton, N., Dunai, T.J., 2008. A complete and easily accessible means of calculating surface exposure ages or erosion rates from ^{10}Be and ^{26}Al measurements. Quat. Geochronol. 3, 174−195.

Bentley, M.J., 2010. The Antarctic palaeo record and its role in improving predictions of future Antarctic Ice Sheet change. J. Quat. Sci. 25, 5−18.

Bentley, M. J., Fogwill, C. J., Le Brocq, A. M., Hubbard, A. L., Sugden, D. E., Dunai, T. J., S. P. Freeman., 2010. Deglacial history of the West Antarctic Ice Sheet in the Weddell Sea embayment: Constraints on past ice volume change, Geology 38, 411–414.

Bentley, M.J., Hein, A.S., Sugden, D.E., Whitehouse, P.L., Shanks, R., Xu, S., Freeman, S.P.H.T., 2017. Deglacial history of the Pensacola Mountains, Antarctica from glacial geomorphology and cosmogenic nuclide surface exposure dating. Quat. Sci. Rev. 158, 58−76.

Bierman, P.R., Caffee, M.W., Davis, P.T., Marsella, K., Pavich, M., Colgan, P., Mickelson, D., Larsen, J., 2002. Rates and timing of earth surface processes from in situ- produced cosmogenic Be-10, Beryllium. Mineral. Petrol. Geochem. 147−205.

Briggs, R.D., Pollard, D., Tarasov, L., 2014. A data-constrained large ensemble analysis of Antarctic evolution since the Eemian. Quat. Sci. Rev. 103, 91–115.

Bradley, S.L., Hindmarsh, R.C.A., Whitehouse, P.L., Bentley, M.J., King, M.A., 2015. Low post- glacial rebound rates in the Weddell Sea due to Late Holocene ice-sheet readvance. Earth Planet. Sci. Lett. 413, 79–89.

Broecker, W. (2010) The Great Ocean Conveyor: Discovering the Trigger for Abrupt Climate Change. Princeton University Press, Princeton, New Jersey.

Bromley, G. R. M., Hall, G., Stone, J., Conway, H., Todd, C., 2010. Late Cenozoic deposits at Reedy Glacier, Transantarctic Mountains implications for former thickness of the West Antarctic Ice Sheet, Quat. Sci. Rev. 29, 384–398.

Borchers, B., Marrero, S., Balco, G., Caffee, M., Goehring, B., Lifton,N., Nishiizumi, K., Phillips, F., Schaefer, J. and Stone, J., 2016. Geological calibration of spallation production rates in the CRONUS- Earth project. Quat. Geochronol. 31, 188−198.

Chmeleff, J., Blanckenburg, F., Kossert, K., Jakob, D., 2010. Determination of the 10Be half-life by multicollector ICP-MS and liquid scintillation counting. Nucl. Instrum. Methods in Phys. Res. B. 268, 192−199.

Depoorter, M., Bamber, J., Griggs, J., Lenaerts, J.T.M., Ligtenberg, S.R.M., van den Broeke, M.R., Moholdt, G., 2013. Calving fluxes and basal melt rates of Antarctic ice shelves. Nature 502, 89–92.

Dinniman, M.S., Klinck, J.M., Hofmann, E.E., 2012. Sensitivity of circumpolar deep water transport and ice shelf basal melt along the West Antarctic Peninsula to changes in the winds. Journal of Climate 25, 4799-4816.

Dinniman, M.S., Asay-Davis, X.S., Galton-Fenzi, B.K., Holland P.R., Jenkins A., Timmermann R., 2016. Modeling ice shelf/ocean interaction in Antarctica: A review. Oceanography 29, 144–153.

Domack, E.W., McClennen, C.E., 1996. Accumulation of glacial marine sediments in fjords of the Antarctic Peninsula and their use as late Holocene paleoenvironmental indicators. In: Ross, R.M., Hofmann, E.E., Quetin, L.B. (Eds.), Foundations for Ecological Research West of the Antarctic Peninsula. Antarctic Research Series, 70. American Geophysical Union, Washington, DC, 135–154

Dome Fuji Ice Core Project Members: Kawamura, K., Abe-Ouchi, A., Motoyama, H., Ageta, Y., Aoki, S., Azuma, N., Fujii, Y., Fujita, K., Fujita, S., Fukui, K., Furukawa, T., Furusaki, A., Goto-Azuma, K., Greve, R., Hirabayashi, M., Hondoh, T., Hori, A., Horikawa, S., Horiuchi, K., Igarashi, M., Iizuka, Y., Kameda, T., Kanda, H., Kohno, M., Kuramoto, T., Matsushi, Y., Miyahara, M., Miyake, T., Miyamoto, A., Nagashima, Y., Nakayama, Y., Nakazawa, T., Nakazawa, F., Nishio, F., Obinata, I., Ohgaito, R., Oka, A., Okuno, J., Okuyama, J., Oyabu, I., Parrenin, F., Pattyn, F., Saito, F., Saito, T., Saito, T., Sakurai, T., Sasa, K., Seddik, H., Shibata, Y., Shinbori, K., Suzuki, K., Suzuki, T., Takahashi, A., Takahashi, K., Takahashi, S., Takata, M., Tanaka, M., Uemura. R., Watanabe, G., Watanabe, O., Yamasaki, T., Yokoyama, K., Yoshimori, M. and Yoshimoto, T., 2017. State dependence of climatic instability over the past 720,000 years from Antarctic ice cores and climate modeling. Science Advances 3, 2, e1600446.

Dutton, A., A. E. Carlson, A. J. Long, G. A. Milne, P. U. Clark, R. DeConto, B. P. Horton, S. Rahmstorf and M. E. Raymo., 2015. Sea-level rise due to polar ice-sheet mass loss during past warm periods. Science, 349, aaa4019.

Golledge, N.R., Fogwill, C.J., Mackintosh, A.N. Buckley, K.M., 2012. Dynamics of the Last Glacial Maximum Antarctic ice-sheet and its response to ocean forcing. Proc. Natl Acad. Sci. USA 109, 16052–16056.

Golledge, N. R., Keller, E. D., Gomez, N., Naughten, K. A., Bernales, J., Trusel, L. D., Edwards, T. L., 2019. Global environmental consequences of twenty-first-century ice-sheet melt. Nature 566, 65–72.

Golledge, N. R., Kowalewski, D., Naish, T., Levy, R., Fogwill, C., Gasson, E., 2015. The multi-millennial Antarctic commitment to future sea-level rise. Nature 526, 421–425.

Gomez, N., Weber, M.E., Clark, P.U., Mitrovica, J.X., Han H.K., 2020. Antarctic ice dynamics amplified by Northern Hemisphere sea-level forcing. Nature 587**,** 600–604.

Gosse, J.C., Phillips, F.M., 2001. Terrestrial in situ cosmogenic nuclides: theory and application. Quat. Sci. Rev. 20, 1475–1560.

Hayashi, M., Yoshida, Y., 1994. Holocene raised beaches in the Lützow-Holm Bay region, East Antarctica. Memoir National Institute of Polar Research (special issue) 50, 49–84.

Hodgson, D.A., Noon, P.E., Vyverman, W., Bryant, C.L., Gore, D.B., Appleby, P., Gilmour, M., Verleyen, E., Sabbe, K., Jones, V.J., Ellis-Evans, J.C., Wood, P.B., 2001. Were the Larsemann Hills ice-free through the last glacial maximum? Antarct. Sci. 13, 440–454.

Hogg, A.G., Hua, Q., Blackwell, P.G., Niu, M., Buck, C.E., Guilderson, T.P., Heaton, T.J., Palmer, J.G., Reimer, P.J., Reimer, R.W., Turney, C.S.M., Zimmerman, S.R.H., 2013. SHCAL13 Southern hemisphere calibration, 0-50,000 years CAL BP. Radiocarbon 55, 1889–1903.

Igarashi, A., Numanami, H. Tsuchiya, Y., Harada, N., Fukuchi, M., Saitoh, T., 1995. Radiocarbon ages of molluscan shell fossils in raised beach deposits along the east coast of Lützow-Holm Bay, Antarctica, determined by accelerator mass-spectrometry. Proc. NIPR Symp. Polar Biol. 8, 154−162.

Igarashi, A., Numanami, H., Tsuchiya, Y., Fukuchi, M., 2001. Bathymetric distribution of fossil foraminifera within marine sediment cores from the eastern part of Lützow-Holm Bay, East Antarctica, and its paleoceanographic implications. Marine Micropaleontology 42, 125−162.

Ishikawa, T., 1976. Superimposed Folding of the Precambrian Metamorphic Rocks of the Lutzow-Holm Bay Region, East Antarctica. Mem. Nat. Inst. Pol. Res. Ser. C 9, 1−41.

Ishikawa, T., Yanai, K., Matsumoto, Y., Kizaki, K., Kojima, S., Tatsumi, T., Kikuchi, T. Yoshikawa, M., 1977. Geological map of Skarvsnes, Antarctica. Antarctic Geological Map Series, Sheet 6 and 7, National Institute of Polar Research, Tokyo, Japan.

Ivins, E. R., James, T. S., 2005. Antarctic glacial isostatic adjustment: a new assessment. Antarct. Sci. 17, 541–553.

Jacobs, S.S., Jenkins, A., Giulivi, C.F., Dutrieux, P., 2011. Stronger ocean circulation and increased melting under Pine Island Glacier ice shelf. Nat. Geosci. 4, 519−523.

Jenkins, A., Shoosmith, D., Dutrieux, P., Jacob, S., Kim, T.W., Lee, S.H., Ha, H.K., Stammerjohn, S., 2018. West Antarctic Ice Sheet retreat in the Amundsen Sea driven by decadal oceanic variability Nat. Geosci. 11, 733–738.

Johnson, G. C., 2008. Quantifying Antarctic Bottom Water and North Atlantic Deep Water volumes. J. Geophys. Res. 113, C05027.

Johnson, J.S., Bentley, M.J., Smith, J.A., Finkel, R.C., Rood, D.H., Gohl, K., Balco, G., Larter, R.D., Schaefer, J.M., 2014. Rapid thinning of pine Island Glacier in the early Holocene. Science 999–1001.

Johnson, J. S., Nichols, K. A., Goehring, B. M., Balco, G., Schaefer, J. M., 2019. Abrupt mid-Holocene ice loss in the western Weddell Sea Embayment of Antarctica, Earth Planet. Sci. Lett. 518, 127–135.

Joughin, I., Smith, B. E., Medley, B., 2014. Marine ice sheet collapse potentially under way for the Thwaites Glacier basin, West Antarctica. *Science* 344, 735–738.

Jones, R.S., Mackintosh, A.N., Norton, K.P., Golledge, N.R., Fogwill, C.J., Kubík, P.W., Christl, M., Greenwood, S.L., 2015. Rapid Holocene thinning of an East Antarctic outlet glacier driven by marine ice sheet instability. Nat. Commun. 6, 8910.

Jones, R. S., Norton, K.P., Mackintosh, A.N., Anderson, J.T.H., Kubik, P., Vockenhuber, C., Wittmann, H., Fink, D., Wilson, G.S., Golledge, N.R., McKay, R., 2017. Cosmogenic nuclides constrain surface fluctuations of an East Antarctic outlet glacier since the Pliocene. Earth Planet. Sci. Lett. 480, 75–86.

Jones, R.S., Whitehouse, P.L., Bentley, M.J., Small, D.P., Dalton, A.S., 2019. Impact of glacial isostatic adjustment on cosmogenic surface-exposure dating. Quat. Sci. Rev. 212, 206–212.

Lambeck, K., Rouby, H., Purcell, A., Sun, Y., Sambridge, M., 2014. Sea level and global ice volumes from the Last Glacial Maximum to the Holocene. Proc. Natl. Acad. Sci. 111, 15296−15303.

Kanamaru, T., Suganuma, Y., Oiwane, H., Miura, H., Miura, M., Okuno, J., Hayakawa, H., 2018: The weathering of granitic rocks in a hyper-arid and hypothermal environment: A case study from the Sør-Rondane Mountains, East Antarctica. Geomorphology 317, 62−74.

Kida, M., Kojima, T., Tanabe, Y., Hayashi, K., Kudoh, S., Maie, N., & Fujitake, N. 2019. Origin, distributions, and environmental significance of ubiquitous humic-like fluorophores in Antarctic lakes and streams. Water Research, 163, 114901.

Kimura, S., Ban, S., Imura, S., Kudoh, S., Matsuzaki, M., 2010. Limnological characteristics of vertical structure in the lakes of Syowa Oasis, East Antarctica. Polar Sci 3, 262−271.

Kohl, C. P., Nishiizumi, K., 1992. Chemical isolation of quartz for measurement of in-situ-produced cosmogenic nuclides. Geochim. Cosmochim. Acta. 56, 3583−3587.

Korschinek, G., Bergmaier, A., Faestermann, T., Gerstmann, U.C., Knie, K, Rugel, G., Wallner, A., Dillmann, I., Dollinger, G., Lierse von Gostomski, C., Kossert, K., Maiti, M., Poutivtsev, M. and Remmert, A. 2010. A new value for the half-life of 10Be by Heavy-Ion Elastic Recoil Detection and liquid scintillation counting. Nucl. Instrum. Methods in Phys. Res. B. 268, 187−191.

Lifton, N., Sato, T., Dunai, T.J., 2014. Scaling in situ cosmogenic nuclide production rates using analytical approximations to atmospheric cosmic-ray fluxes. Earth Planet. Sci. Lett. 386, 149−160.

Liu, Y., Moore, J.C., Cheng, X., Gladstone, R.M., Bassis, J.N., Liu, H., Wen, J., Hui, F., 2015. Ocean-driven thinning enhances iceberg calving and retreat of Antarctic ice shelves. Proc. Natl. Acad. Sci. USA 112, 3263–3268.

Locarnini, R. A., Mishonov, A. V., Antonov, J. I., Boyer, T. P., Garcia, H. E., Baranova, O. K., Zweng, M. M., Paver, C. R., Reagan, J. R., Johnson, D. R., Hamilton, M., Seidov, D., 2013. World Ocean Atlas 2013, Volume 1: Temperature. S. Levitus, Ed., A. Mishonov Technical Ed.; NOAA Atlas NESDIS 73, 40 pp. U.S. Gov. Printing Office, Washington, D.C.

Mackintosh, A., White, D., Fink, D., Gore, D.B., Pickard, J., Fanning, P.C., 2007. Exposure ages from mountain dipsticks in Mac.Robertson Land, East Antarctica, indicate little change in ice-sheet thickness since the Last Glacial Maximum. Geology 35, 551−554.

Mackintosh, A., Golledge, N., Domack, E., Dunbar, R., Leventer, A., White, D., Pollard, D., DeConto, R., Fink, D., Zwartz, D., Gore, D., Lavoie, C., 2011. Retreat of the East Antarctic ice sheet during the last glacial termination. Nat. Geosci. 4, 195−202.

Mackintosh, A., Verleyen, E., O'Brien, P.E., White, D.A., Jones, R.S., McKay, R., Dunbar, R., Gore, D.B., Fink, D., Post, A.L., Miura, H., Leventer, A., Goodwin, I., Hodgson, D.A., Lilly, K., Crosta, X., Golledge, N.R., Wagner, B., Berg, S., van Ommen, T., Zwartz, D., Roberts, S.J., Vyverman, W., Masse, G., 2014. Retreat history of the east Antarctic ice sheet since the last glacial maximum. Quat. Sci. Rev. 100, 10−30.

Maemoku, H., Miura, H., Saigusa, S., Moriwaki, K., 1997. Stratigraphy of the Late Quaternary raised record of the late Pleistocene beach deposits in the northern part of Langhovde, Lutzow-Holmbay, East Antarctica. Proc. NIPR Symp. Antarct. Geosci. 10, 178−186.

Maemoku, H., Miura, H., Iwasaki, S., 2008. A possibility of glacial fluctuation in the East Antarctic Ice Sheet during mid Holocene deduced from the landforms and unconsolidated subsurface sediments. The 28th symposium on polar geosciences program and abstracts 107P.

Miura, H., Maemoku, H., Seto, K., Moriwaki, K., 1998a. Late Quaternary East Antarctic melting event in the Soya Coast region based on stratigraphy and oxygen isotopic ratio of fossil molluscs. Pol. Geosci. 11, 260−274.

Miura, H., Moriwaki, K., Maemoku, H., Hirakawa, K., 1998b. Fluctuations of the East Antarctic ice-sheet margin since the last glaciation from the stratigraphy of raised beach deposits along the Soya Coast. Annals of Glaciology 27, 297−301.

Miura, H., Maemoku, H., Igarashi, A., Moriwaki., K., 1998c. Late Quaternary raised beach deposits and radiocarbon dates of marine fossils around Lützow-Holm Bay. Special Map Series of National Institute of Polar Research 6, National Institute of Polar Research, Tokyo.

Miller, K.G., Schmelz, W.J., Browning, J.V., Kopp, R.E., Mountain, G.S., Wright, J.D., 2020. Ancient sea level as key to the future. Oceanography 33, 32–41.

Moriwaki, K., Hirakawa, K., Hayashi, M., Iwata, S., 1992. Late Cenozoic Glacial history in the Sør-Rondane Mountains, East Antarctica. In: Yoshida, Y., Kaminuma, K., Shiraishi, K. (Eds.), Recent Progress in Antarctic Earth Science. Terra Scientific Publishing Company, Tokyo pp. 661−667.

Moriwaki, K., Iwata, S., Matsuoka, N., Hasegawa, H., Hirakawa, K., 1991. Weathering stage of till and glacial history of the central Sør-Rondane Mountains. Proc. NIPR Symp. Antarct. Geosci. 5, 99−111.

Moriwaki, K., Iwata, S., Matsuoka, N., Hasegawa, H., Hirakawa, K., 1994. Weathering stage as a relative age of till in the central Sør-Rondane. Proc. NIPR Symp. Antarct. Geosci. 7, 156−161.

Moriwaki, K., Yoshida, Y., 1983. Submarine topography of Lutzow-Holm Bay, Antarctica. Mem.Natl. Inst. Polar Res., Spec. Issue 28, 247−258

Moriwaki, K., Yoshida, Y., 2002. Bathymetric chart of Lützow-Holmbukta (Lützow-Holm Bay). Special Map Series of National Institute of Polar Research 4b, National Institute of Polar Research, Tokyo.

Nakai, Y., Kano, T., Yoshikawa, S., Ishikawa, T., Yanai, K., 1979. Explanatatory text of geological map of Kjuka and Telen, Antarctica. Antarctic Geological Map Series, Sheet 8, National Institute of Polar Research, Tokyo, Japan.

Nakayama, Y., Menemenlis, D., Zhang, H., Schodlok, M., Rignot, E, 2018. Origin of Circumpolar Deep Water intruding onto the Amundsen and Bellingshausen Sea continental shelves. Nat. Commun. 9, 3403.

Nishiizumi, K., 2004. Preparation of ^{26}Al ams standards. Nucl. Instrum. Methods Phys. Res. Sect. B-Beam Interact. Mater. Atoms 223, 388−392.

Nishiizumi, K., Kohl, C.P., Arnold, J.R., Klein, J., Fink, D., Middleton, R., 1991. Cosmic ray produced ^{10}Be and ^{26}Al in Antarctic rocks: Exposure and erosion history. Earth Planet. Sci. Lett. 104, 440−454.

Nishiizumi, K., Imamura, M., Caffee, M.W., Southon, J.R., Finkel, R.C., McAninch, J., 2007. Absolute calibration of Be-10 AMS standards. Nucl. Instrum. Methods Phys. Res. Sect. B-Beam Interact. Mater. Atoms 258, 403−413.

Ohshima, K. I., Y. Fukamachi, G. D. Williams, S. Nihashi, F. Roquet, Y. Kitade, T. Tamura, D. Hirano, L. Herraiz- Borreguero, I. Field, M. Hindell, S. Aoki and M. Wakatsuchi., 2013. Antarctic Bottom Water production by intense sea- ice formation in the Cape Darnley Polynya. Nature Geosci., 6, 235–240

Ohzono, M., Tabei, T., Doi, K., Shibuya, K., Sagiya, T., 2006. Crustal movement of Antarctica and Syowa Station based on GPS measurements. Earth, Planets and Space 58, 795–804.

Okuno, J., Miura, H., 2013. Last deglacial relative sea level variations in Antarctica derived from glacial isostatic adjustment modelling. Geosci. Front. 4, 623−632.

Omori, T., Yamazaki, K., Itahashi, Y., Ozaki, H., Yoneda, M., 2017. Development of a simple automated graphitization system for radiocarbon dating at the University of Tokyo. The 14th International Conference on Accelerator Mass Spectrometry.

Osanai, Y., Toyoshima, T., Owada, M., Tsunogae, T., Hokada, T., Yoshimura, Y., Miyamoto, T., Motoyoshi, Y., Crowe, W.A., Harley, S.L., Kanao, M., Iwata, M., 2004. Geological map of Skallen, Antarctica. Antarctic Geological Map Series, Sheet 40, National Institute of Polar Research, Tokyo, Japan.

Orsi, A. H., Whitworth, T., Nowlin, W. D., 1995. On the meridional extent and fronts of the Antarctic Circumpolar Current. Deep-Sea Research Part I, 42, 641–673.

Parkinson, C. L., Cavalieri. D. J., 2012. Antarctic sea ice variability and trends, 1979–2010. The Cryosphere 6, 871-880.

Pavlis, N. K., Holmes, S. A., Kenyon, S. C. and Factor, J. K. 2012. The development and evaluation of the Earth Gravitational Model 2008 (EGM2008). *Journal of Geophysical Research* 117: B04406.

Paolo, F. S., H. A. Fricker., L. Padman., 2015. Volume loss from Antarctic ice shelves is accelerating. Science 348, 327−331.

Peltier, W. R., Argus, D. F., Drummond, R., 2016. Space geodesy constrains ice age terminal deglaciation: the global ICE-6G_C (VM5a) model, J. Geophys. Res. Solid Earth 120, 450–487

Pritchard, H.D., Ligtenberg, S.R.M., Fricker, H.A., Vaughan, D.G., Van den Broeke, M.R., Padman, L., 2012. Antarctic ice-sheet loss driven by basal melting of ice shelves. Nature 484, 502−505.

Reimer, P.J., Bard, E., Bayliss, A., Beck, J.W., Blackwell, P.G., Ramsey, C.B., Buck, C.E., Cheng, H., Edwards, R.L., Friedrich, M., Grootes, P.M., Guilderson, T.P., Haflidason, H., Hajdas, I., Hatte, C., Heaton, T.J., Hoffmann, D.L., Hogg, A.G., Hughen, K.A., Kaiser, K.F., Kromer, B., Manning, S.W., Niu, M., Reimer, R.W., Richards, D.A., Scott, E.M., Southon, J.R., Staff, R.A., Turney, C.S.M., van der Plicht, J., 2013. INTCAL13 and MARINE13 radiocarbon age calibration curves 0- 50,000 years cal BP. Radiocarbon 55, 1869−1887.

Rignot, E, Mouginot J, Scheuchl B., 2011. Ice flow of the Antarctic Ice Sheet. Science 333, 1427–1430.

Rignot, E., Jacobs, S., Mouginot, J., Scheuchl, B., 2013. Ice-shelf melting around Antarctica. Science 341, 266–270.

Rignot, E., J. Mouginot, and B. Scheuchl. 2017. MEaSUREs InSAR-Based Antarctica Ice Velocity Map, Version 2. Boulder, Colorado USA. NASA National Snow and Ice Data Center Distributed Active Archive Center.

Rignot, E., Mouginot, J., Scheuchl, B., van den Broeke, M., van Wessem, M.J., Morlighem, M., 2019. Four decades of Antarctic Ice Sheet mass balance from 1979–2017. Proc. Natl. Acad. Sci. USA 116, 1095–1103.

Sawagaki, T., Hirakawa, K., 1997. Erosion of Bedrock by subglacial meltwater, Soya Coast, East Antarctica. Geografiska. Annaler. A 79, 223−238.

Sawagaki, T., Hirakawa, K., 2002a. Hydrostatic investigationons on subglacial meltwater: implications for the formation of streamlined bedforms and subglacial lakes, East Antarctica, Pol. Geosci. 15, 123−147.

Sawagaki, T., Hirakawa, K., 2002b. Terrestrial evidence of melting of the Antarctic ice sheet during the last glacial period. Antarctica at the close of a millennium; proceedings of the 8th international symposium on Antarctic earth sciences (Gamble, John A., editor; et al.), Bulletin - Royal Society of New Zealand 35, 404−414.

Schoof, C., 2007. Ice sheet grounding line dynamics: Steady states, stability, and hysteresis. J. Geophysi. Res. 112, F03S28.

Shepherd, A., Ivins, E.R., Geruo, A., Barletta, V.R., Bentley, M.J., Bettadpur, S., Briggs, K.H., Bromwich, D.H., Forsberg, R., Galin, N., Horwath, M., Jacobs, S., Joughin, I., King, M.A., Lenaerts, J.T.M., Li, J.L., Ligtenberg, S.R.M., Luckman, A., Luthcke, S.B., McMillan, M., Meister, R., Milne, G., Mouginot, J., Muir, A., Nicolas, J.P., Paden, J., Payne, A.J., Pritchard, H., Rignot, E., Rott, H., Sorensen, L.S., Scambos, T.A., Scheuchl, B., Schrama, E.J.O., Smith, B., Sundal, A.V., van

Angelen, J.H., van de Berg, W.J., van den Broeke, M.R., Vaughan, D.G., Velicogna, I., Wahr, J., Whitehouse, P.L., Wingham, D.J., Yi, D.H., Young, D., Zwally, H.J., 2012. A reconciled estimate of ice-sheet mass balance. Science 338, 1183−1189.

Small, D., Bentley, M.J., Jones, R.S., Pittard, M.L., Whitehouse, P.L., 2019. Antarctic ice sheet palaeo-thinning rates from vertical transects of cosmogenic exposure ages. Quat. Sci. Rev. 206, 65−80.

Suganuma, Y., Miura, H., Okuno, J., 2012. A new sampling technique for surface exposure dating using a portable electric rock cutter. Antarctic Record (Nankyoku Shiryô) 2, 85−90.

Suganuma, Y., Miura, H., Zondervan, A., Okuno, J., 2014. East Antarctic deglaciation and the link to global cooling during the Quaternary: Evidence from glacial geomorphology and Be-10 surface exposure dating of the Sør Rondane Mountains, Dronning Maud Land. Quat. Sci. Rev. 97, 102−120.

Suganuma, Y., Katsuki, K. Kaneda, H., Kawama- ta, M., Tanabe, Y. and Shibata, D., 2019. Portable percussion piston corer, lake sediments, shallow marine sediment. Journal of the Geological Society of Japan, 125, 323−326.

Sugden, D.E., Balco, G., Cowdery, S.G., Stone, J.O., Sass, L.C., 2005. Selective glacial erosion and weathering zones in the coastal mountains of Marie Byrd Land, Antarctica. Geomorphology 67, 317−334.

Stone, J.O., Balco, G.A., Sugden, D.E., Caffee, M.W., Sass, L.C., Cowdery, S.G., Siddoway, C., 2003. Holocene deglaciation of Marie Byrd land, west Antarctica. Science 299, 99−102.

Stuiver., M., and Polach, H.A., 1977. Discussion: Reporting of ^{14}C data. Radiocarbon 19, 355−363.

Szeliski, R., 2010. Computer Vision: Algorithms and Applications. Springer-Verlag Editors, New York, USA.

Takada, M., Tani, A., Miura, H., Moriwaki, K., Nagatomo, T., 2003. ESR dating of fossil shells in the Lützow-Holm Bay region. East Antarctica. Quat. Sci. Rev. 22, 1323−1328.

Takano, Y., Tyler, J.J., Kojima, H., Yokoyama, Y., Tanabe, Y., Sato, T., Ogawa, N.O., Ohkouchi, N., Fukui, M., 2012. Holocene lake development and glacial-isostatic uplift at Lake Skallen and Lake Oyako, Lützow Holm Bay, East Antarctica, based on biogeochemical facies and molecular signatures. Applied Geochemistry 27, 2546−2559.

Thébault, E., Finlay C.C., Beggan, C.D., Alken, P., Aubert, J., Barrois, O., Bertrand, F., Bondar, T., Boness, A., Brocco, L., Canet, E., Chambodut, A., Chulliat, A., Coïsson, P., Civet, F., Du, A., Fournier, A., Fratter, I., Gillet, N., Hamilton, B.,

Hamoudi, M., Hulot, G., Jager, T., Korte, M., Kuang, W., Lalanne, X., Langlais, B., Léger J-M., Lesur, V., Lowes, F.J., Macmillan, S., Mandea, M., Manoj, C., Maus, S., Olsen, N., Petrov, V., Ridley, V., Rother, M., Sabaka, T. J., Saturnino, D., Schachtschneider, R., Sirol, O., Tangborn, A., Thomson, A., Tøffner-Clausen, L., Vigneron, P., Wardinski, I., Zvereva, T., 2015. International Geomagnetic Reference Field: the twelfth generation. Earth Planets Space 67−79.

Thoma, M., Jenkins, A., Holland, D., Jacobs, S., 2008. Modelling Circumpolar Deep Water intrusions on the Amundsen Sea continental shelf, Antarctica. Geophys. Res. Lett. 35, L18602.

Velicogna, I., Mohajerani, Y., A, G., Landerer, F., Mouginot, J., Noel, B., Rignot, E., Sutterley., T., Broeke, M. van den ., Wessem, M. van., Wiese, D., 2020. Continuity of ice sheet mass loss in Greenland and Antarctica from the GRACE and GRACE Follow-On missions. Geophys. Res. Lett. 47, e2020GL087291.

Verleyen, E., Tavernier, I., Hodgson, D.A., Whitehouse, P.L., Kudoh, S., Imura, S., Heirman, K., Bentley, M.J., Roberts, S.J., Batist, M.D., Sabbe, K., Vyverman, W., 2017. Ice sheet retreat and glacio-isostatic adjustment in Lützow-Holm Bay, East Antarctica. Quat. Sci. Rev. 169, 85−98.

Vernet, M., Geibert, W., Hoppema, M., Brown, P. J., Haas, C., Hellmer, H., Jokat, W., Jullion, L., Mazloff, M., Bakker, D. C. E., Brearley, J. A., Croot, P., Hattermann, T., Hauck, J., Hillenbrand, C.-D., Hoppe, C. J. M., Huhn, O., Koch, B. P., Lechtenfeld, O. J., Meredith, M. P., Naveira Garabato, A. C., Nöthig, E.-M., Peeken, I., Rutgers van der Loeff, M. M., Schmidtko, S., Schröder, M., Strass, V. H., Torres-Valdés, S., Verdy, A., 2019. The Weddell Gyre, Southern Ocean: Present knowledge and future challenges. Reviews of Geophysics 57, 623–708.

Watcham, E.P., Bentley, M.J., Hodgson, D.A., Roberts, S.J., Fretwell, P.T., Lloyd, J.M., Larter, R.D., Whitehouse, P.L., Leng, M.J., Monien, P., Moreton, S.G., 2011. A new Holocene relative sea-level curve for the South Shetland Islands, Antarctica. Quat. Sci. Rev. 30, 3152−3170.

Weber, M.E., Clark, P.U., Kuhn, G., Timmermann, A., Sprenk, D., Gladstone, R., Zhang, X., Lohmann, G., Menviel, L., Chikamoto, M.O., Friedrich, T., 2014. Millennial-scale variability in Antarctic ice-sheet discharge during the last deglaciation. Nature 510, 134.

Wessel, B., Huber, M., Wohlfart, C., Marschalk, U., Kosmann, D., Roth, A., 2018. Accuracy Assessment of the Global TanDEM-X Digital Elevation Model with GPS Data. ISPRS J. Photogramm. Rem. Sens. 139, 171–182.

White, D.A., Fink, D., Gore, D.B., 2011. Cosmogenic nuclide evidence for enhanced sensitivity of an East Antarctic ice stream to change during the last deglaciation. Geology 39, 23−26.

White, D.A., Fink, D., 2014. Late Quaternary glacial history constrains glacio-isostatic rebound in Enderby Land, East Antarctica. J. Geophys. Res. Earth Surface 119, 401−413.

White, D.A., Fink, D., Post, A.L., Simon, K., Galton-Fenzi, B., Foster, S., Fujioka, T., Jeromson, M.R., Blaxell, M., Yokoyama, Y., 2019. Beryllium isotope signatures of ice shelves and sub-ice shelf circulation. Earth Planet Sci. Lett. 505, 86–95.

Whitehouse, P. L., Bentley, M. J., Milne, G. A., King, M. A., Thomas, I. D., 2012. A new glacial isostatic adjustment model for Antarctica: calibrated and tested using observations of relative sea-level change and present-day uplift rates. Geophys J. Int. 190, 1464–1482.

Whitehouse, P. L., Bentley, M. J., Vieli, A., Jamieson, S. S. R., Hein, A. S., Sugden, D. E., 2017. Controls on Last Glacial Maximum ice extent in the Weddell Sea embayment, Antarctica, J. Geophys. Res. Earth Surf. 122, 371–397.

Whitehouse, P.L., Gomez, N., King, M.A., Wiens, D.A., 2019. Solid Earth change and the evolution of the Antarctic Ice Sheet. Nat. Comm. 10, 503.

Williams, G. D., Nicol, S., Aoki, S., Meijers, A. J. S., Bindoff, N. L., Iijima, Y., Marsland, S.J., Klocker, A., 2010. Surface oceanography of BROKE-West, along the Antarctic margin of the south-west Indian Ocean (30–80 degrees E). Deep-Sea Res. Pt. II 57, 738–757.

Yamane, M., Yokoyama, Y., Miura, H., Maemoku, H., Iwasaki, S., Matsuzaki, H., 2011. The last deglacial history of Lützow-Holm Bay, East Antarctica. J. Quat. Sci. 26, 3−6.

Yamane, M., Yokoyama, Y., Abe-Ouchi, A. Obrochta, S., Sito, F., Moriwaki, K., Matuzaki, H., 2015. Exposure age and ice-sheet model constraints on Pliocene East Antarctic ice sheet dynamics. Nat. Commun. 6, 7016.

Yoshida, Y., 1983. Physiography of the Prince Olav and the Prince Harald Coasts, East Antarctica. Memoirs of National Institute of Polar Research. Ser. C, Earth sciences 13, 1−83.

Zwartz, D., Stone, J., 1997. Cosmogenic isotope exposure dating at Mt Riiser Larsen. Implications for ice sheet history. The 17th Symposium on Antarctic Geosciences, Program and Abstracts, 1997 Tokyo, National institute for Polar Research 45, 1997 Tokyo, National institute for Polar Research, 45.

Table 1 Sample information for surface exposure dating.

Sample Name	Latitude (°S)[*a]	Longitude (°E)[*a]	Altitude (m)[*a]	Type	Thickness (cm)	Shielding factor [*b]	Sample size (m)
Skarvsnes							
16012401	69.4879	39.6509	237	Bedrock	2.5	0.987	-
16012403	69.4992	39.6836	139	Erratic	2.3	1.000	1.7×1.1×1.0
16012501	69.5085	39.7439	233	Erratic	2.6	0.982	1.1×0.8×0.8
16012402	69.4914	39.6617	66	Erratic	2.2	0.987	2.5×2.0×1.7
16012404	69.4995	39.7092	119	Erratic	2.7	0.996	0.8×0.7×0.5
16012503	69.4992	39.6836	139	Erratic	2.6	0.998	0.8×0.7×0.4
16012201	69.4658	39.7831	153	Erratic	2.5	0.999	1.3×1.0×1.0
16012301	69.4642	39.7464	122	Erratic	2.3	0.997	1.0×0.7×0.5
18010904	69.4303	39.5944	400	Erratic	5.0	0.994	cobble
18010905	69.4303	39.5944	400	Bedrock	2.5	0.998	-
18010911	69.4302	39.6041	296	Erratic	5.0	0.990	cobble
18010916	69.4288	39.6087	194	Erratic	4.5	0.978	cobble
18010924	69.4301	39.6196	105	Erratic	4.0	0.990	cobble
18010929	69.4298	39.6266	47	Erratic	4.5	0.994	cobble
17121703	69.4729	39.5796	214	Erratic	2.5	0.998	cobble
18010906	69.4300	39.5987	362	Erratic	4.0	0.996	cobble
18010914	69.4297	39.6061	244	Erratic	3.5	0.994	cobble
18010919	69.4296	39.6151	146	Erratic	3.0	0.989	cobble
17121801	69.4751	39.5879	97	Erratic	4.0	0.991	cobble
17121804	69.4755	39.5905	63	Erratic	4.0	0.976	cobble
Skallen							
15123101	60.6775	39.4431	115	Erratic	2.2	1.000	-
15123102	60.6775	39.4431	115	Bedrock	2.5	1.000	-
16010601	69.6464	39.4525	48	Erratic	2.4	1.000	-
17122702	69.6786	39.4765	140	Erratic	4.5	0.989	cobble
18012706	69.6775	39.4818	80	Erratic	4.0	0.995	cobble
18012805	69.6463	39.4416	92	Erratic	3.0	0.998	cobble
18012812	69.6483	39.4640	28	Erratic	4.0	0.999	cobble
18012709	69.6728	39.4826	7	Erratic	5.0	0.999	cobble
Telen							
16010901	69.6534	39.7060	68	Erratic	2.0	0.996	-
16010902	69.6515	39.7125	91	Erratic	2.0	1.000	1.3×0.9×0.8
16011201	69.6509	39.6860	4	Erratic	2.3	0.987	0.8×0.7×0.3
16011202	69.6517	39.6862	4	Erratic	2.5	0.998	2.1×1.3×0.8

[*a] Latitudes, longitudes, and altitudes were recorded in the field with a Garmin GPSmap 62sc.

[*b] The shielding factor was calculated using the online Geometric Shielding Calculator version 1.1 (Balco *et al*., 2008).

Table 2 Analytical results and information for surface exposure dating

Sample name	Sample weight(g) [*a]	9Be carrier weight (mg) [*a]	Al in quartz (μg/g)	Aditional ^{27}Al carrier weight (mg) [*a]	^{10}Be/^{9}Be ratio (×10^{-15}) [*b*c]	^{26}Al/^{27}Al ratio (×10^{-15}) [*b*d]	^{10}Be conc. (×10^{4} atoms/g) [*e*f]	^{26}Al conc. (×10^{4} atoms/g) [*e*g]	^{10}Be age (ka) [*h*i]	^{10}Be ± int (ka) [*j]	^{10}Be ± ext (ka) [*k]	^{26}Al age (ka) [*h*i]	^{26}Al ± int (ka) [*j]	^{26}Al ± ext (ka) [*k]	^{26}Al/^{10}Be ratio	Procedural blank number
Skarvsnes																
16012401	38.52	0.4736	69.69	0	148.5 ± 4.91	400.0 ± 15.1	9.68 ± 0.46	61.99 ± 2.35	14.36	0.68	1.09	12.94	0.49	1.22	6.40 ± 0.39	1
16012403	39.13	0.4747	34.27	1.1019	100.6 ± 3.85	248.5 ± 10.3	5.68 ± 0.38	34.41 ± 1.45	9.10	0.61	0.81	7.73	0.33	0.74	6.06 ± 0.48	1
16012501	38.60	0.4758	161.06	0	109.6 ± 4.12	111.6 ± 6.10	6.51 ± 0.40	39.90 ± 2.20	9.69	0.60	0.83	8.33	0.46	0.86	6.13 ± 0.51	1
16012402	44.63	0.4737	78.04	0	66.90 ± 2.77	-	4.37 ± 0.21	-	7.63	0.36	0.58	-	-	-	-	2
16012404	40.93	0.4415	28.61	0.9575	63.66 ± 2.37	-	4.18 ± 0.18	-	6.92	0.30	0.51	-	-	-	-	2
16012503	44.66	0.4756	84.12	0	74.02 ± 3.36	209.6 ± 29.6	4.90 ± 0.25	39.25 ± 5.56	7.86	0.40	0.61	8.87	1.26	1.48	8.02 ± 1.20	2
16012201	44.05	0.4772	286.51	0	62.45 ± 2.35	51.75 ± 4.79	4.14 ± 0.18	32.99 ± 3.07	6.60	0.29	0.49	7.35	0.69	0.94	7.96 ± 0.82	2
16012301	43.56	0.4753	15.07	1.1226	61.26 ± 2.29	-	4.09 ± 0.18	-	6.71	0.29	0.49	-	-	-	-	2
18010904	58.58	0.4822	148.31	0	129.5 ± 4.20	138.9 ± 6.34	6.81 ± 0.23	44.24 ± 2.06	8.85	0.30	0.60	7.92	0.37	0.78	6.36 ± 0.37	3
18010905	58.79	0.4739	87.24	0	317.5 ± 9.18	648.0 ± 17.0	16.9 ± 0.50	120.6 ± 3.23	21.24	0.63	1.41	21.38	0.58	1.95	7.12 ± 0.28	3
18010911	54.67	0.4791	34.94	0	97.41 ± 4.05	-	5.52 ± 0.24	-	7.80	0.34	0.57	-	-	-	-	3
18010916	60.11	0.3430	89.99	0	122.3 ± 5.24	165.3 ± 6.90	4.50 ± 0.20	31.41 ± 1.35	7.12	0.32	0.53	7.00	0.30	0.68	6.99 ± 0.43	3
18010924	58.54	0.3440	26.56	0	100.5 ± 2.87	488.6 ± 15.9	3.78 ± 0.12	26.98 ± 0.91	6.45	0.20	0.43	6.47	0.22	0.60	7.15 ± 0.33	3
18010929	57.97	0.3431	257.21	0	104.7 ± 3.45	52.61 ± 2.93	3.97 ± 0.14	28.80 ± 1.65	7.17	0.26	0.49	7.29	0.42	0.76	7.26 ± 0.49	3
17121703	60.16	0.3419	194.66	0	136.1 ± 5.83	95.12 ± 3.72	4.93 ± 0.24	41.29 ± 1.62	7.37	0.35	0.56	8.65	0.34	0.82	8.37 ± 0.52	4
18010906	59.48	0.4775	209.59	0	111.3 ± 4.11	93.03 ± 3.91	5.74 ± 0.24	43.48 ± 1.83	7.51	0.31	0.54	8.00	0.34	0.77	7.58 ± 0.45	4
18010914	51.78	0.3406	40.18	0	118.9 ± 5.47	-	4.95 ± 0.26	-	7.28	0.38	0.58	-	-	-	-	4
18010919	60.67	0.3408	133.00	0	116.8 ± 4.54	120.6 ± 4.97	4.15 ± 0.19	35.75 ± 1.48	6.75	0.31	0.50	8.11	0.34	0.78	8.61 ± 0.53	4
17121801	39.55	0.3401	132.17	0	81.84 ± 2.86	-	4.47 ± 0.17	-	7.64	0.30	0.54	-	-	-	-	5
17121804	40.80	0.3406	79.40	0	83.05 ± 3.47	-	4.41 ± 0.20	-	7.90	0.37	0.59	-	-	-	-	5
Skallen																
15123101	43.85	0.4754	69.83	0	62.85 ± 2.65	188.1 ± 8.89	4.17 ± 0.20	29.21 ± 1.39	6.97	0.34	0.53	6.86	0.33	0.68	7.00 ± 0.47	2
15123102	40.42	0.4764	97.43	0	55.28 ± 2.76	-	3.94 ± 0.23	-	6.61	0.38	0.55	-	-	-	-	2
16010601	45.09	0.4763	157.41	0	67.07 ± 2.71	-	4.37 ± 0.20	-	7.66	0.35	0.57	-	-	-	-	2
17122702	56.53	0.2909	52.77	0	122.4 ± 4.29	-	3.96 ± 0.17	-	6.56	0.29	0.48	-	-	-	-	4
18012706	54.67	0.2904	134.51	0	104.6 ± 4.19	89.69 ± 3.99	3.45 ± 0.17	26.88 ± 1.20	6.02	0.30	0.47	6.57	0.30	0.64	7.78 ± 0.52	4
18012805	58.57	0.2895	202.41	0	137.1 ± 6.13	70.64 ± 3.30	4.29 ± 0.22	31.88 ± 1.49	7.28	0.37	0.57	7.57	0.36	0.74	7.43 ± 0.52	4
18012812	58.53	0.2891	69.07	0	97.11 ± 5.34	150.2 ± 5.93	2.96 ± 0.20	23.11 ± 0.92	5.43	0.36	0.48	5.93	0.24	0.56	7.80 ± 0.60	4
18012709	39.57	0.3396	475.78	0	18.91 ± 1.30	-	0.85 ± 0.09	-	1.54	0.16	0.19	-	-	-	-	5
Telen																
16010901	59.88	0.3436	77.46	0	67.00 ± 2.71	-	2.40 ± 0.11	-	4.15	0.19	0.31	-	-	-	-	3
16010902	63.90	0.3429	104.82	0	114.2 ± 4.20	-	3.94 ± 0.15	-	6.64	0.26	0.47	-	-	-	-	3
16011201	49.38	0.3447	78.85	0	11.35 ± 1.25	-	0.34 ± 0.07	-	0.61	0.13	0.13	-	-	-	-	5
16011202	48.30	0.3416	47.32	0	5.89 ± 0.88	-	0.09 ± 0.06	-	0.17	0.11	0.11	-	-	-	-	5

[*a] The weights of the samples and carriers show residual weights for AMS after aliquoting for Al measurement.

[*b] All nuclide ratio mesured by PRIME lab (Purdue Rare Isotope Measurement Laboratory).

[*c] Measurements are normalized to 07KNSTD (Nishiizumi et al., 2007) Be standard material with a nominal ^{10}Be/^{9}Be of 2.851×10^{-12}.

[*d] Meaasurments are normalized to KNSTD (Nishiizumi, 2004) Al standard material with a nominal ^{26}Al/^{27}Al of 1.818×10^{-12}.

[*e] Concentrations involved the subtraction of background ^{10}Be and ^{26}Al atoms measured in one procedural blank.

[*f] Propagated uncertainties of ^{10}Be include an error in the uncertainties on the AMS measurements of both the samples and the blank.

[*g] Propagated uncertainties of ^{26}Al include an error in the uncertainties on the AMS measurements of both the samples and the blank and 3% stable ^{27}Al measurement (ICP-MS) uncertainty.

[*h] Ages were calculated with the LSDn scale CRONUS-Earth online calculators, V3 (Balco et al. 2008) (http://hess.ess.washington.edu).

[*i] A density of 2.7 g/cm3 was used based on the gniss rock of the surface samples and assuming zero erosion.

[*j] int = Internal uncertainties; includes only concentration uncertainties based on lab/AMS measurements.

[*k] ext = External uncertainties; includes internal uncertainties plus scaling and production rate uncertainties.

Table 3 Procedural blank data.

Blank No.	^{9}Be carrier weight (mg)	^{27}Al carrier weight (mg)	^{10}Be/^{9}Be ratio ($\times10^{-15}$)	^{26}Al/^{27}Al ratio ($\times10^{-15}$)	^{10}Be conc.($\times 10^{4}$ atoms)	^{26}Al conc. (10^{4} atoms)
1	0.4759	1.4409	30.5 ± 2.67	2.58 ± 1.87	96.95 ± 8.49	8.29 ± 6.00
2	0.4743	1.4385	5.23 ± 0.83	1.42 ± 2.04	16.58 ± 2.63	4.55 ± 6.56
3	0.4798	1.4517	3.12 ± 0.61	11.9 ± 3.18	10.01 ± 1.96	38.4 ± 10.3
4	0.4767	1.4330	4.43 ± 1.56	0.70 ± 1.00	14.12 ± 4.96	2.23 ± 3.21
5	0.4747	1.4442	2.91 ± 0.56	0.75 ± 1.08	9.24 ± 1.82	2.41 ± 3.47

Table 4 Conventional and calibrated radiocarbon ages of the lake sediment core and raised beach data.

ID	Material	Upper-depth (cm)	Lower-depth (cm)	$\delta^{13}C$ (‰)	Conventioal radiocarbon age (yr BP)	1 sigma	Median age (cal. yr BP)	Calendar age 2 sigma upper (cal. yr BP)	Calendar age 2 sigma lower (cal. yr BP)	Environmental	Cal. Curve	Oxcal
Lake Namazu-Ike												
17NZ-SC1-002	Bulk sediment	1.9	3.9	-19.4 ± 0.3	1236	17	1109	1061	1179	lacustrine	SHCal13	17NZ-SC1-002,1236,17
17NZ-SC1-002_biomat	Biological mat	1.9	3.9	-22.3 ± 0.4	1139	20	997	956	1059	lacustrine	SHCal13	17NZ-SC1-002_biomat,1139,20
17NZ-SC1-031	Bulk sediment	57.9	59.8	-21.3 ± 0.2	3295	20	3476	3400	3563	lacustrine	SHCal13	17NZ-SC1-031,3295,20
17NZ-SC1-054	Bulk sediment	102.2	104.2	-22.8 ± 0.2	5422	22	6201	6020	6282	lacustrine	SHCal13	17NZ-SC1-054,5422,22
17NZ-SC1-062	Bulk sediment	117.7	119.6	-24.2 ± 0.4	2053	23	1962	1906	2013	lacustrine	SHCal13	17NZ-SC1-062,2053,23
17NZ-SC1-062_biomat	Biological mat	117.7	119.6	-26.3 ± 0.4	1154	20	1015	962	1059	lacustrine	SHCal13	17NZ-SC1-062_biomat,1154,20
Lake Naga-Ike												
17NG-SC1-002	Bulk sediment	1.4	2.9	-22.6 ± 0.3	507	17	511	497	529	lacustrine	SHCal13	17NG-SC1-002,507,17
17NG-SC1-041	Bulk sediment	57.8	59.2	-22.8 ± 0.4	5709	25	6446	6324	6540	lacustrine	SHCal13	17NG-SC1-041,5709,25
17NG-SC1-083	Bulk sediment	119.9	121.3	-23.0 ± 0.9	6418	42	7312	7180	7423	lacustrine	SHCal13	17NG-SC1-083,6418,42
17NG-SC1-089	Bulk sediment	127.1	128.5	-22.2 ± 0.7	6842	54	7641	7566	7782	lacustrine	SHCal13	17NG-SC1-089,6842,54
Lake Oku-Ike												
17OK-SC1-001	Bulk sediment	0.0	1.7	-23.7 ± 0.2	1162	18	1016	965	1059	lacustrine	SHCal13	17OK-SC1-001,1162,18
17OK-SC1-073	Bulk sediment	107.5	109.2	-28.6 ± 0.2	4863	22	5523	5473	5608	lacustrine	SHCal13	17OK-SC1-073,4863,22
17OK-SC1-080	Bulk sediment	119.6	121.4	-27.5 ± 1.1	5923	51	6701	6546	6851	lacustrine	SHCal13	17OK-SC1-080,5923,51
17OK-SC1-089	Bulk sediment	135.2	137.0	-23.9 ± 1.4	6300	70	7176	6955	7324	lacustrine	SHCal13	17OK-SC1-089,6300,70
Lake Hyoutan-Ike												
17HY-SC2-001	Bulk sediment	0.0	1.3	-25.1 ± 0.3	155	17	98	-	269	lacustrine	SHCal13	17HY-SC2-001,155,17
17HY-SC2-088	Bulk sediment	116.6	117.9	-22.2 ± 1.4	7287	77	8071	7880	8290	lacustrine	SHCal13	17HY-SC2-088,7287,77
Lake Oyako-Ike												
17OY-SC1-001	Bulk sediment	0.0	1.1	-11.9 ± 0.7	881	33	744	680	797	lacustrine	SHCal13	17OY-SC1-001,881,33
17OY-SC1-100*	Bulk sediment	106.7	107.7	-21.5 ± 0.3	3333	22	2297	2030	2640	Marine	Marine13	17OY-SC1-100*,3333,22
17OY-SC1-200*	Bulk sediment	214.4	215.5	-25.5 ± 0.3	4903	24	4261	3960	4531	Marine	Marine13	17OY-SC1-200*,4903,24
17OY-SC1-300*	Bulk sediment	322.1	323.2	-29.8 ± 0.3	8547	28	8285	8049	8501	Marine	Marine13	17OY-SC1-300*,8547,28
17OY-SC1-400*	Bulk sediment	429.9	431.0	-20.7 ± 1.3	8772	98	8542	8253	8951	Marine	Marine13	17OY-SC1-400*,8772,98
Beaches												
Trench-1*	Polychaete tube	-	-	0.2 ± 0.4	6841	26	6551	6308	6781	Marine	Marine13	Trench-1*,6841,26
Trench_01*	Fossil shell	-	-	-0.4 ± 0.6	7445	29	7249	6997	7437	Marine	Marine13	Trench_01*,7445,29
Trench_02*	Polychaete tube	-	-	0.1 ± 0.6	6821	28	6530	6295	6756	Marine	Marine13	Trench_02*,6821,28

Ages indicated with an asterisk were corrected for the regional marine reservoir effect (1120 years).

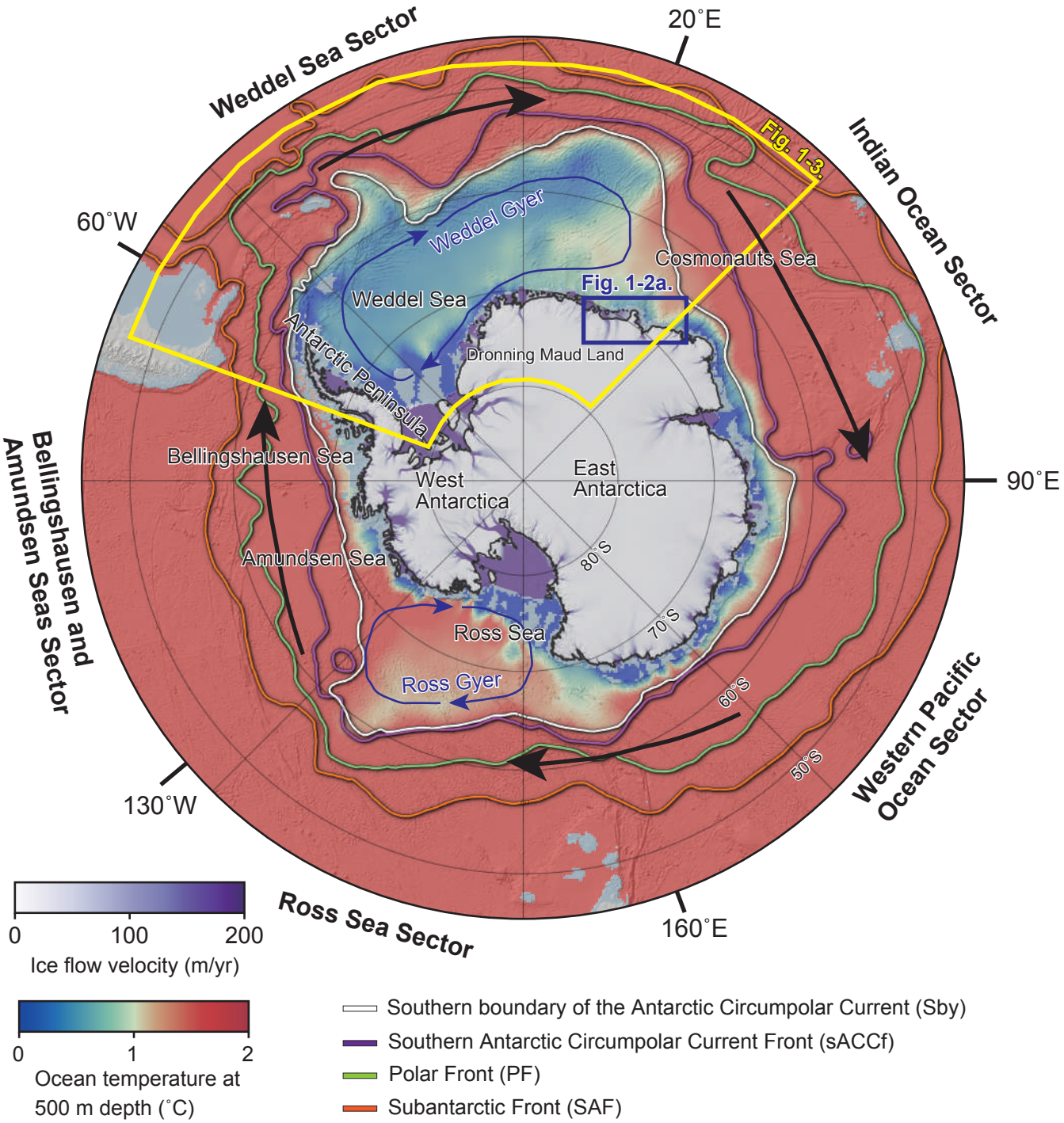

Fig. 1-1. Overview map of Antarctica with InSAR-Based ice velocity (Rignot et al., 2017) and ocean temperatures at 500 m depth (Locarnini et al., 2013), including the regions discussed in this thesis. Fronts related to the Antarctic Circumpolar Current (ACC) are shown as solid lines (Orsi et al., 1995). The black and blue arrow shows the flow direction of the ACC and main gyres of the Southern Ocean, respectively. The base map is from Quantarctica GIS package compiled by the Norwegian Polar Institute (http://www.quantarctica.org/). The classification of the five ocean sectors was based on a previous oceanic study (Parkinson and Cavalieri et al., 2012).

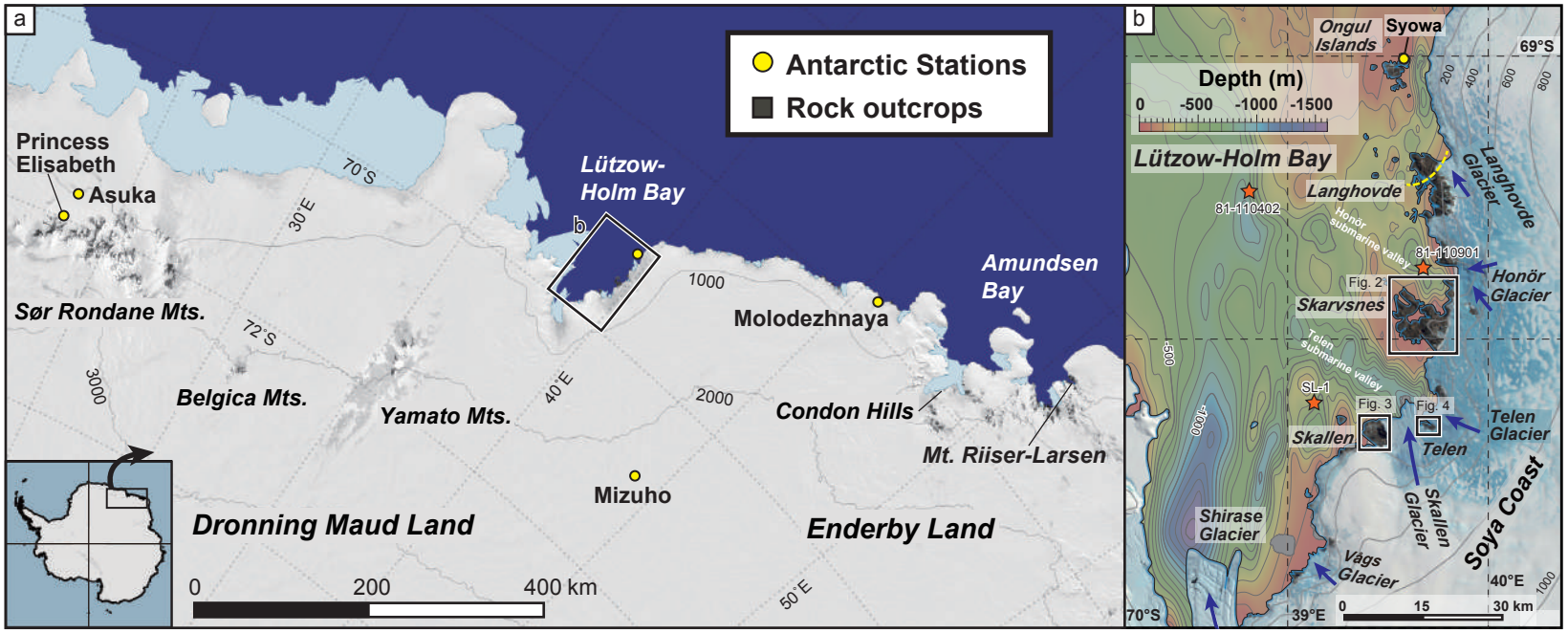

Fig. 1-2. (a) Overview map of Antarctica, showing the study area in the Indian Ocean sector (Dronning Maud Land and Enderby Land), based on Quantarctica GIS package compiled by the Norwegian Polar Institute (http://www.quantarctica.org/). (b) Satellite image of the Soya Coast. Blue arrows indicate the flow directions of major ice streams in this area. Areas north of the dashed yellow line were thought to be not covered by the EAIS during the LGM (Miura et al., 1998a). Orange stars show marine sediment sampling sites that include calcareous foraminifera *Bulimina aculeate*. Bathymetry is from the regional bathymetric chart of Moriwaki and Yoshida (2002).

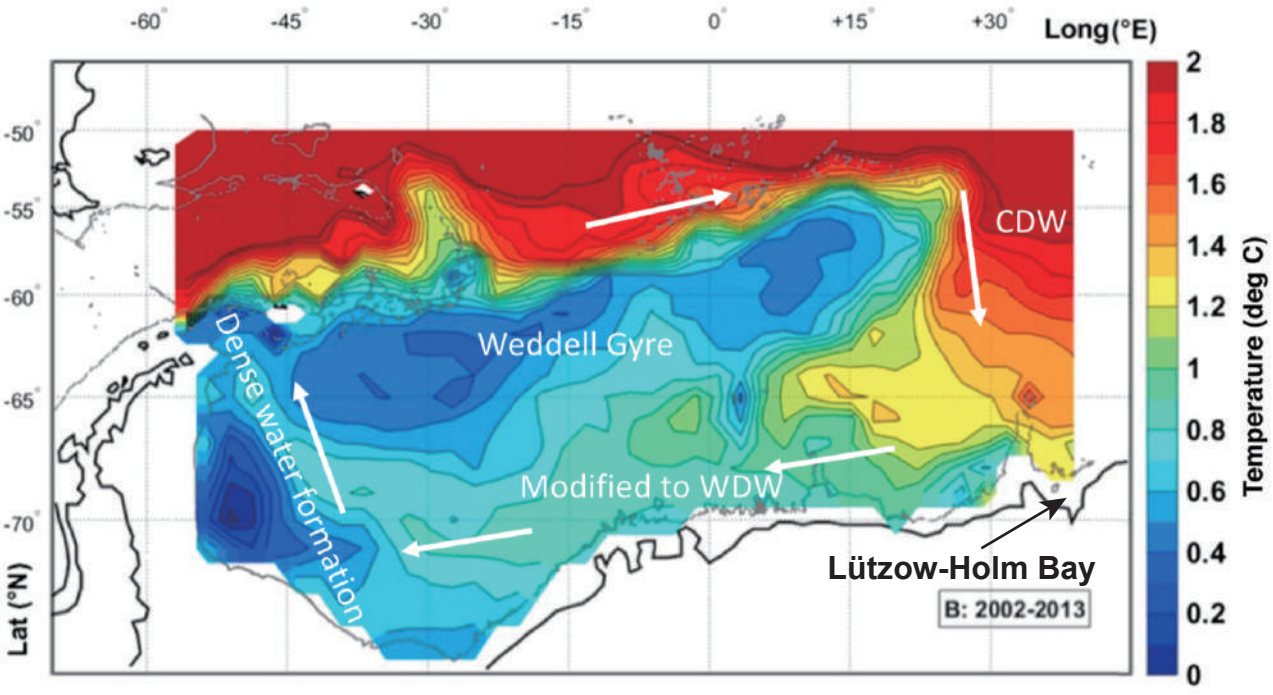

Fig. 1-3. The Weddell Gyre: temperature (˚C) at the subsurface temperature maximum, derived from optimally interpolated Argo float data as in Vernet et al. (2019). The figure shows clearly the penetration of Circumpolar Deep Water (CDW) from the east on the southern side of the gyre facing the Lützow-Holm Bay. The arrows show the dominant middepth flow direction of the gyre, and WDW is Warm Deep Water.

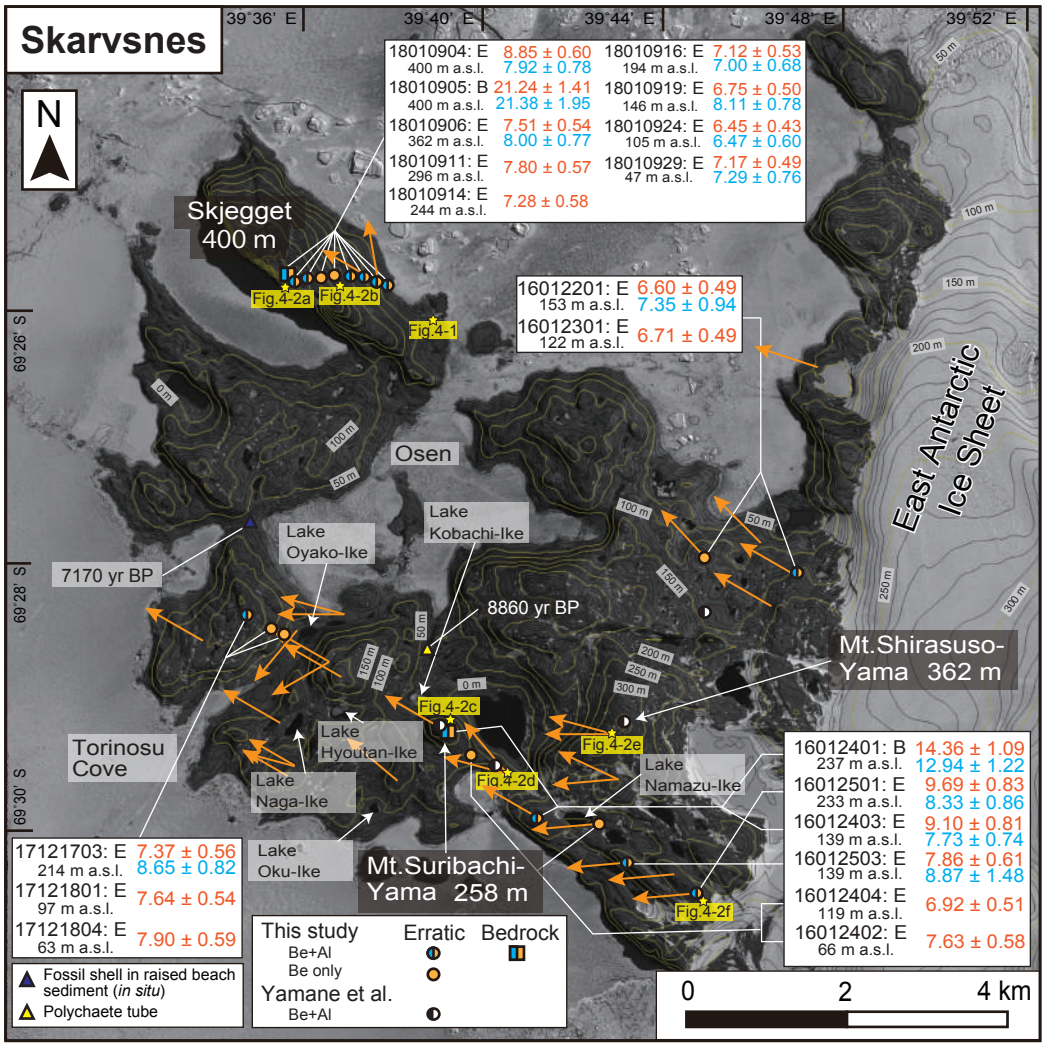

Fig. 2-1. Satellite image of Skarvsnes derived from Panchromatic Remote-sensing Instrument for Stereo Mapping mounted on the Advanced Land Observing Satellite (ALOS/PRISM). Yellow stars show each location of Fig. 8 and 9. Orange arrows show the orientation of striations identified in this study. Sample sites and ages for surface exposure dating are also shown, with orange and blue symbols/numbers indicating Be and Al SED sites/ages, respectively. Contours are 10 m (black) and 50 m (yellow) intervals, and are derived from the TanDEM-X 90 m Digital Elevation Model (Wessel et al., 2018).

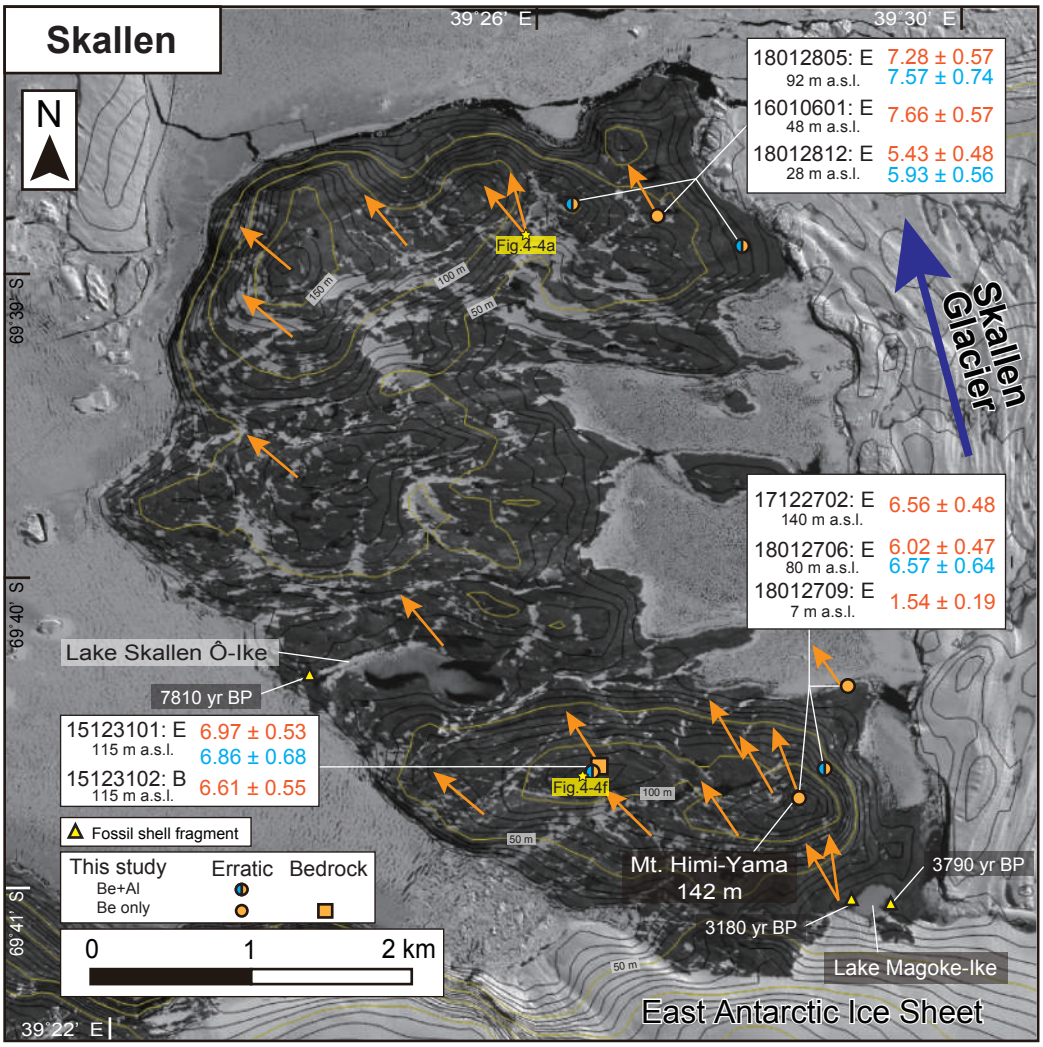

Fig. 2-2. Satellite image of Skallen derived from ALOS/PRISM. Yellow stars show each location of Fig.4-4. The description of the figure is as for Fig. 2-1.

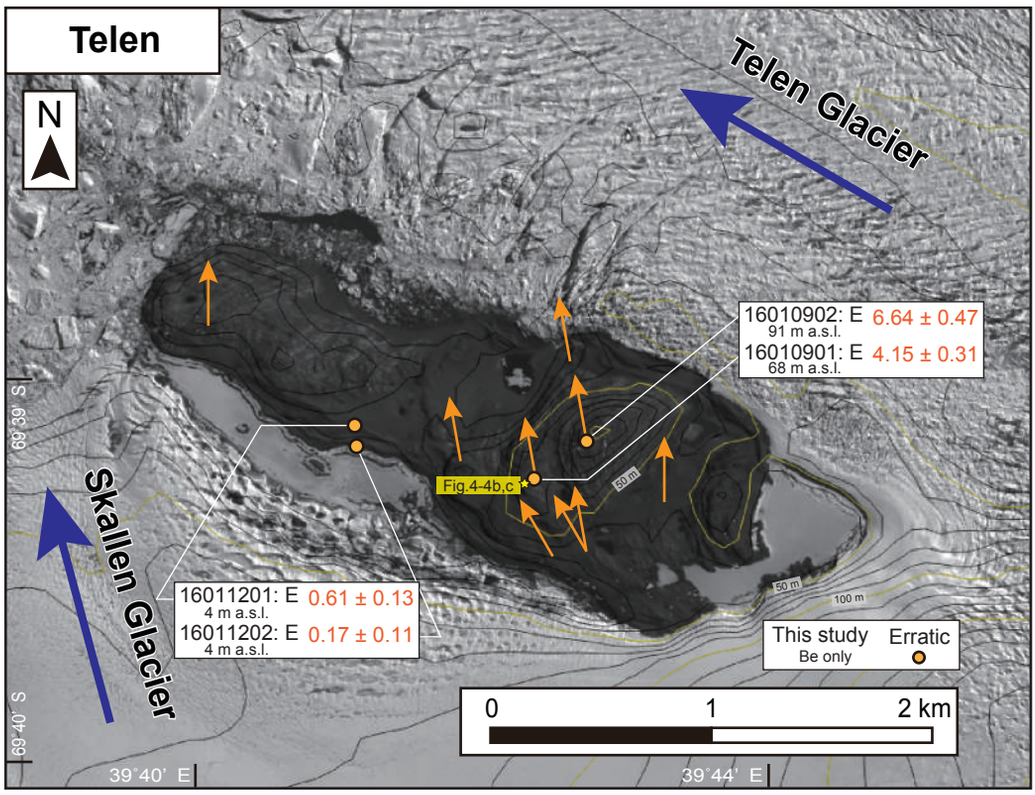

Fig. 2-3. Satellite image of Telen derived from ALOS/PRISM. Yellow stars show each location of Fig.4-4. The description of the figure is as for Fig. 2-1.

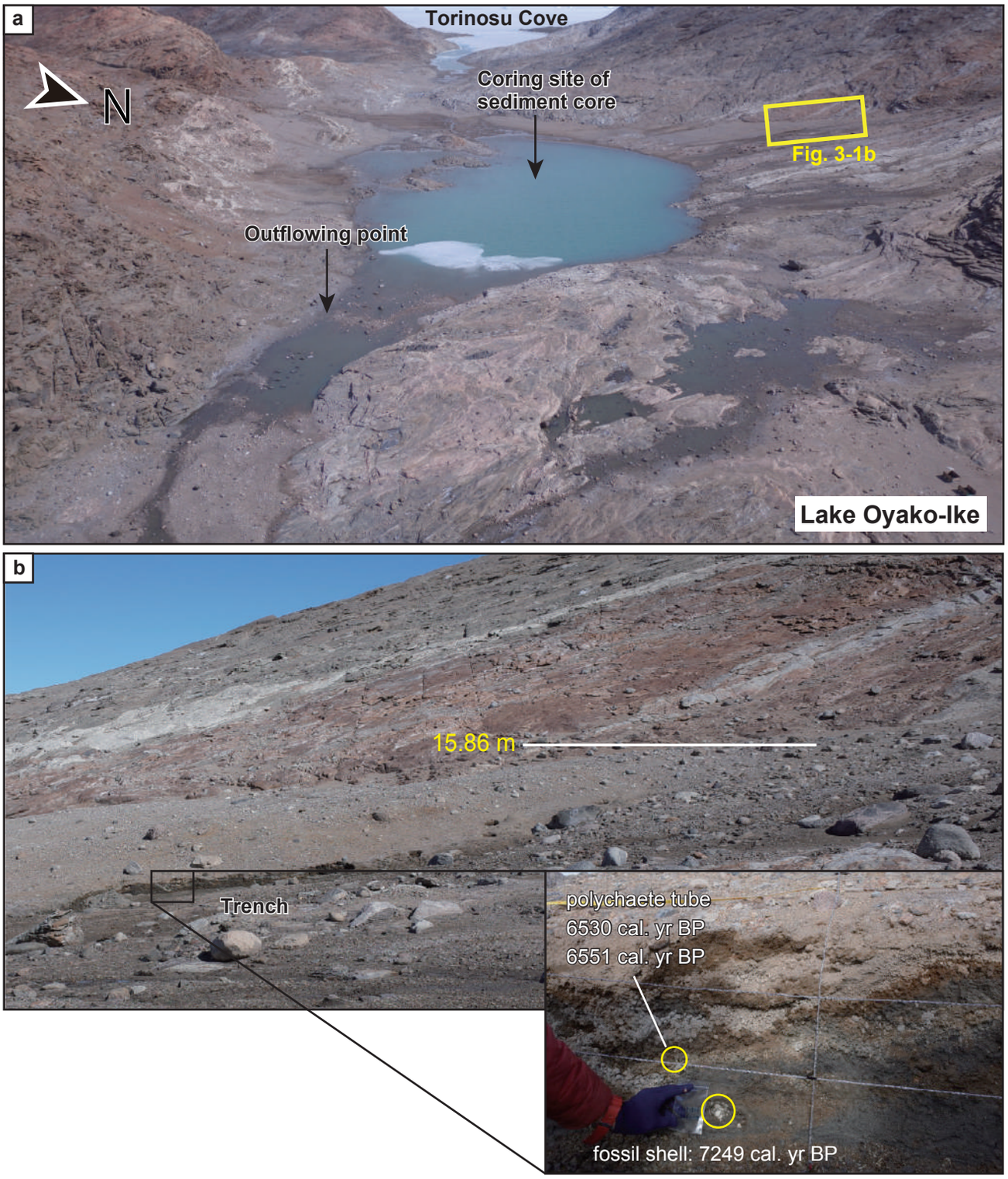

Fig. 3-1. Photographs of the landscape around the Lake Oyako-Ike, showing the water overflow point (2.37 ± 0.01 m a.s.l.; Takano et al., 2012), as taken in January 2017. The trench survey area and results of the ^{14}C ages is also shown.

Fig. 3-2. Sediment coring on a ice-covered lake using a newly developed portable engine-driven percussion piston corer (Suganuma et al., 2019) (Photo credit: Y. Suganuma).

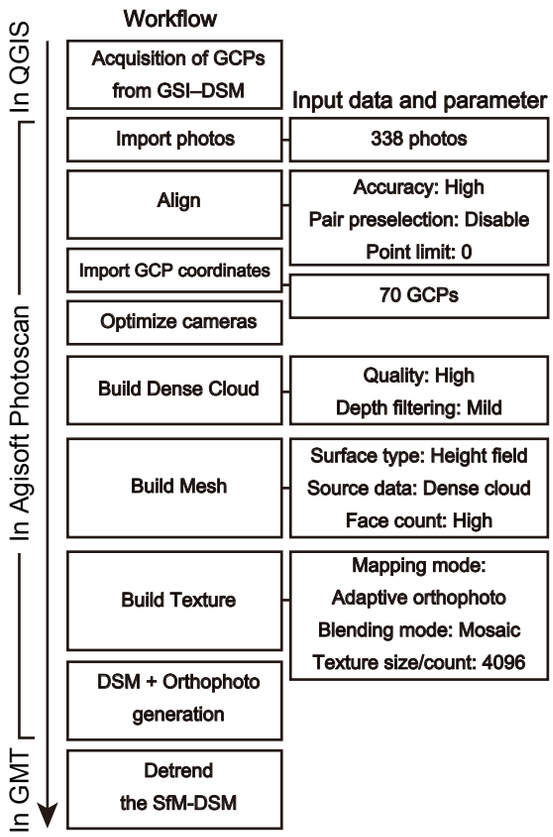

Fig. 3-3. Workflow, input data, and parameter for SfM–DSM construction

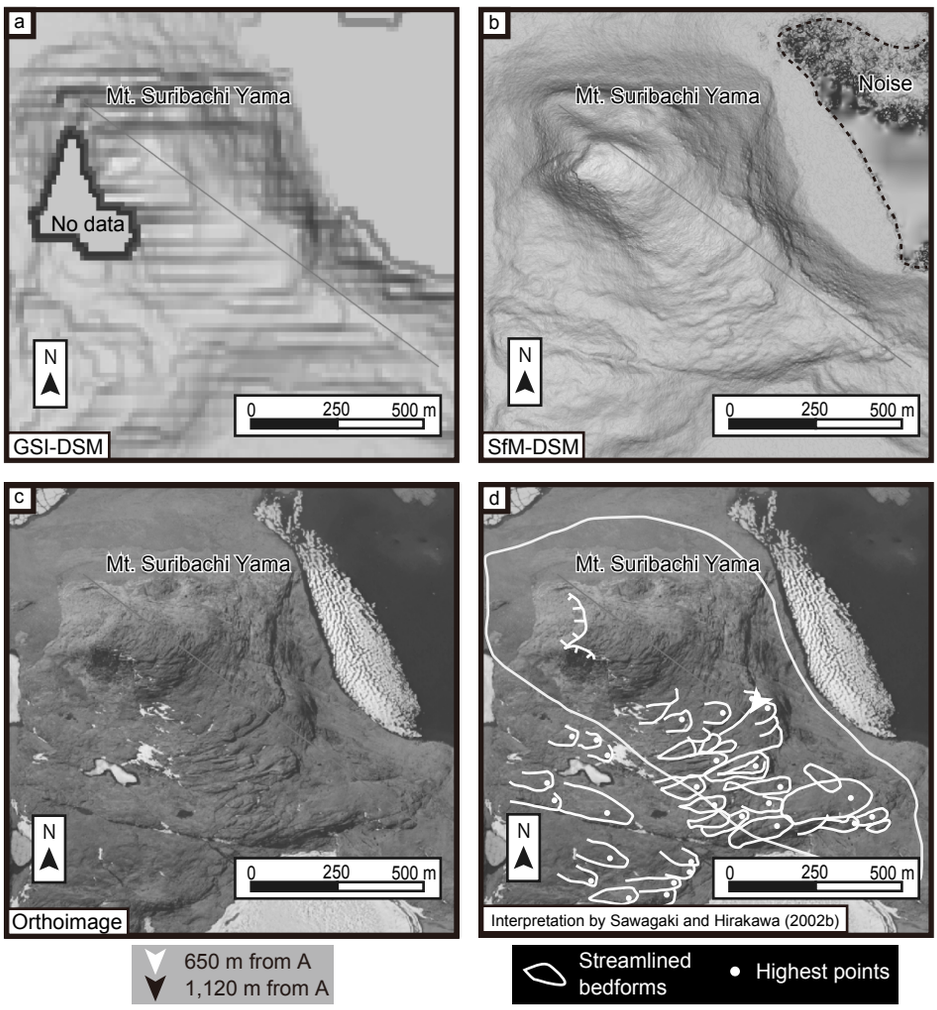

Fig.3-4. Comparison between SfM–DSM (present study: spatial resolution of 1.4 m) and GSI–DSM (previous data: resolution of 10 m) around Mt. Suribachi Yama. (a) Topographic map of the GSI–DSM, composed of elevation and slope images; (b) Topographic map of the SfM–DSM, composed of elevation and slope images; (c) Orthoimage; (d) Traced image of interpretation of streamlined bedforms by Sawagaki and Hirakawa (2002b) on orthoimage.

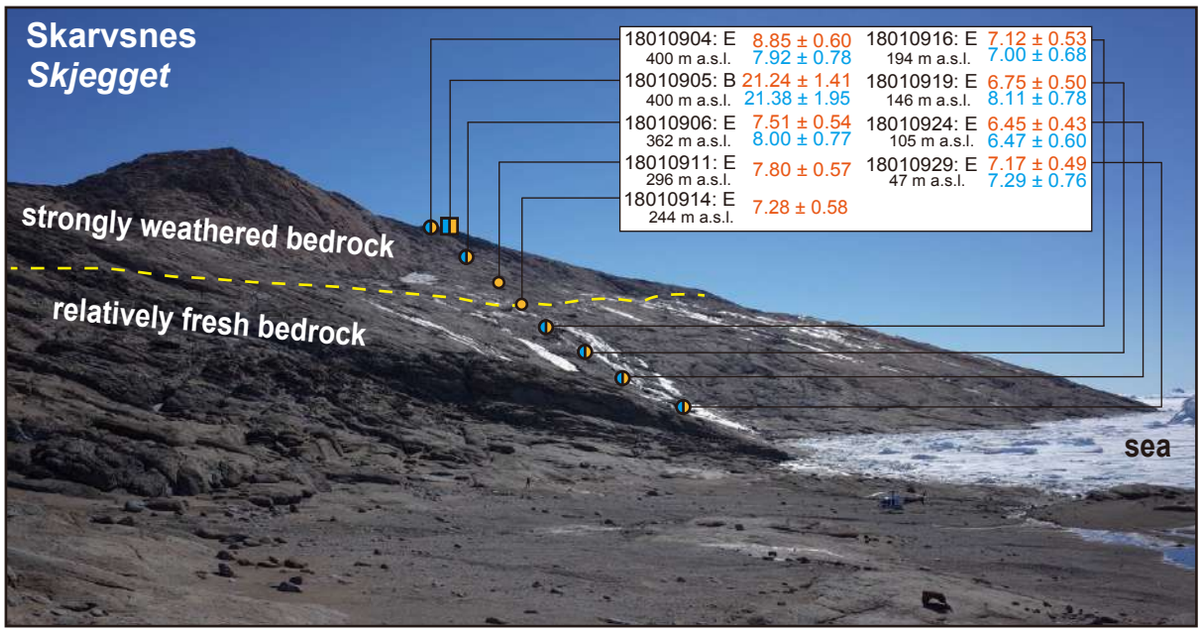

Fig. 4-1. Overview photograph of Skjegget viewed from the eastside site of Skjegget (Fig. 2-1), showing sampling sites for surface exposure dating. The dashed yellow line indicates the boundary (at 250 m–300 m a.s.l.) between strongly weathered (above) and relatively fresh (below) bedrock zones, as deduced from field observations. Above the line, bedrock is fractured with honeycomb weathering (Fig. 4-2a), whereas below the line, bedrock is relatively smooth and largely intact (Fig. 4-2b).

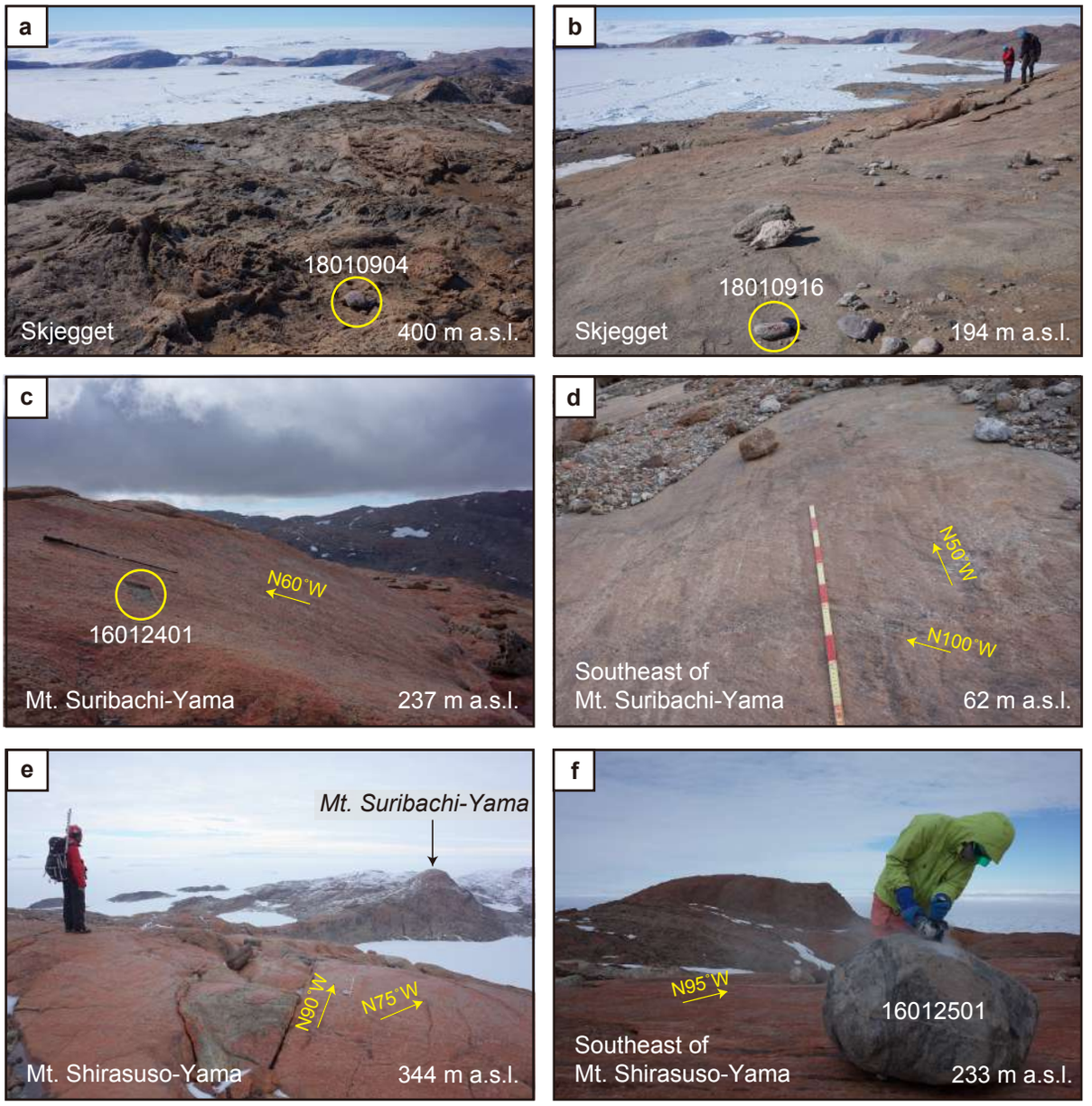

Fig. 4-2. Glacial geomorphology at Skarvsnes. Localities are shown in Fig. 2-1. (a) Bedrock at the top of Skjegget, showing intense honeycomb weathering. (b) Sampling site 18010916, at 194 m a.s.l. on Skjegget, showing relatively unweathered and smooth bedrock. (c) Mt. Suribachi-Yama, at an altitude of 237 m a.s.l. (d) Southeastern Mt. Suribachi-Yama, at an altitude of 62 m a.s.l. Cross-cutting striations are clearly observed. (e) Mt. Shirasuso-Yama, at an altitude of 344 m a.s.l. (f) Southern Mt. Shirasuso-Yama, at an altitude of 233 m a.s.l. Striation orientations vary depending on altitude. Yellow circles and arrows show samples for dating and orientations of striations, respectively.

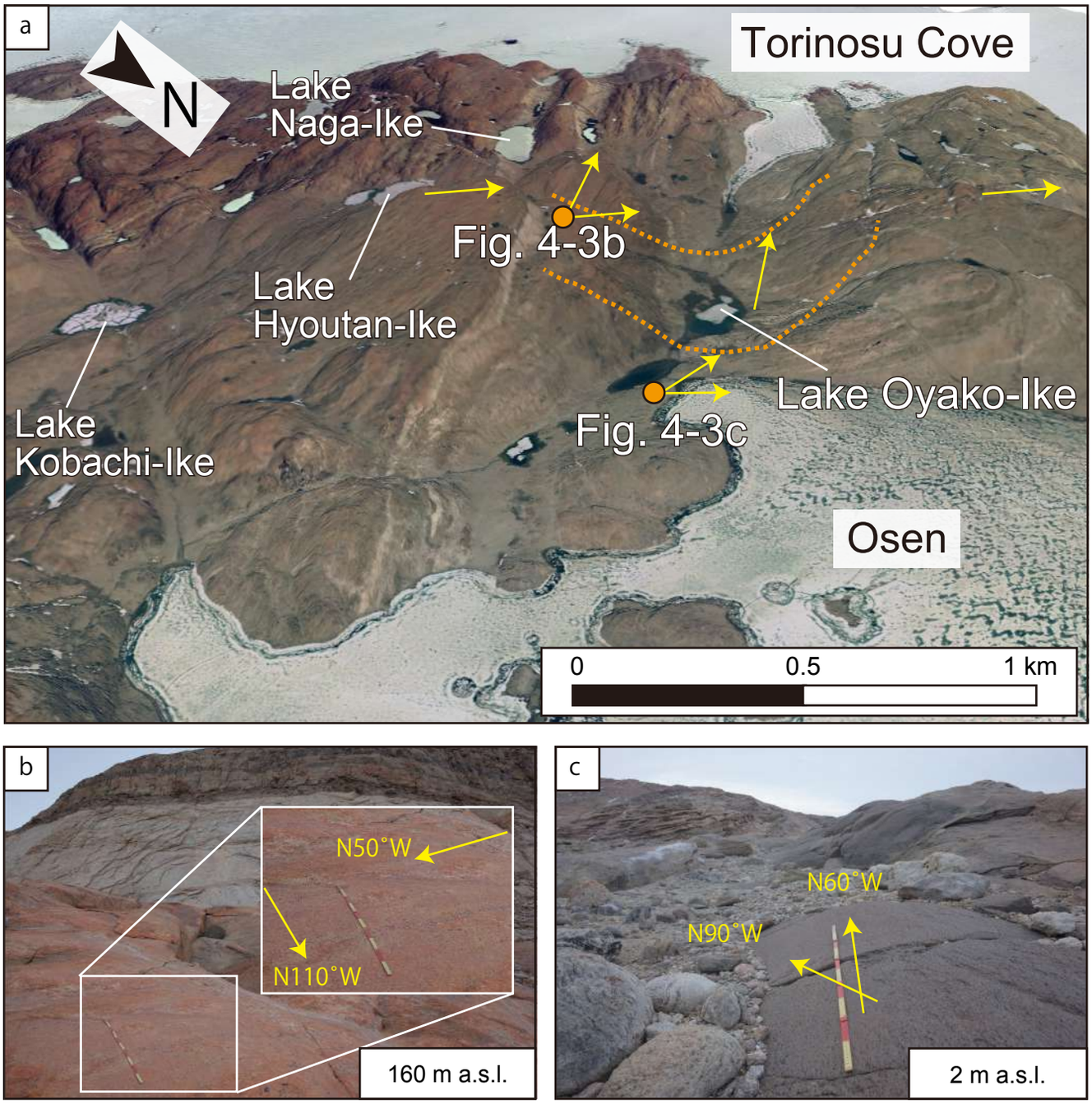

Fig. 4-3. (a) Bird's eye view of around Lake Oyako-Ike, 1.5 times vertically exaggerated of SfM-DSM. Directions of glacial striations differ depending on altitude of the location. (b)160 m a.s.l. at easten hill of Lake Oyako-Ike. (c) Striations at the 2 m a.s.l. of northeastan Lake Oyako-Ike. Orange circles show locations of (b) and (c). Orange dashed lines show U-shaped valley. Yellow arrows show directions of glacial striations.

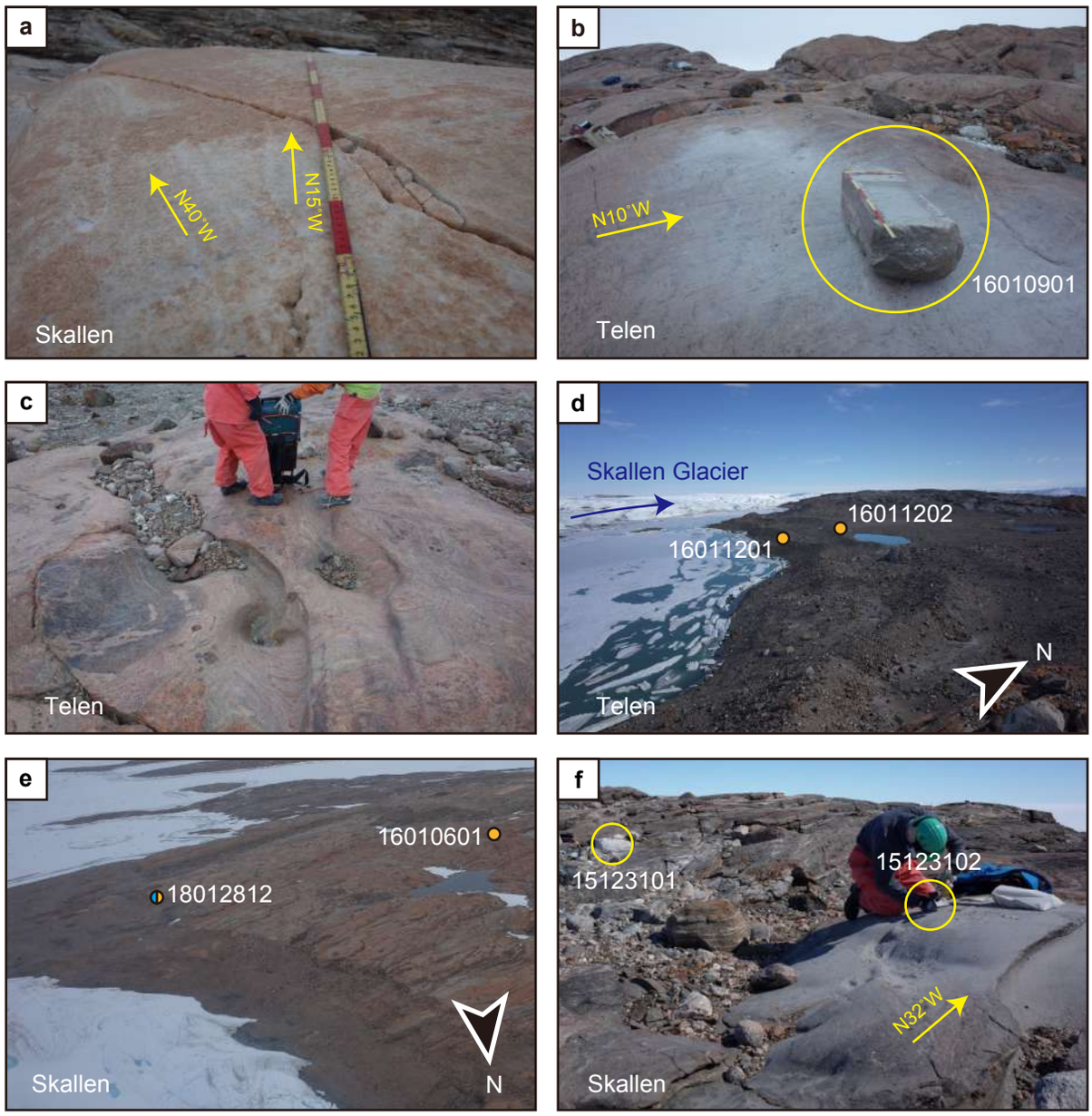

Fig. 4-4. Glacial geomorphology at Skallen and Telen. Localities are shown in Figs. 2-2 and 2-3. (a) N15˚W striations cross-cutting N40˚W striations at Skallen. (b) Sampling site 16010901 at Telen. (c) Sculpted erosional form at Telen. This form indicates a subglacial meltwater flow event (Sawagaki and Hirakawa, 1997). (d) Lateral moraines flanking Skallen Glacier at Telen. (e) Bird' s eye view looking from the northeastern side of Skallen. (f) Bedrock sampling at Skallen, showing unweathered and smooth bedrock. Yellow circles and arrows show samples for dating and orientations of striations, respectively.

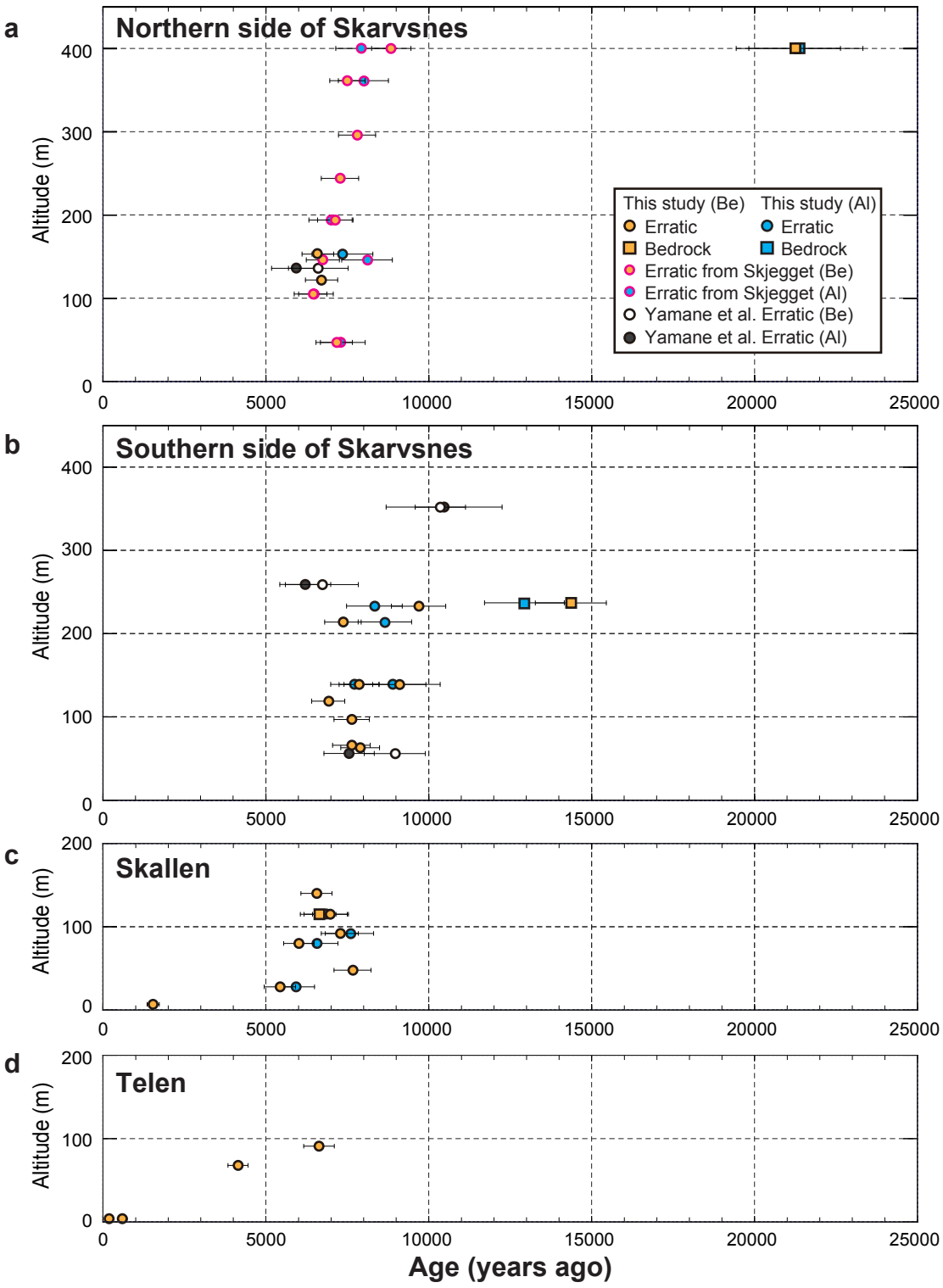

Fig. 4-5. (a–d) Surface exposure ages plotted against altitude for (a) Northern, (b) southern side of Skarvsnes (with surface exposure ages of erratic rocks from Yamane et al. (2011) also shown), (c) Skallen, and (d) Telen. Surface exposure ages of erratic rocks taken from Skjegget which best evidence for the main phase of thinning recorded in the southern Soya Coast is highlighted.

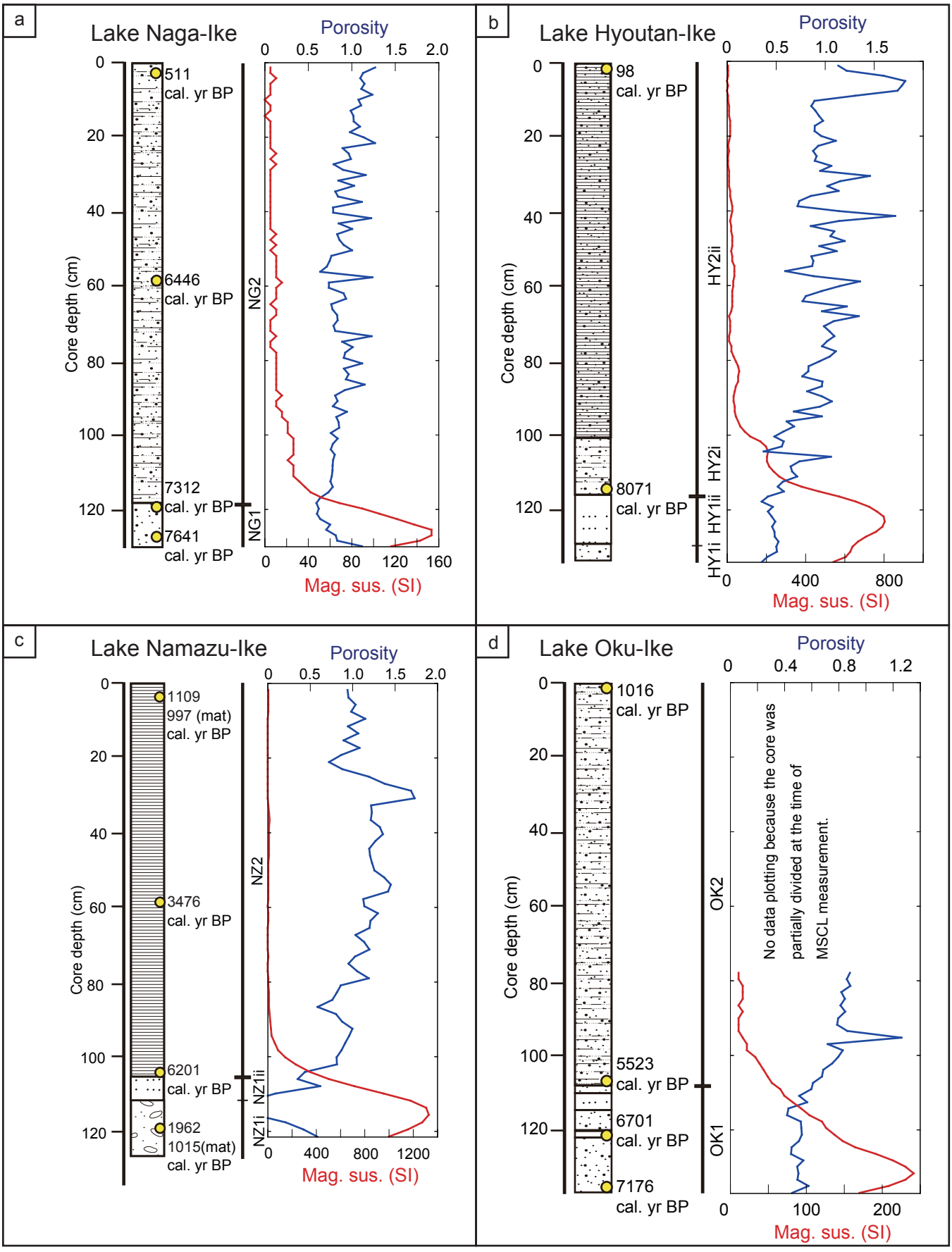

Fig.4-6. Sediment core showing the lithology, calibrated ^{14}C age, and physical property data (magnetic susceptibility and porosity) of (a) Lake Naga-Ike, (b) Lake Hyoutan-Ike, (c) Lake Namazu-Ike, and (d) Lake Oku-Ike.

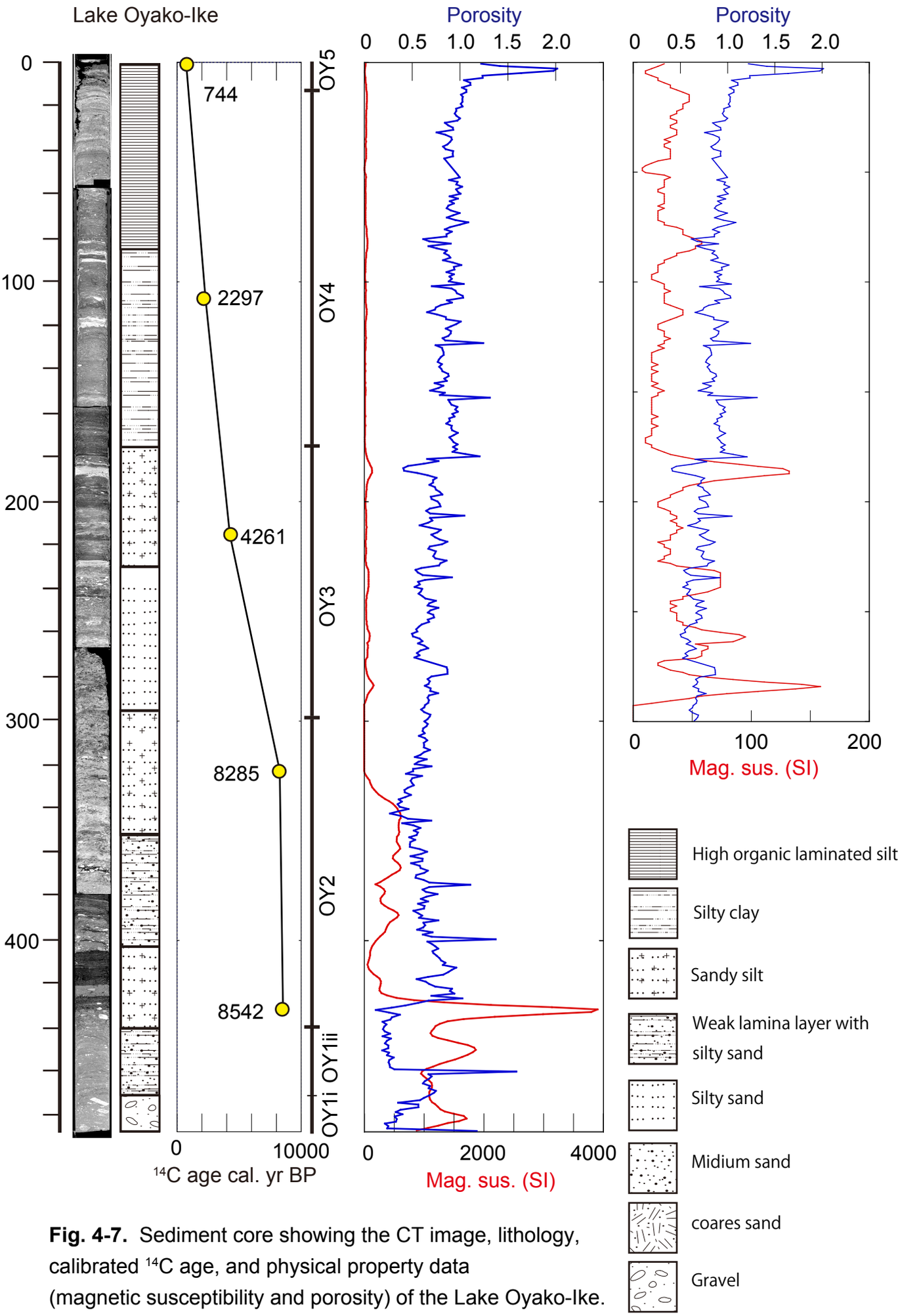

Fig. 4-7. Sediment core showing the CT image, lithology, calibrated ^{14}C age, and physical property data (magnetic susceptibility and porosity) of the Lake Oyako-Ike.

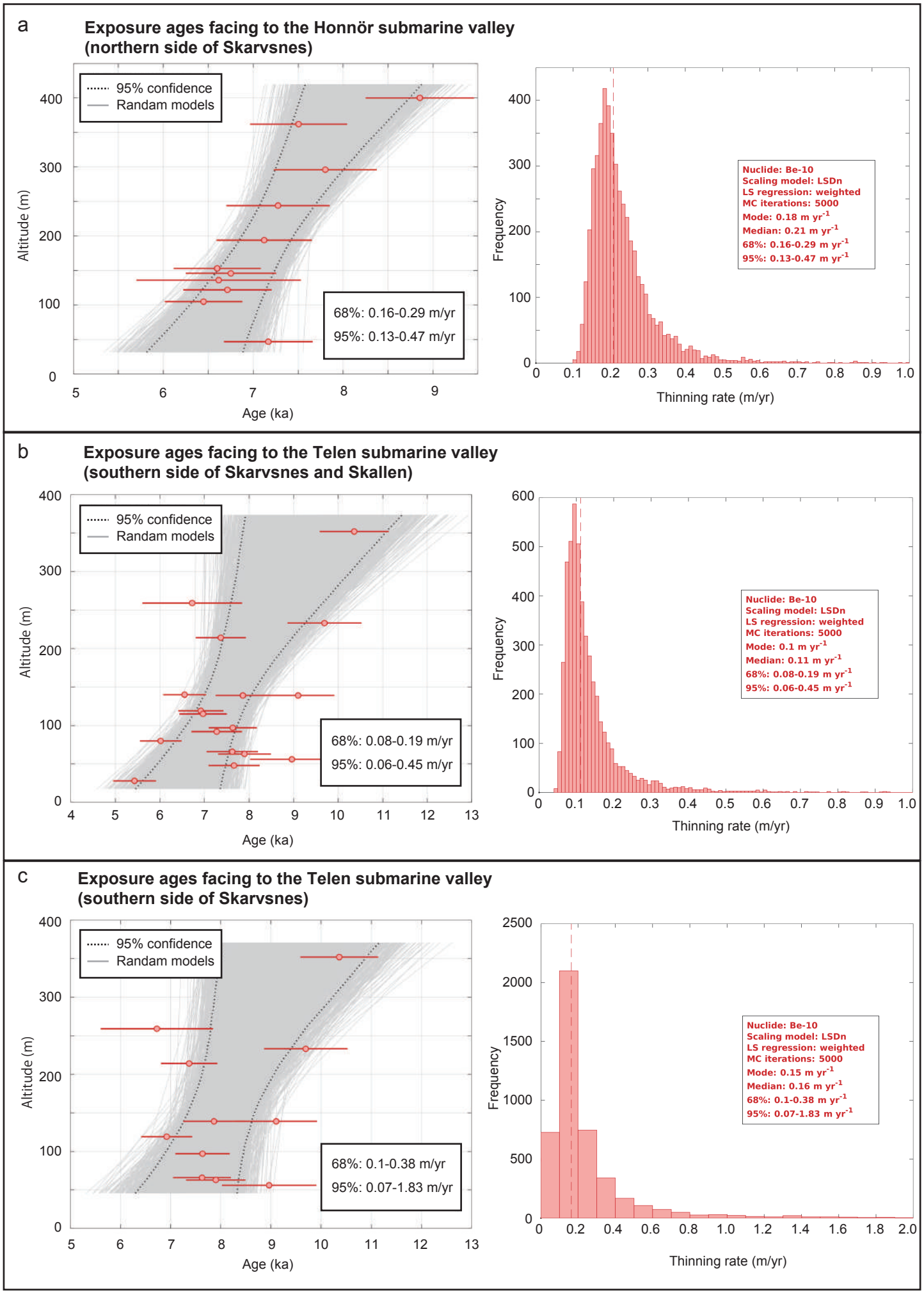
a
Exposure ages facing to the Honnör submarine valley
(northern side of Skarvsnes)
95% confidence
Randam models
68%: 0.16-0.29 m/yr
95%: 0.13-0.47 m/yr
Altitude (m)
Age (ka)
Nuclide: Be-10
Scaling model: LSDn
LS regression: weighted
MC iterations: 5000
Mode: 0.18 m yr-1
Median: 0.21 m yr-1
68%: 0.16-0.29 m yr-1
95%: 0.13-0.47 m yr-1
Frequency
Thinning rate (m/yr)
b
Exposure ages facing to the Telen submarine valley
(southern side of Skarvsnes and Skallen)
95% confidence
Randam models
68%: 0.08-0.19 m/yr
95%: 0.06-0.45 m/yr
Altitude (m)
Age (ka)
Nuclide: Be-10
Scaling model: LSDn
LS regression: weighted
MC iterations: 5000
Mode: 0.1 m yr-1
Median: 0.11 m yr-1
68%: 0.08-0.19 m yr-1
95%: 0.06-0.45 m yr-1
Frequency
Thinning rate (m/yr)
c
Exposure ages facing to the Telen submarine valley
(southern side of Skarvsnes)
95% confidence
Randam models
68%: 0.1-0.38 m/yr
95%: 0.07-1.83 m/yr
Altitude (m)
Age (ka)
Nuclide: Be-10
Scaling model: LSDn
LS regression: weighted
MC iterations: 5000
Mode: 0.15 m yr-1
Median: 0.16 m yr-1
68%: 0.1-0.38 m yr-1
95%: 0.07-1.83 m yr-1
Frequency
Thinning rate (m/yr)

Fig. 5-1.

Fig. 5-1. Results of linear regression analysis (Profile of ice surface lowering with time and histogram of modeled thinning rates). (a) exposure ages facing to the Honnör submarine valley (northern side of Skarvsnes), (b) exposure ages facing to the Telen submarine valley (southern side of Skarvsnes and Skallen), and (c) exposure ages facing to the Telen submarine valley (southern side of Skarvsnes).

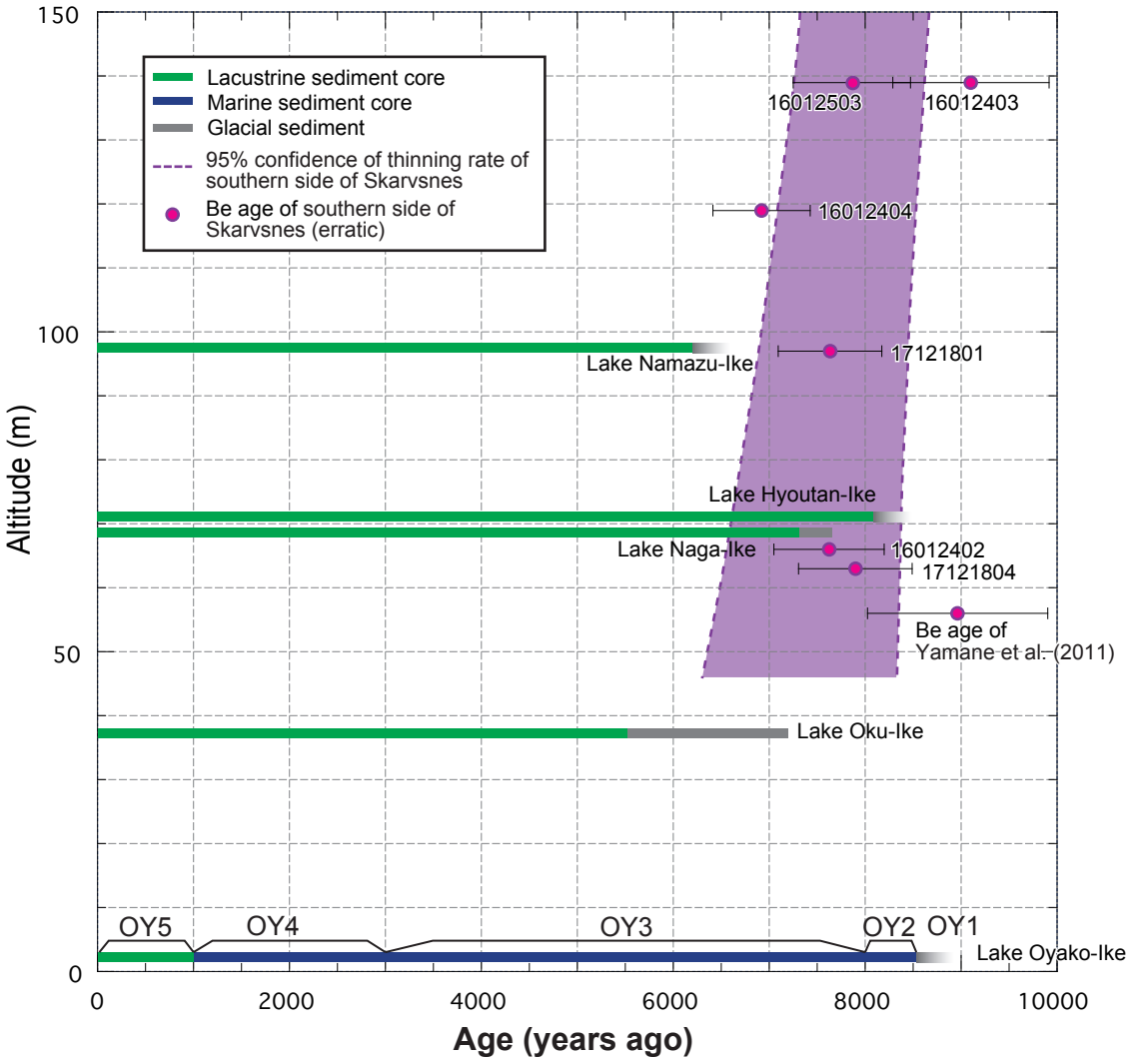

Fig. 5-2. Surface exposure ages and lake sediment ages plotted against altitude for southern side of Skarvsnes (with surface exposure ages of erratic rocks from Yamane et al., 2011 also shown). Purple dashed line show 95% confidence of thinning rate of southern side of Skarvsnes.

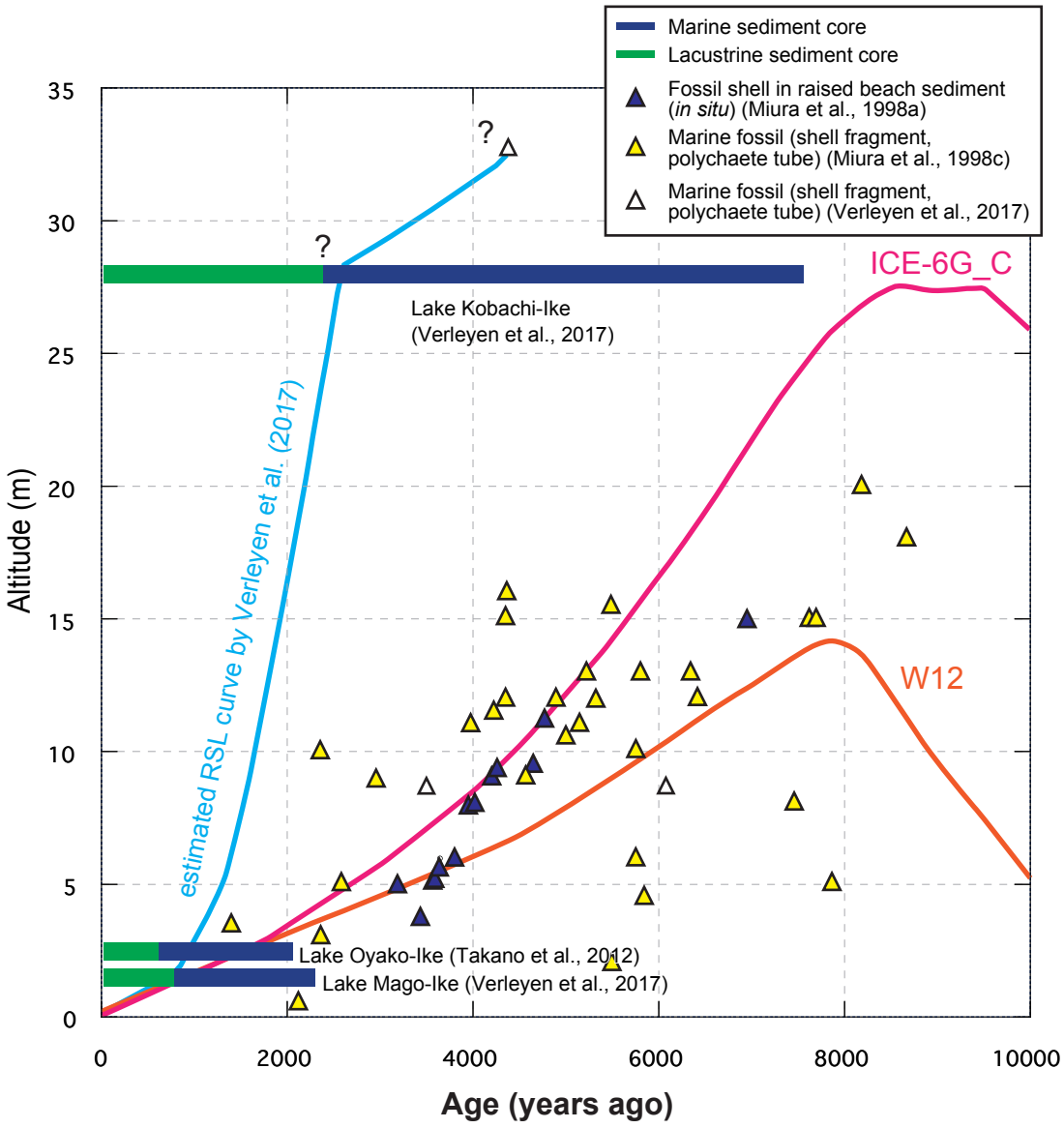

Fig. 5-3. Relative sea-level curves for Skarvsnes modified Verleyen et al. (2017). The plots show the height above present sea level of the median calibrated ^{14}C ages of the *in situ* fossil shells in the raised beaches (blue triangles; Miura et al. 1998a) and other previous data of marine fossils extracted from Miura et al. (1998c). The marine sediments in the isolation lakes (blue bar), and the lacustrine sediments in the isolation lakes (green bar), including the data extracted from Takano et al. (2012) are also shown. The orange line shows the output of the W12 model (Whitehouse et al., 2012a), and the pink line is the output of the ICE-6G_C model (Argus et al., 2014). The blue line is a hand-drawn approximation of the minimum RSL by Verleyen et al. (2017).

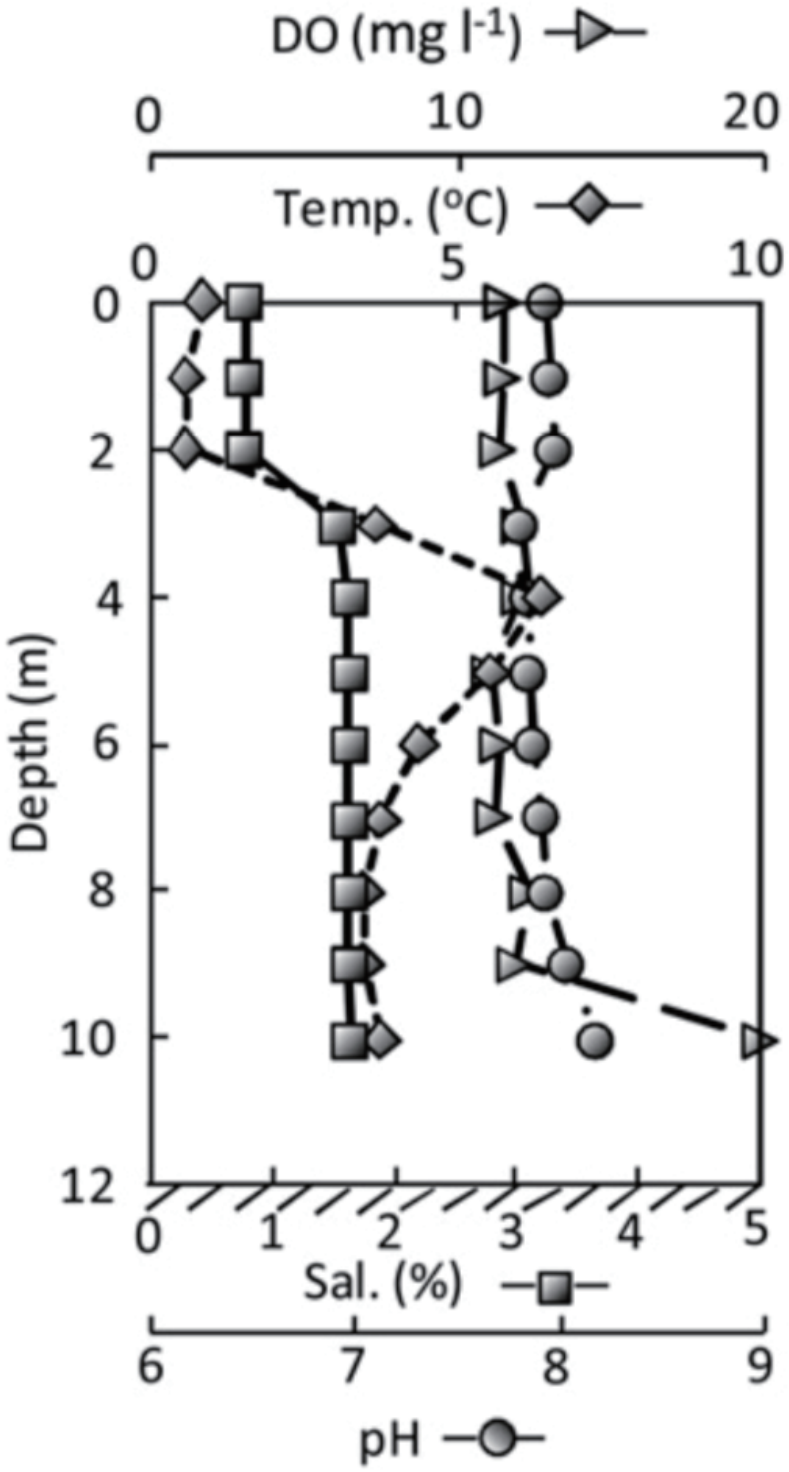

Fig. 5-4. Vertical profiles of Lake Kobachi-Ike of dissolved oxygen (DO; mg/l), temperature (°C), salinity (%) and pH as in Kimura et al. (2010).

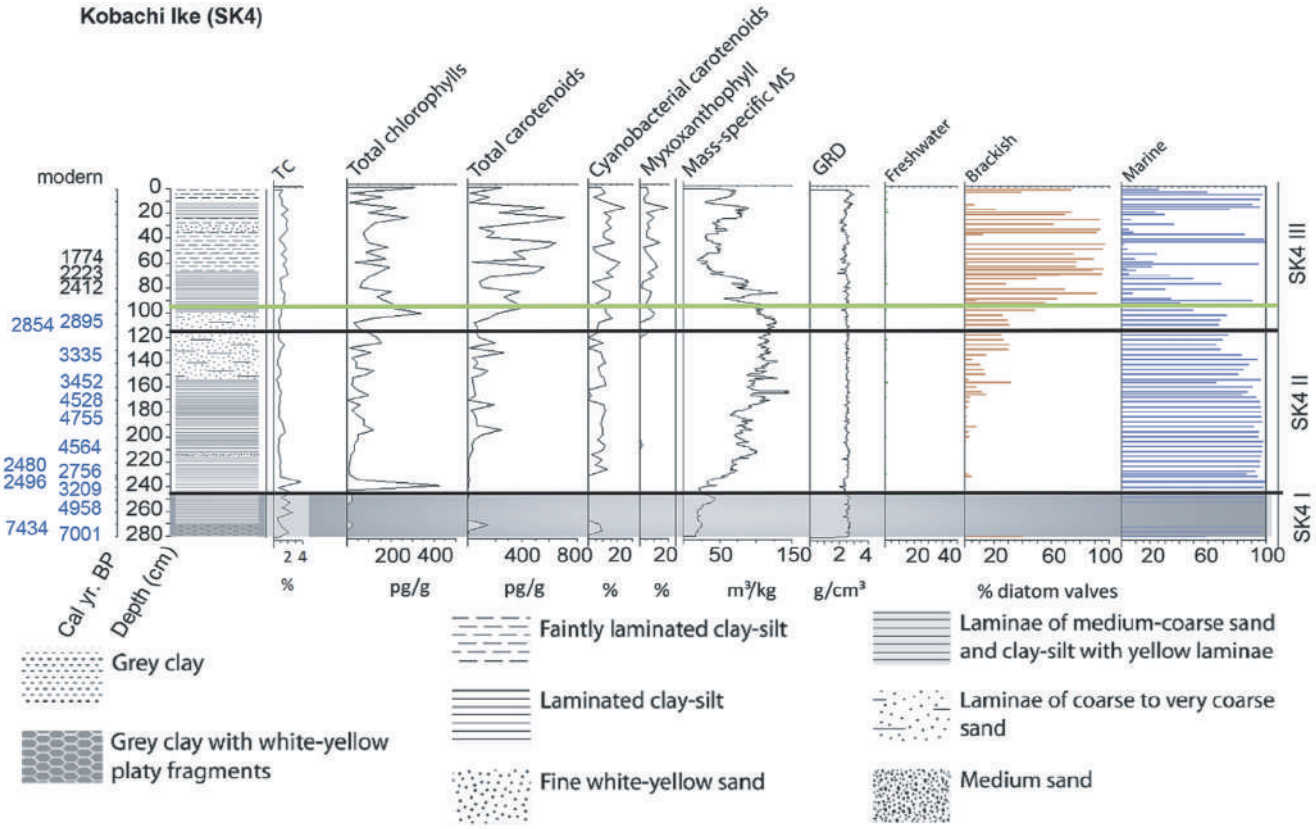

Fig. 5-5. Summary diagram of the Lake Kobachi-Ike (28 m a.s.l.) sediment core as in Verlyeyen et al. (2017). Verleyen et al. (2017) combined fossil diatoms with fossil pigments and changes in the sediment properties (magnetic susceptibility) to determine the isolation event. Verleyen et al. (2017) concluded the green line represents the interpreted start of full lacustrine conditions.

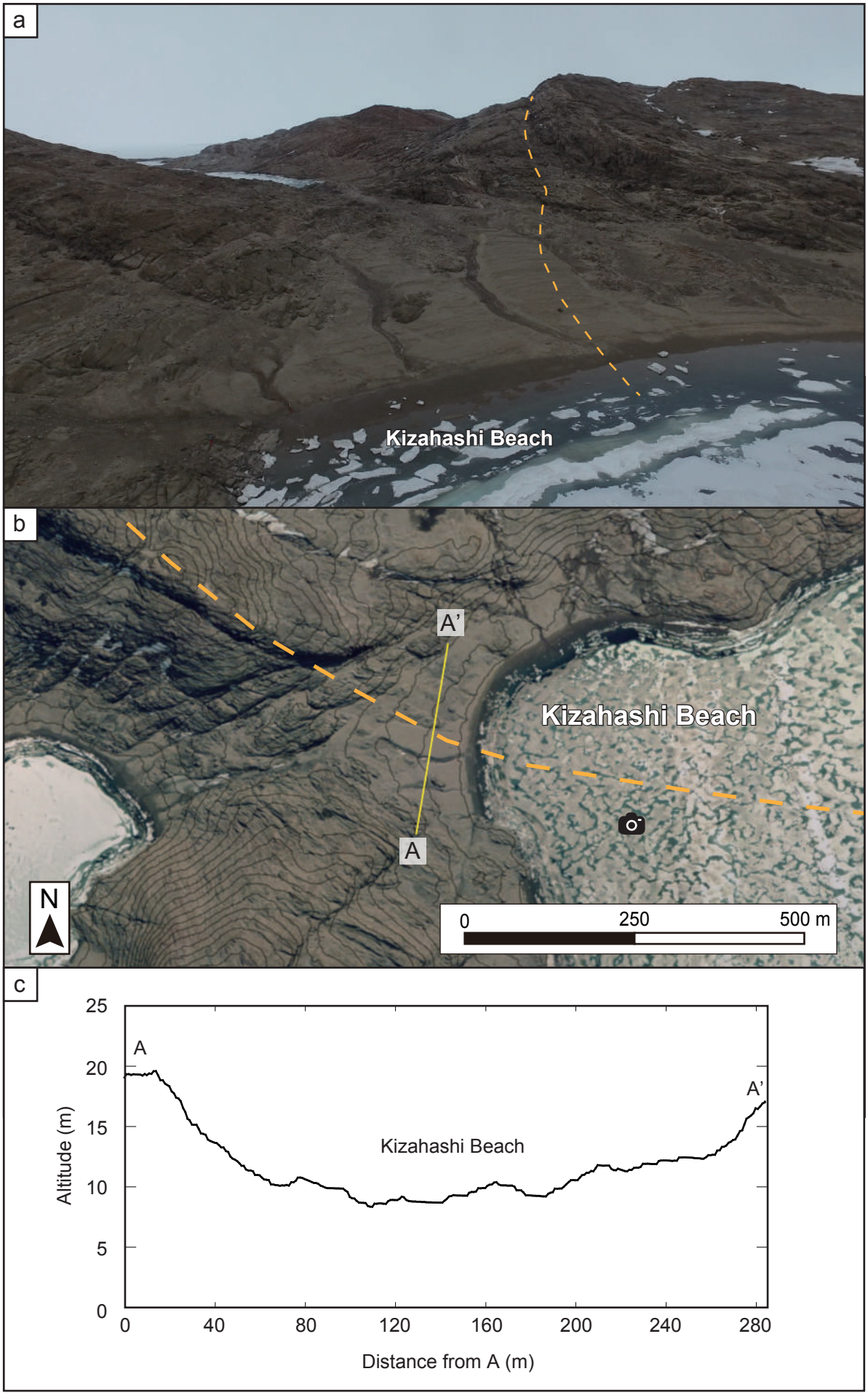

Fig. 5-6. (a) Aerial photo of Kizahashi beach, where the developed as marked stepped raised beach in Skarvsnes. Orange dashed line shows the thrust fault reported by Ishikawa et al. (1977). (b) Orthioimage around the Kizahashi Beach. Contours are 5 m intervals and are derived from SfM-DSM. (c) Cross-section of transect A–A' shown in b.

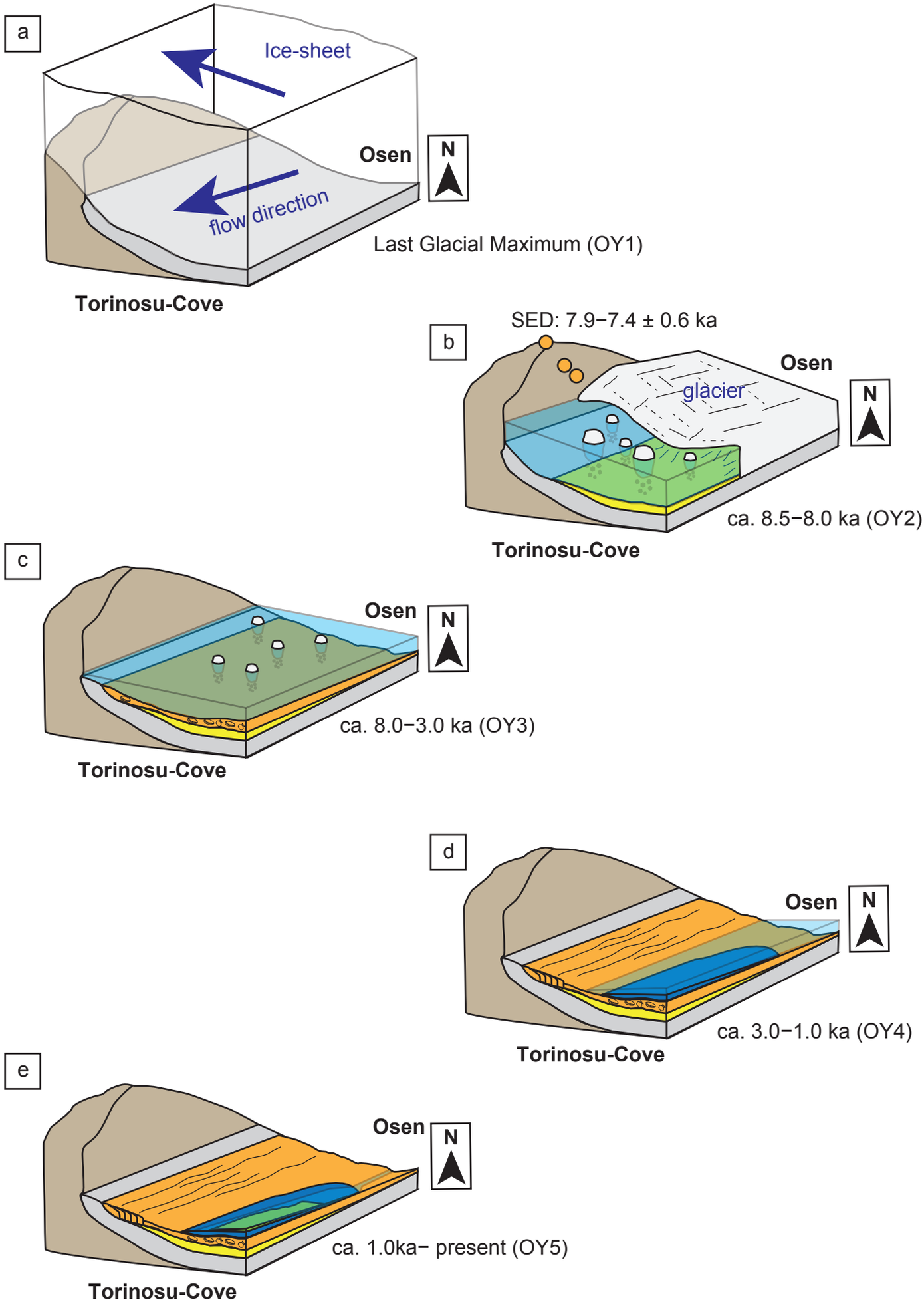

Fig. 5-7. Geomorphological history around Lake Oyako-Ike.

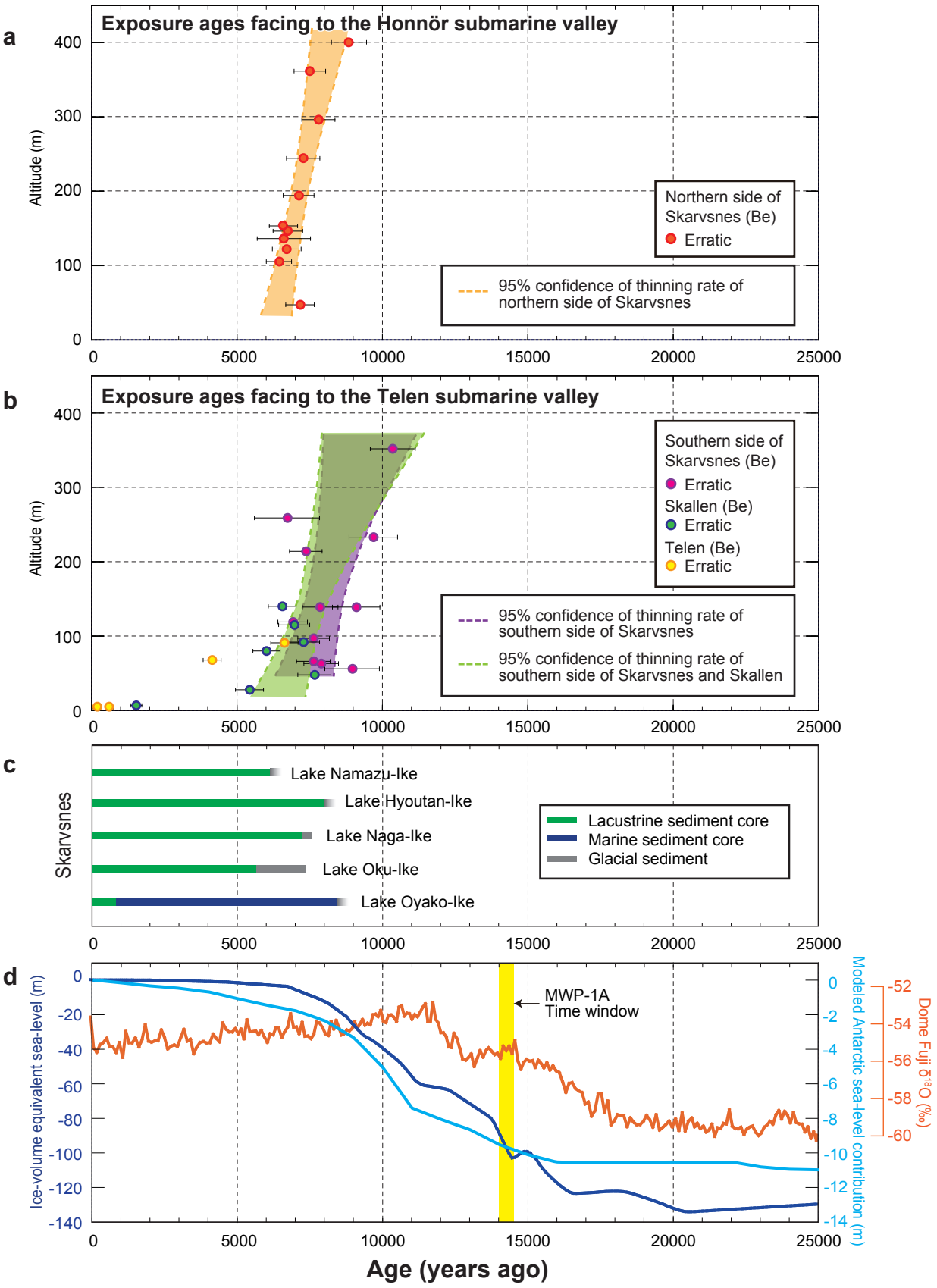
a
Exposure ages facing to the Honnör submarine valley
Altitude (m)
Northern side of Skarvsnes (Be)
Erratic
95% confidence of thinning rate of northern side of Skarvsnes
b
Exposure ages facing to the Telen submarine valley
Altitude (m)
Southern side of Skarvsnes (Be)
Erratic
Skallen (Be)
Erratic
Telen (Be)
Erratic
95% confidence of thinning rate of southern side of Skarvsnes
95% confidence of thinning rate of southern side of Skarvsnes and Skallen
c
Skarvsnes
Lake Namazu-Ike
Lake Hyoutan-Ike
Lake Naga-Ike
Lake Oku-Ike
Lake Oyako-Ike
Lacustrine sediment core
Marine sediment core
Glacial sediment
d
Ice-volume equivalent sea-level (m)
Modeled Antarctic sea-level contribution (m)
Dome Fuji δ18O (‰)
MWP-1A
Time window
Age (years ago)

Fig. 5-8.

Fig. 5-8. ^{10}Be exposure ages of erratic rocks plotted against altitude for (a) facing to the Honnör submarine valley (northern side of Skarvsnes), (b) facing to the Telen submarine valley (southern side of Skarvsnes, Skallen, and Telen) including the exposure ages of Yamane et al. (2011).Dashed lines denote the 95% confidence intervals from linear regression analysis, (c) calibrated lake sediment ages of this study, (d) δ^{18}O record from Dome Fuji ice core (orange line; Dome Fuji Ice Core Project Members., 2017) plotted alongside ice-volume equivalent global sea-level changes (dark-blue line; Lambeck et al., 2014) and a modeled Antarctic contribution to sea-level change (light-blue line; Briggs et al., 2014) since 25 ka. Dome Fuji Station is located ~1,000 km inland from Syowa Station. The δ^{18}O record obtained from Dome Fuji provide a relative temperature index that represents the surrounding areas in Antarctica. The timing of Meltwater Pulse 1A (MWP-1A) is shown in yellow shading (Lambeck et al., 2014). The ice-sheet retreat episode of the southern Soya Coast (95% confidence intervals from linear regression analysis of SED, and bottom ages of lake sediment) does not correspond to any recorded increase in regional atmospheric temperature or significant sea-level rise event such as MWP-1A.

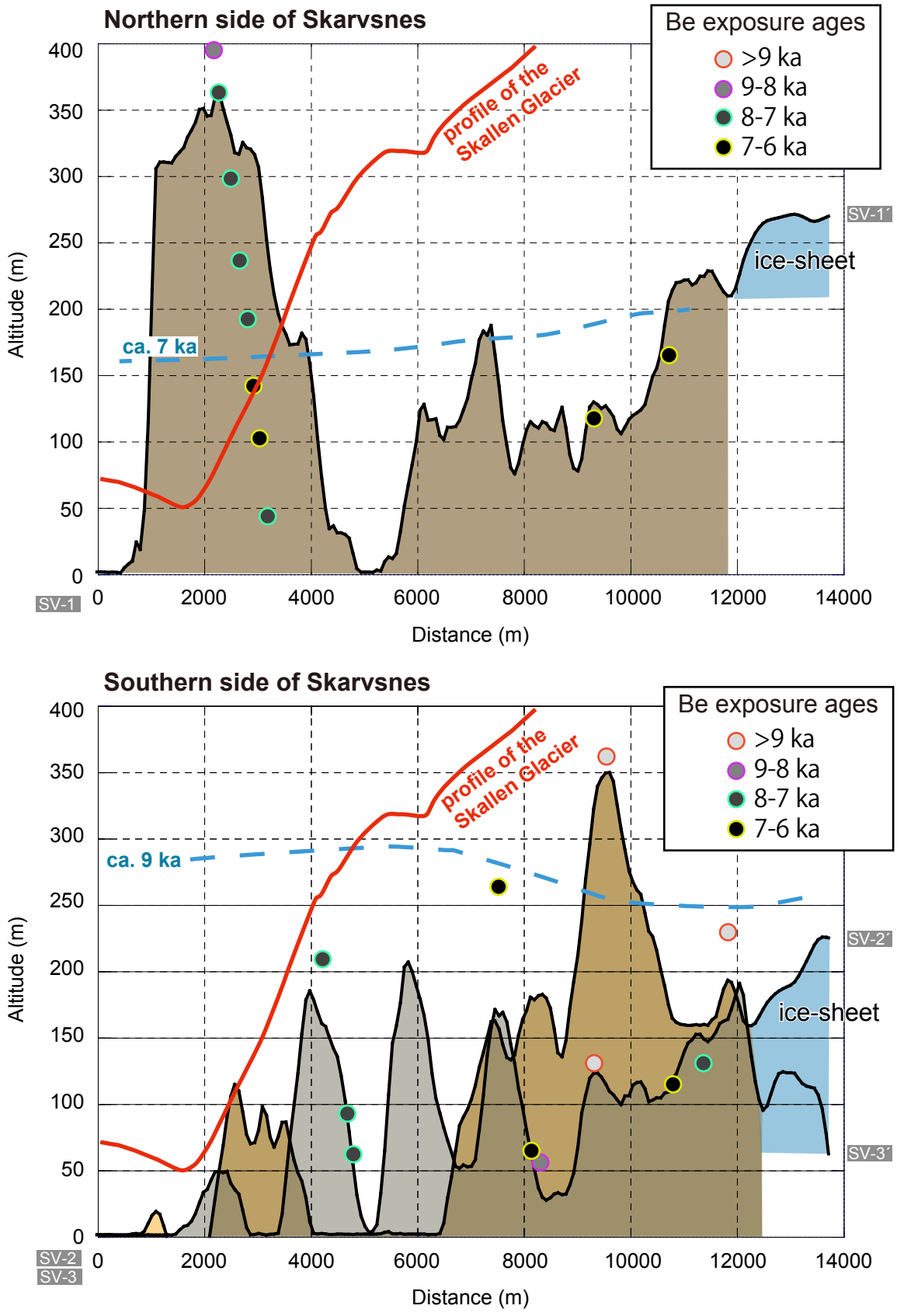

Fig. 5-9. Cross-sections of parallel to the submarine valley on the northern and southern sides of the Skarvsnes. SED sampling locations of this study and Yamane et al.(2011) are also shown.The results show that similar ages can be found from the almost same altitude regardless of the distance from the current ice sheet margin at the northern part of the Skarvsnes (Blue dashed line show the hand-drawn approximation of the ice-sheet profile). This age distribution cannot be explained by simple retreating of the modern glacier surface profile acuaired August, 2016 from the TanDEM-X 90 m DEM (Wessel et al., 2018) (orange line).

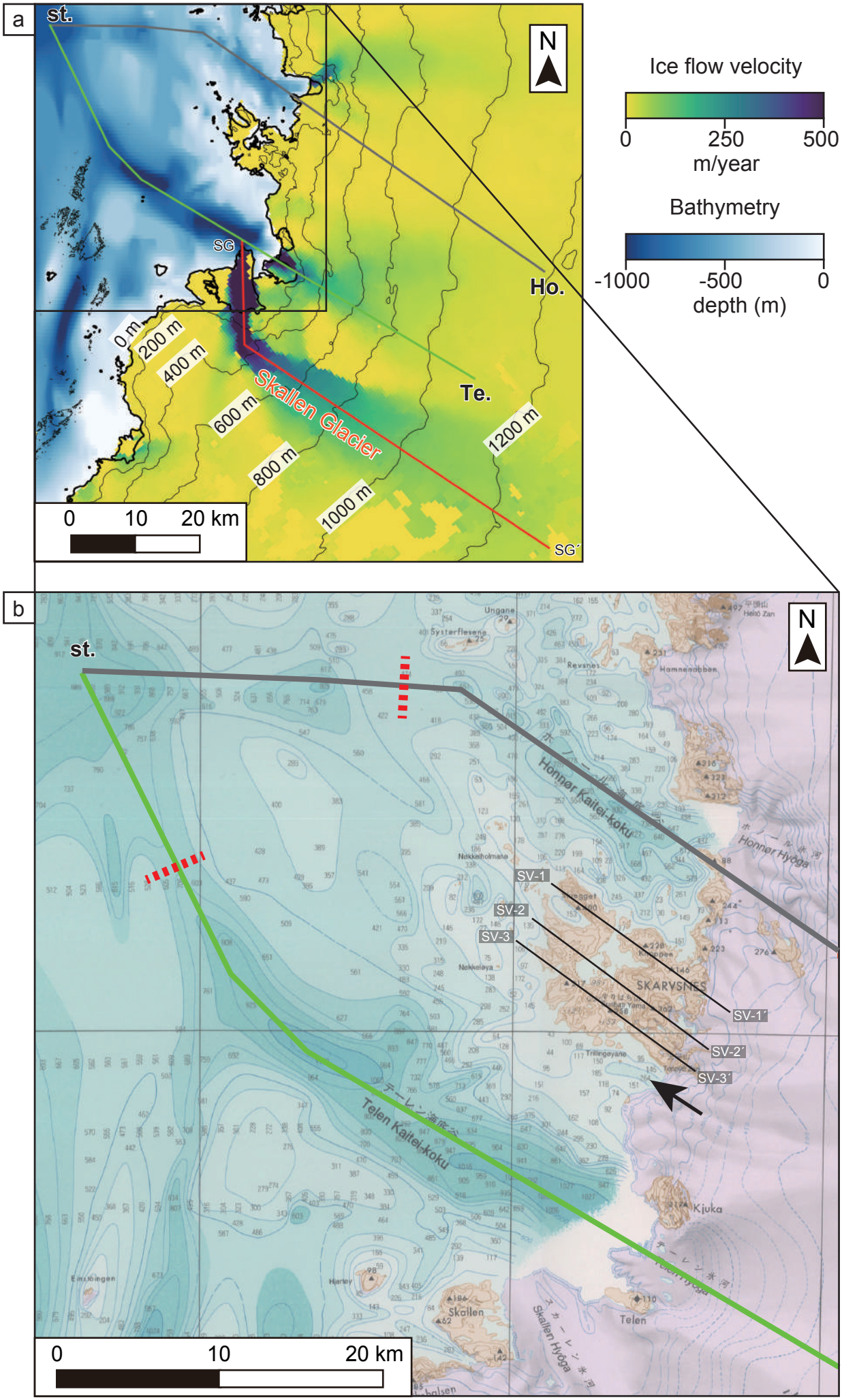
a
st.
N
Ice flow velocity
0
250
500
m/year
Bathymetry
-1000
-500
0
depth (m)
SG
Ho.
Te.
0 m
200 m
400 m
600 m
800 m
1000 m
1200 m
Skallen Glacier
SG´
0
10
20 km
b
st.
N
Honnør Kaitei-koku
Honnør Hyōga
SV-1
SV-2
SV-3
SV-1´
SV-2´
SV-3´
SKARVSNES
Telen Kaitei-koku
Kjuka
Skallen
Telen
Skallen Hyōga
0
10
20 km

Fig. 5-10

Fig. 5-10. (a) Flow velocity image around the southern Soya Coast from InSAR-Based Antarctica Ice Velocity Map (MEaSUREs Ice velocity map) (Rignot et al., 2017). Bathymetry is from the regional bathymetric chart of Moriwaki and Yoshida (2002). The grey (st. to Ho.) and green (st. to Te.) lines show profiles taken in cross-sections in Fig.5-11 and Fig. 5-12, respectively. The cross-section along the orange line (SG to SG´) of modern Skallen Glacier is shown in Fig. 5-9, Fig.5-11, and Fig. 5-12. Contours are 200 m intervals and are derived from the TanDEM-X 90 m Digital Elevation Model (Wessel et al., 2018). (b) Bathymetry map around the Skarvsnes (Moriwaki and Yoshida. 2002). The submarine valleys of about 200 m in depth exist in the southern part of the Skarvsnes (indicated by black arrow), which is thought to be associated with a small valley glacier. The black lines (SV-1, SV-2, and SV-3) show profiles taken in cross-sections in Fig.5-9. The estimated grounding line position during the LGM in Fig.5-11 and Fig. 5-12 are shown in red dashed lines.

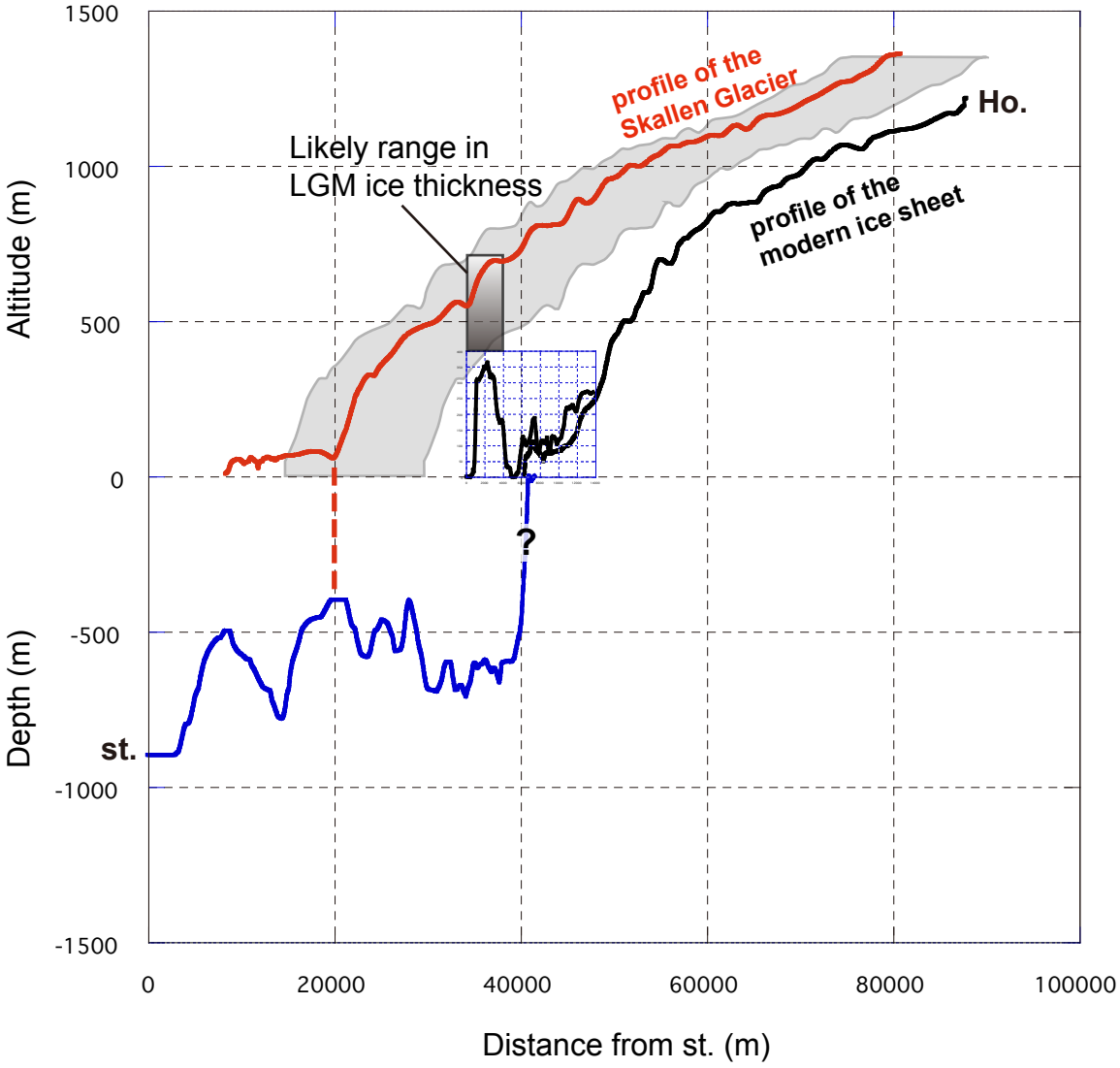

Fig. 5-11. Profile of the along flow line of the Telen submarine valley (st. to Ho.; the grey line of Fig. 5-10). The blue and black lines show profiles of the bathymetry and terrestrial surface elevation, including the ice-free area and ice-sheet, respectively. The grey shade shows the possible range of ice sheet extent in LGM based on geo-morphological evidence of the summit of Skjegget and the 2D shape of the Skallen Glacier. The ridge of the submarine valley exists within this range, and the ice sheet profile of the orange line is a probable profile at the LGM ice sheet.

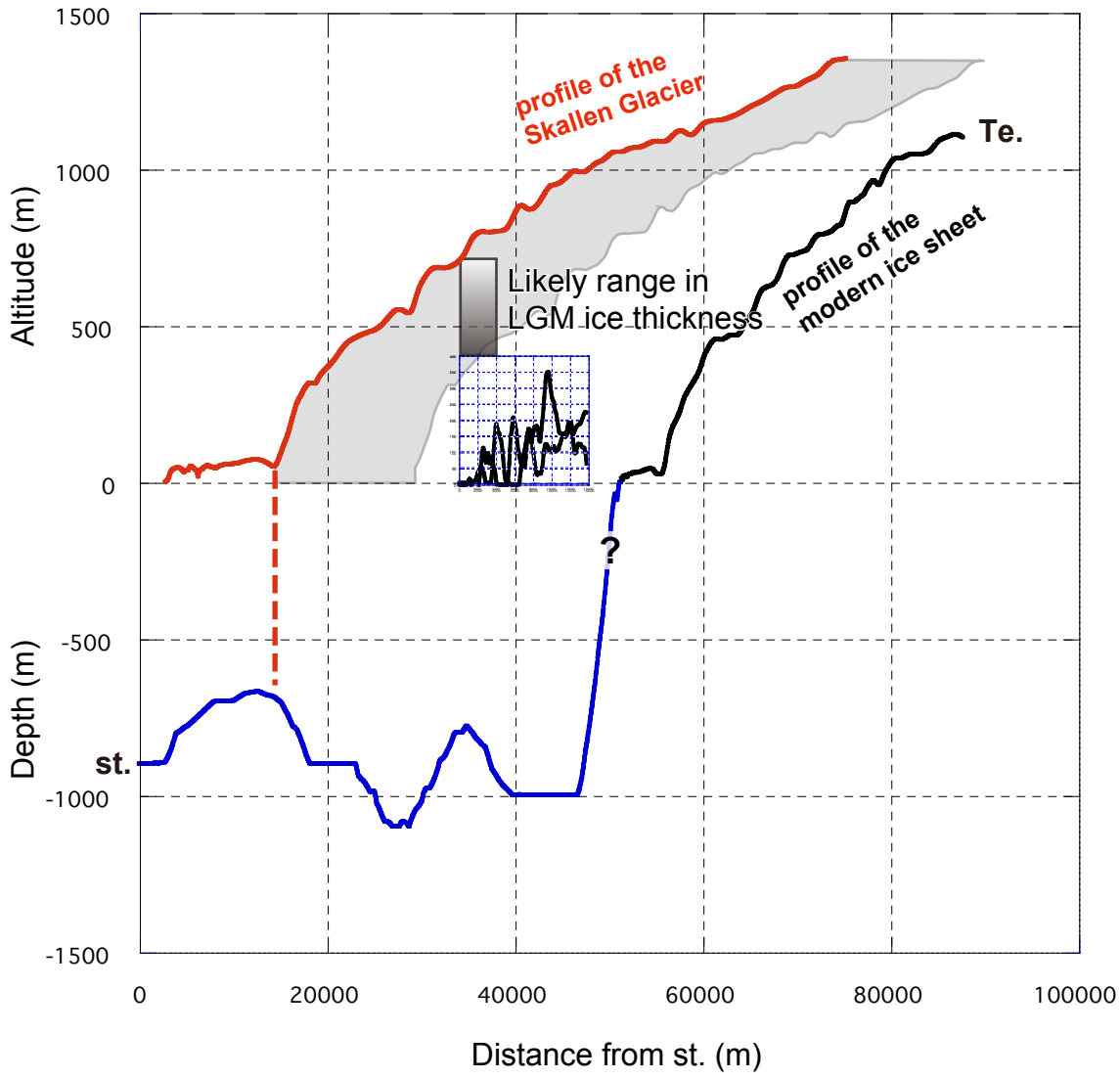

Fig. 5-12. Profile of the along flow line of the Telen submarine valley (st. to Te; the green line of Fig. 5-10). The blue and black lines show profiles of the bathymetry and terrestrial surface elevation, including the ice-free area and ice-sheet, respectively. The grey shade shows the possible range of ice sheet extent in LGM based on geo-morphological evidence of the summit of Skjegget and the 2D shape of the Skallen Glacier. The ridge of the submarine valley exists within this range, and the ice sheet profile of the orange line is a probable profile at the LGM ice sheet.

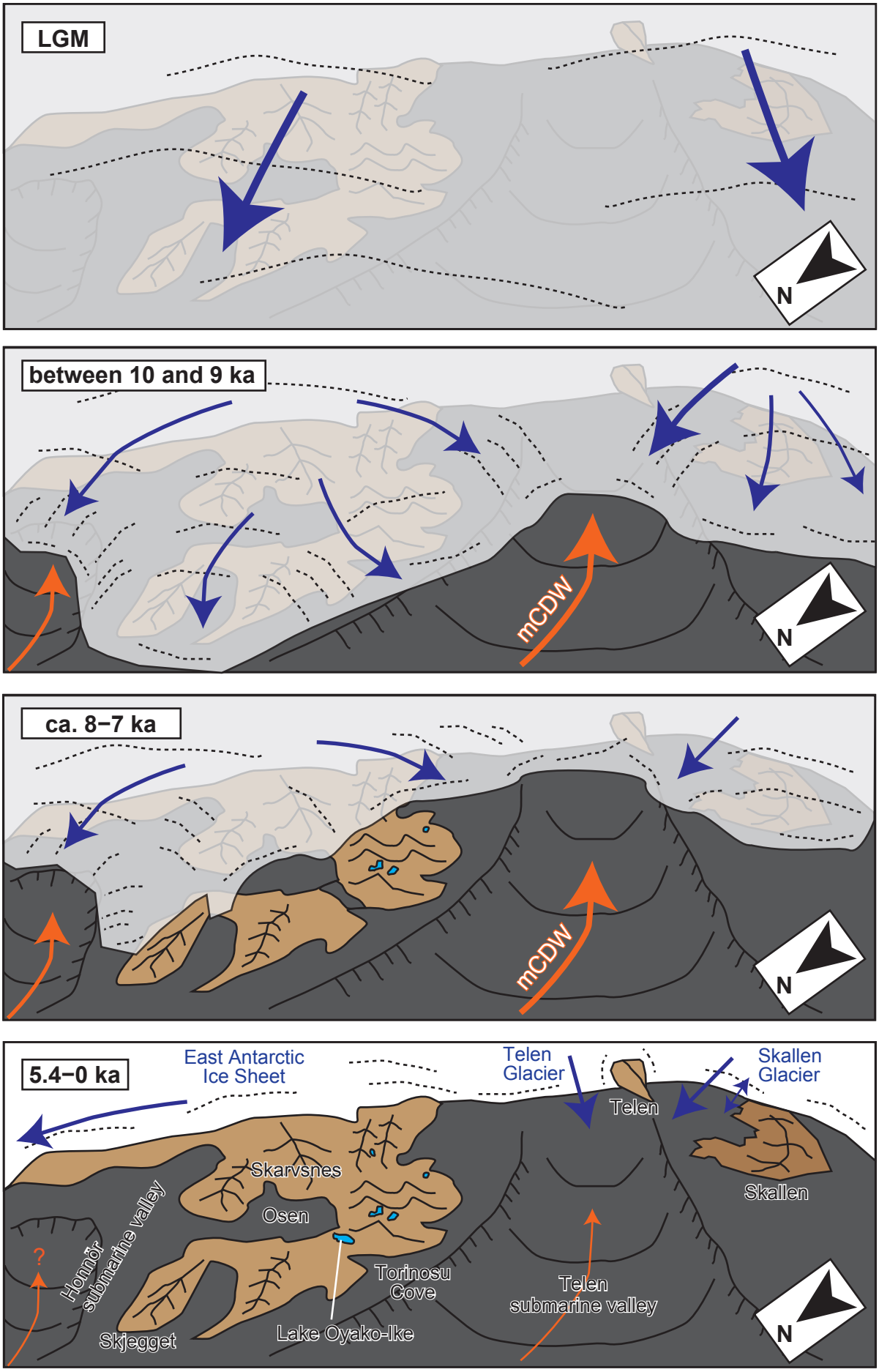
LGM
N
between 10 and 9 ka
mCDW
N
ca. 8–7 ka
mCDW
N
5.4–0 ka
East Antarctic Ice Sheet
Telen Glacier
Skallen Glacier
Telen
Skallen
Skarvsnes
Osen
Honnør submarine valley
?
Torinosu Cove
Telen submarine valley
Skjegget
Lake Oyako-Ike
N

Fig. 5-13.

Fig. 5-13. A conceptual reconstruction of different ice-sheet configurations along the southern Soya Coast (viewed from the northwest). The inferred history of ice-sheet retreat is as follows. The EAIS covered the entire southern Soya Coast during the LGM and had advanced to the ca. 30 km northwest. The ice sheet thinning and retreat had started Early-Holocene (between 10 and 9 ka), with flow direction changing as a result of bedrock topographic control. The thinning and retreat of the EAIS in this area is considered to have been marine ice-sheet instability caused by the strong influx of the modified Circumpolar Deep Water (orange arrows) via deep submarine valley. the slight differences in the timing of the initiation of the ice-sheet retreat between the northern and southern sides of Skarvsnes can also be explained by the geographical configuration of this area. The Telen submarine valley, southern side of Skarvsnes, is a large submarine valley with more than 1000 m deep, while the Honnör submarine valley is slightly shallower and smaller. This suggests that the Telen submarine valley is potentially more susceptible to mCDW intrusion, which may cause earlier deglaciation in the southern side of Skarvsnes. Blue arrows indicate the flow directions of major ice streams in this area.

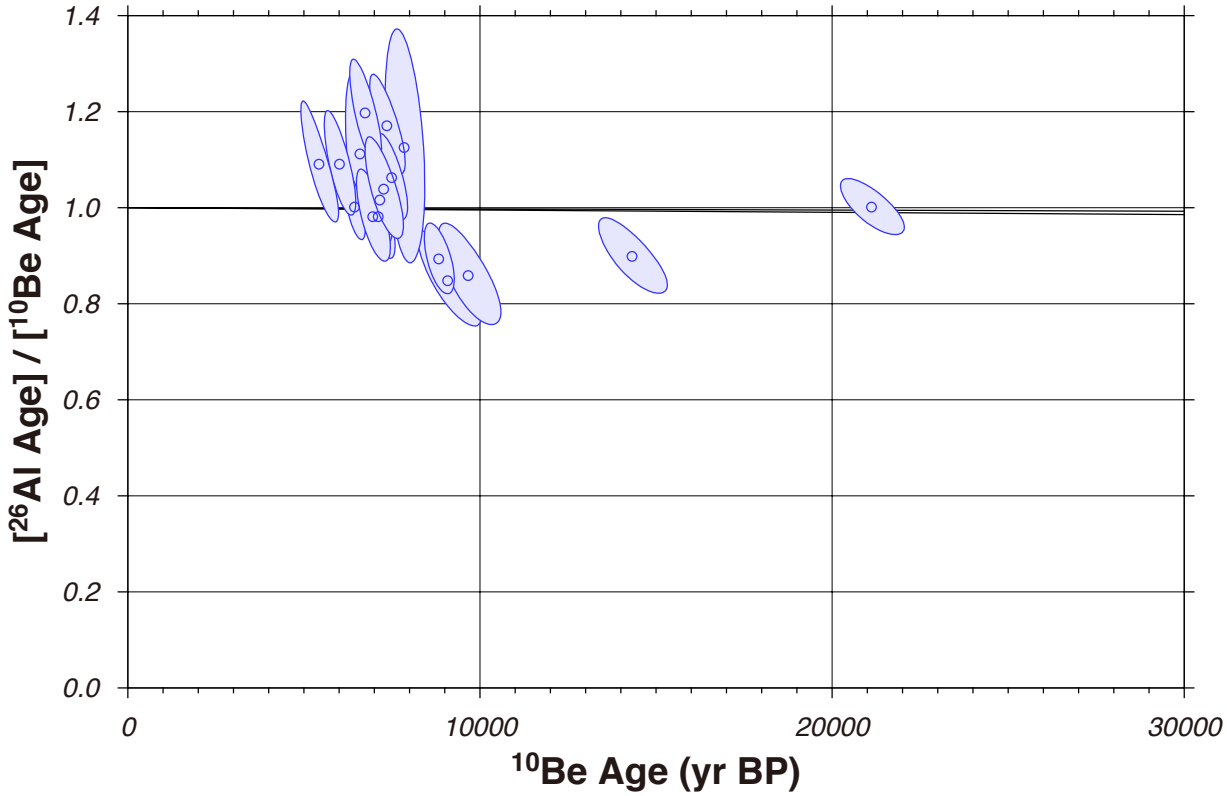

Supplementary figure. 1

^{10}Be–^{26}Al/10Be diagram for all samples from this study, calculated using the CRONUS-Earth online calculators (https://hess.ess.washington.edu/). The x-axis is the measured ^{10}Be concentration normalized by the production rate at the site, which has units of years and is equal to the apparent ^{10}Be exposure age of the sample. The y-axis is the measured ^{26}Al/^{10}Be ratio normalized to the production ratio. The black line represents of the simple-exposure line.

Supplementary figure. 2

Photographs of all samples for surface exposure dating.

Supplementary figure. 2

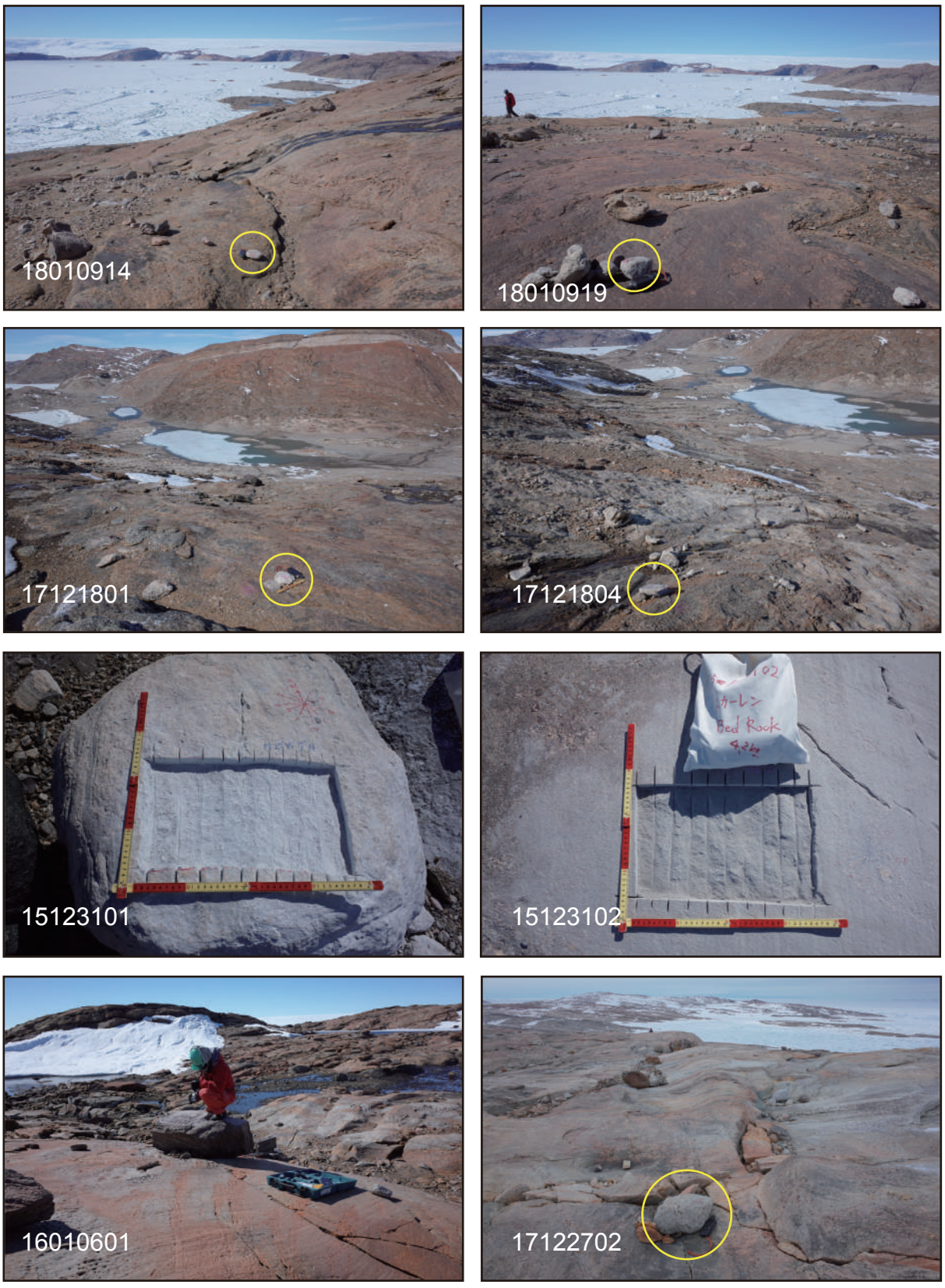

Supplementary figure. 2

Supplementary figure. 2